ON THE PROCESSING, MICROSTRUCTURE AND STRENGTH OF BRITTLE FOAMS

by
Sirui Bi

A dissertation submitted to Johns Hopkins University in conformity with the requirements for the degree of Doctor of Philosophy

Baltimore, Maryland
October 2020

Abstract

This dissertation focuses on the nonlinear mechanics of open-cell foams and in particular the connection between their cellular microstructure and their macroscopic strength. We first examine the quasi-brittle failure of Reticulated Vitreous Carbon (RVC) foams under compression. The carbon foam microstructure is analyzed using microcomputed tomography. It is shown to follow closely the polyhedral structure of the precursor polymer foam, that is pyrolyzed to produce its carbon counterpart. Scanning single foam-ligaments reveals that their cross-sectional area is a hypocycloid with a non-uniform distribution across the ligament length. X-ray tomography also shows several processing-induced defects in the form of anisotropy and remaining closed-cell faces. Specimens of different geometries and dimensions are crushed between rigid surfaces in order to examine the effect of load distribution, specimen size, relative density and cell-size on the resulting response and the associated crushing strength of the foam. In-situ testing and image analysis is utilized to observe the failure mechanism and associate it with the recorded force-displacement response.

In the second part of this thesis, additive manufacturing is employed to examine the strength of brittle foams with controlled microstructural characteristics. Tessellation-based topologies are used to generate realistic microstructures of open-cell foams that are subsequently 3D-printed by stereolithography. The stress-strain curve and fracture strength of the base photopolymer are measured using tensile tests on small dog-bone specimens with the dimensions of foam ligaments. Synthesized foams are scanned by microcomputed tomography and manufacturing-induced variations are quantified

through image analysis. Characterization shows that there is a small amount of volume shrinkage of the material caused by the additive manufacturing process, but all other microstructural features are accurately reproduced. We then perform a series of experiments to measure the compressive response and strength of the 3D-printed foams and connect it to load-transferring conditions, the strength of the base solid material and the foam relative density.

Finally, we examine the compressive response of open-cell aluminum foams under high temperatures. Foam specimens with different cell-sizes are compressed within an environmental chamber under a range of temperatures $20\,^{\circ}\mathrm{C} \leq T \leq 300\,^{\circ}\mathrm{C}$. The localization and evolution of collapse are monitored and analyzed using Digital Image Correlation (DIC) and the overall force-displacement response is measured. The results indicate that high temperatures significantly affect all mechanical properties of aluminum foams. Both the limit and plateau stresses were found to decrease linearly with temperature. More importantly, their drop is not proportional to the corresponding one in the base material's yielding stress. The densification strain, that is a measure of the plateau extension, also follows a linear trend albeit in an increasing manner. This increase is attributed to changes of the collapse mechanism, which at high temperatures involves localization in different zones within the foam, as well as increased compaction at the cell-level caused by the base material softening. Finally, we measure the reduction in the strain energy absorption capacity of the foam caused by high temperatures.

Thesis Readers

Dr. Stavros Gaitanaros (Primary Advisor)
Assistant Professor
Department of Civil and Systems Engineering
Johns Hopkins University

Dr. James K. Guest
Associate Professor
Department of Civil and Systems Engineering
Johns Hopkins University

Dr. Benjamin W. Schafer
Professor
Department of Civil and Systems Engineering
Johns Hopkins University

Dedicated to my grandmother, my parents, my husband and my son.

Acknowledgements

There are so many people to thank. Of course, I would like to express my greatest thanks and sincere gratitude to my advisor, Prof. Stavros Gaitanaros, for all his excellent guidance, extensive support and continuous encouragement throughout my Ph.D. studies. His knowledge, experience and deep understanding of the subject helped me through every step to accomplish this work. His patience, understanding and trust helped me through various difficulties in my studies and life. His discreet and optimistic attitude will affect me long-term and I owe my special gratitude to him.

I would like to thank Prof. Michael D. Shields for a fruitful collaboration and for sharing his deep insight on the behavior of aluminum under high-temperatures. I would also like to express my gratitude to Prof. Lori Graham-Brady, Prof. James K. Guest, Prof. Kevin Hemker, Prof. Sung Hoon Kang, and Prof. Feng Zhu for serving on my GBO committee. My sincere thanks to Prof. Benjamin W. Schafer and Prof. James K. Guest for serving as my thesis committee and reviewing this dissertation. To Guannan Zhang, my summer internship mentor at Oak Ridge National Lab, I owe a special thank you. He guided me into a new field of research and facilitated my career development and general outlook on the scientific endeavor profoundly.

Nick Logvinovsky and Matthew Shaeffer were always available to provide experimental support and their help has been invaluable. I would also like to thank all members of the Extreme Mechanics of Architected Materials Group, Alireza Bayat, Shengzhi Luan and Enze Chen, for their help and support along the way and great

time that you spent with me. Additionally, I am grateful to my colleagues at the JHU Civil and Systems Engineering Department. Many thanks to Aakash, Hamid, Hak Yong, Jinlei, and Noah for many insightful discussions.

I must thank my parents for their continued love and support after all these years. In particular, I would like to thank my grandmother for raising and accompanying me throughout my childhood and adolescence. A great appreciation to my loving husband, Jiaxin Zhang, for his unconditional love and unwavering support. Finally, I dedicate this to my son Bryson.

The content of this dissertation has been presented in the following publications:

Bi, S., Chen, E. and Gaitanaros, S., 2020. Additive manufacturing and characterization of brittle foams. Mechanics of Materials, 145, p.103368.

Aakash, B.S., Bi, S., Shields, M.D. and Gaitanaros, S., 2019. On the high-temperature crushing of metal foams. International Journal of Solids and Structures, 174, pp.18-27.

Contents

List of Tables

List of Figures

Chapter 1

Introduction

Cellular solids have excellent mechanical, thermal and acoustic properties and have thus been widely used in a variety of engineering applications including thermal shielding, acoustic insulation and shock absorption. Their excellent stiffness- and strength-to-weight ratios make them attractive as cores in sandwich panels for naval and aerospace structures. These man-made structures mimic a plethora of natural cellular materials such as plant stems, trabecular bone, birds' beaks, animal quills, wood and many others (See Fig. 1-1) [1]. Synthetic cellular materials, such as honeycomb, foams and micro-lattices (see Fig. 1-2) are manufactured from polymers, metals, as well as brittle materials such as carbon. Foams have a polyhedral cellular microstructure and relative densities (or volume fraction) of about 1% at the lower end and 15% at the other extreme (Hilyard and Cunningham [2], 1994; Ashby et al. [3], 2000). Their cells can be open or closed: in the first case the material is concentrated in the nearly straight edges of the polyhedra, and in the nodes at which they intersect; in the latter case the cell faces are covered with thin membranes or plates.

The compressive response of cellular material, including foams, typically consists of three distinct regimes: an initial linear elastic part that terminates on a limit stress, a stress plateau that extends to high macroscopic strains, and the densification stage where the response stiffens for a second time (Gibson and Ashby [4], 1999). The initial limit stress can be attributed to yielding, buckling, and/or brittle fracture

depending on the mechanical behavior of the underlying solid material and the cellular microstructure; see Klintworth and Stronge [5] (1988), Papka and Kyriakides [6] [7] [8] (1994, 1998a,b), and Triantafyllidis and Schraad [9] (1998) for honeycombs; see Zhou et al. [10] [11] [12] (2002, 2004, 2005), Gong and Kyriakides [13] (2005), Gong et al. [14] (2005), Jang and Kyriakides [15] [16] (2009a,b), and Gaitanaros et al. [17] (2012) for open-cell foams; see Sugimura et al. [18] (1997) and Gioux et al. [19] (2000) for closed-cell foams. In the case of open-cell metallic foams this peak stress is caused by the combination of yielding and buckling of foam ligaments (Zhou et al. [12], 2005). Localization is associated with the collapse of foam cells in a "weak" domain within the microstructure. As foam compaction continues, a band of collapsed cells is formed that traverses the material in a non-planar manner (Jang and Kyriakides [15], 2009a; Gaitanaros et al. [17], 2012). The band width broadens with the collapse of neighboring cells while stress levels remain nearly constant. Note here that the formation of additional bands of collapsed cells is also possible. Once these bands reach the foam boundaries, typically adhered to thin metal plates, the response stiffens and densification initiates. In this regime, the deformation involves additional compaction of the previously collapsed cells in a homogeneous stable manner. Contrary, the response of flexible polymeric foams is governed by elastic instabilities that range from macroscopic (long wavelength) to microscopic (wavelength comparable to cell-size) depending on the foam density, anisotropy and polydispersity.

The characteristic load-plateau of their compressive response makes polymeric and metallic foams excellent candidates for energy absorption and impact mitigation applications. Cellular solids made of a brittle material (e.g. ceramics, carbon), on the other hand, because of their low weight and large surface area have found use in energy storage devices, filtration, acoustic insulation, armored textiles as well as thermal shielding under extreme conditions. In all of these applications, material integrity remains a requirement for functionality and performance. A characteristic example

is the carbon foam on the Parker Solar Probe that is used for thermal protection, but at the same time has to withstand impacts from hypervelocity dust particles as the spacecraft flies close to the sun's atmosphere [20]. Despite their significance however, the properties of brittle cellular materials have been largely understudied in contrast to the enormous body of work on their metallic counterparts or the brittle failure of traditional monolithic materials. The small number of existing experimental studies, which span a variety of different material systems manufactured by different processes and using different experimental set-ups, makes it difficult to draw generalized conclusions. It is clear that an understanding between (a) foam microstructure, (b) the parent solid material fracture strength and (c) the resulting macroscopic foam strength is crucial for the design of stronger foams. This process remains a significant challenge, however, mainly because of the complex microstructure and associated manufacturing induced variations/imperfections, the difficulty in characterizing the foamed base material and establishing its fracture strength, and the prohibitive computational cost of physics-based modeling.

1.1 Outline of the Present Study

The goal of the present experimental study is twofold: (a) to understand the governing failure mechanism of brittle foams under compression and its connection with the foam microstructure and (b) examine the effect of high-temperatures on the mechanical properties and energy absorption capacity of metal foams. The thesis is organized as follows. Chapter 2 focuses on the relationship between processing, microstructure and mechanical properties of commercial open-cell carbon foams. Microcomputed tomography and a series of crushing experiments are used to showcase the large variation of measurements on the foam strength caused by the complex microstructure, processing-induced defects and the high sensitivity to load distribution. In Chapter 3 additive manufacturing is employed to synthesize brittle foams with controlled

morphological characteristics. The parent solid's stress-strain curve is extracted by in-situ micro-tensile tests while the microstructure of foam specimens is analyzed using microcomputed tomography in order to quantify manufacturing-induced morphological deviations. The foam crushing strength is then measured as a function of loading conditions and microstructural features. The complete crushing response of Al foams under high-temperatures is examined in Chapter 4. Crushing experiments within an environmental chamber are used to quantify the effect of elevated temperatures on the foam compressive response and the associated limit stress, densification strain and total energy absorption. Furthermore, imaging analysis and DIC are used to examine how high temperatures alter the initiation and evolution of crushing within the material. Finally, in Chapter 5 the main results of this study are summarized and potential future research directions are explored.

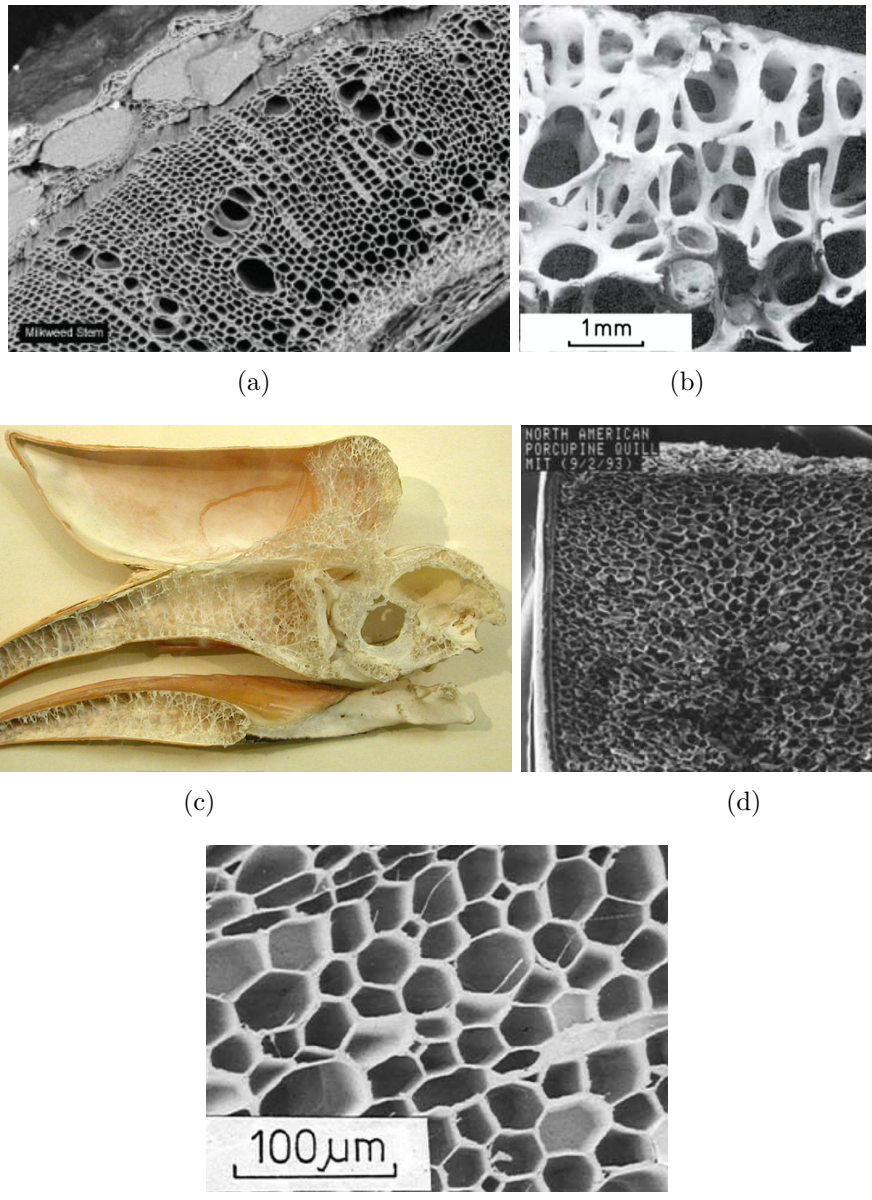

(a) (b)

(c) (d)

(e)

Figure 1-1. Natural cellular materials [1]: (a) cross sections of milkweed stem (b) trabecular bone (c) hornbill bird beak (d) porcupine quill (e) balsa wood.

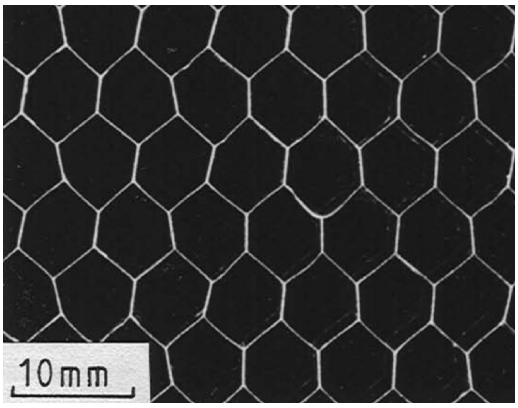

(a)

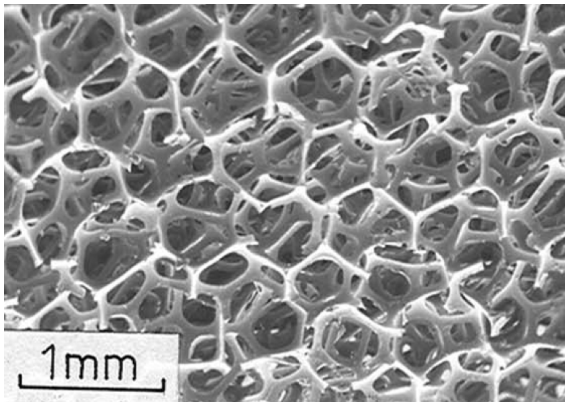

(b)

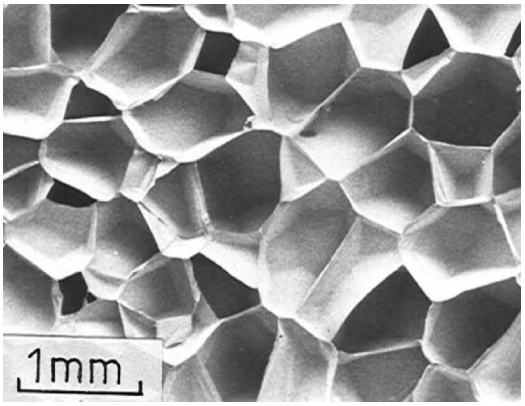

(c)

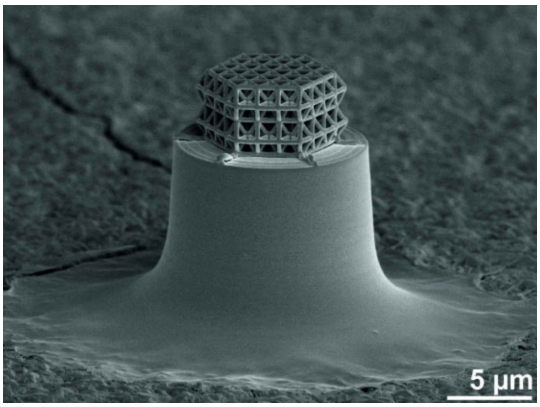

(d)

Figure 1-2. Man-made cellular materials (a) aluminum honeycomb [1] (b) open-cell polyurethane foam [1] (c) closed-cell polyethylene foam [1] (d) carbon nanolattices [21].

Chapter 2

Microstructure and Crushing Strength of Carbon Foams

Carbon is a unique element with a large number of allotropes having a wide range of properties. By modifying processing parameters and structure, carbon-based materials can be generated with mechanical, thermal and acoustic properties that span several orders of magnitude. Carbon allotropes can also be used as parent solids in porous cellular materials. Typical foam synthesis involves a sequential process including blowing, carbonizing and thermal treatment. Alternatively, it is also feasible to use autoclave processes. Furthermore, foams can be machined into intricate parts or blown into a mold for net-shape composites. The foam properties are highly dependent on the process path and chosen precursor. Graphitic foams, for example, have been shown to attain a compression modulus of roughly 2 GPa with a low density of approximately 0.1 $g \cdot cm^{-3}$ [22]. In general, carbon foams are characterized by different combinations of low density-to strength ratio, acoustic and electromagnetic wave absorption, as well as thermal and electrical conductivity. All these properties make them excellent candidates for the design of novel material systems that include filters, electrochemical energy storage, gas diffusers, catalyst supports, templates for metallic foams, and thermal shields. Therefore, the ability to engineer foam microstructures in order to capture their full potential will have a significant impact in many engineering

applications.

Carbon-based cellular solids are a broad class of materials that includes vitreous carbon and graphitic foams, as well as foams made of Carbon Nanotubes (CNTs). Vitreous carbon is classified as non-graphitizing material composed of randomly oriented graphitic crystallites connected by disordered carbon sheets. Depending on the manufacturing process and the parent solid the pores inside the foam structure may differ in size and be open (interconnected with each other) or closed, with thin-membranes serving as cell-boundaries. There are also semi-open foam microstructures, known as Cellular Vitreous Carbon Foam (CVC) consisting of spherical cells that are interconnected by smaller circular holes on the cell-faces. One of the most studied and commercially used carbon foams is Reticulated Vitreous Carbon (RVC) which this work focuses on. A crucial element for the design of stronger foams is the understanding between (a) foam microstructure, (b) the parent solid material's fracture strength and (c) the resulting macroscopic foam strength. This process is a significant challenge, however, mainly because of the complex microstructure and the difficulty in characterizing the foamed base material and establishing its fracture strength. A widely used formula by Gibson and Ashby [23] (1982) derived from scaling arguments on an idealized microstructure, which was initially applied to elastic and plastic foams, was later used to fit measurements on brittle foams as well:

$$\frac{\sigma_{cr}}{\sigma_{fs}} = C\overline{\rho}^{n} \tag{2.1}$$

Here σ_{cr} is the foam crushing strength, σ_{fs} is the base solid fracture strength, $\overline{\rho}$ is the relative density and C, n are constants. Ashby [24] (1983) reports a value for the coefficient C = 0.65 and a power of n = 1.5 which is similar to the one previously derived (Gibson and Ashby [23], 1982) for the plastic collapse in metal foams. The same study also considers the foam fracture toughness. Several other researchers since then have used both modeling and experiments to measure the fracture toughness of both ductile and brittle lattices and foams (Maiti et al. [25], 1984; Huang and Gibson

[26], 1991; Brezny and Green [27], 1991; Choi and Sankar [28], 2003; Quintana-Alonso and Fleck [29], 2009; Alonso and Fleck [30], 2007; Fleck and Qiu [31], 2007; Combaz and Mortensen [32], 2010; O'Masta et al. [33], 2017; Kucherov and Ryvkin [34], 2014).

Brezny and Green [27] (1989) characterized ceramic foams and measured their strength and toughness. The scaling formula (2.1) was employed to fit their experimental data and a coefficient $0.13 \leq C \leq 0.23$ was found. Gibson and Ashby later used their analysis (Gibson and Ashby [4], 1999) to modify the coefficient to C = 0.2. Both works mention the scatter in the experimental results which they attribute to large variations of the foam ligaments' failure stress as well as to deviations in the assumed ligament boundary conditions. Several of the aforementioned experimental results and the scaling formula of (2.1) are shown in Fig. 2-1 (adapted from (Gibson and Ashby [4], 1999)). One can easily notice that even within the same set of experiments there are significant deviations that can reach up to an order of magnitude. Mora and Waas [35] (2002) studied the strength of brittle graphitic foams, similar to the ones examined here, and showed that the results are highly sensitive to the load-transferring conditions. In particular, they found that the strength of a foam specimen that is bonded to a thin plate by epoxy is significantly higher than the case of a specimen directly contacting the platens. Similar results were found in Letellier et al. [36] (2017) on a carbon foam using similar testing conditions and comparing the foam strength. Both studies proposed techniques to correct the experimental data in an effort to recover the true foam strength. Voigt et al. [37] (2013) examined the effect of several measurement parameters, including loading rate and specimen size, on the crushing strength of ceramic foams. Song et al. [38] (2008) performed in-situ experiments within a SEM using small-size specimens of closed-cell brittle foams to capture the fracture mechanism and analyze size effects. A recent study (Nakanishi et al. [39], 2018) examined the failure of graphitic foams. This chapter presents results from a detailed microstructure characterization and a series of uniaxial compression

tests performed on RVC foams that aim to uncover the intricate connection between processing-structure-properties for this material.

2.1 Carbon Foam Synthesis

RVC foam is a low-density open-cell structure constituted by vitreous (or glassy) carbon. The adjective reticulated means "arranged as a network". The porosity of RVC foams is typically very large (97%) leading to high values of surface area and permeability. Its rigid structure provides a low thermal expansion coefficient, wide chemical stability and high resistance to temperature in non-oxidizing environments. In addition, they have good electrical conductivity, high resistance to combustion, and chemical inertness to various acids, alkalis and organic solvents [40]. Because of these unique properties RVC foams have been used as porous electrodes [40], as filters for metal and gas filtration [41], as 3D substrates for many types of functional surface coatings [42] and active materials [43], in storage batteries [44], in semiconductors [45], as field emission cathodes [46], as bio-scaffolds for bone-tissue repairing [47], as acoustical/vibrational insulation [48], and for thermal shielding in aerospace vehicles [40].

Although foams can be fabricated by many different techniques, RVC is synthesized by carbonizing an open-cell polyurethane precursor foam which has been impregnated by a thermosetting resin [49]. More specifically, reticulated polyurethane foams [50] are first stabilized with gaseous oxygen to prevent the structure from swelling, softening, or collapsing during processing. Alternatively, the foam can be immersed in the polyvinyl alcohol solution at 80 °C. Then the water evaporates from the solution, and the polyvinyl alcohol adheres to the ligament of the foam to form a film, which will not react or dissolve in the impregnating agent in the next step. Next, the ligaments are coated with phenolic resins. The phenolic resin is cured through drying the foam. Finally, the coated polyurethane foam is pyrolyzed to a glassy carbon foam. The

final foam properties, such as density, strength, etc, can be adjusted by performing many coating steps. The above process is implemented by Ultramet Corp., to produce the RVC foam used in this study (Ultrafoam). Fig. 2-2 (a)-(d) presents scanning electron microscopy (SEM) images of 10, 30, 60, and 100 ppi samples of RVC, showing that several porosity grades with a pore size in the range 0.1 to 1 mm have a similar structure. Fig. 2-2 (e)-(f) shows the ligaments of RVC foams. It is worth noting that metals and ceramics can then be infiltrated into the carbon foam to tailor the material properties for specific applications.

The resulting properties of the RVC foam depend on many of the aforementioned manufacturing parameters including resin composition, solvent, solution viscosity, curing agent, the pore size of the precursor foam and processing temperature [51] By changing the structure of the precursor foam (i.e. linear cell number, ligament thickness, etc.) and changing the production process, one can manufacture foams with the same relative density but drastically different structures and properties, such as strengths, thermal conductivities, and permeability factors.

The impregnating resins used in polyurethane precursor foams are typically polyurethane resin, phenolic resins, epoxy resins or furfuryl alcohol. It has been found [49] that the carbonization rate of furfural-impregnated polyurethane foam is higher than that of foam injected with phenolic and epoxy resins. The glassy carbon foam, produced by mixing furfuryl alcohol with polyurethane has drastically different properties than the carbon foam coming from a polyurethane foam [52]. The pore size distribution of the precursor polymeric foam also governs the pore size distribution of the resulting carbon foam [49]. Vinton et al. [53] showed that the pore structure of RVC is almost the same as that of the precursor foam. However, Stankiewicz [54] reports the synthesis of anisotropic carbon foam with a specific cell aspect-ratio by compressing the precursor in one direction before the pyrolysis. Therefore, to obtain RVC with different cell sizes it is necessary to control the cell size during the foaming

of the polyurethane.

2.2 Microstructure Characterization of Carbon Foams

2.2.1 X-Ray Tomography

We next turn our focus on analyzing the RVC foam microstructure with the aid of micro-computed tomography (Micro-CT or µCT). Micro-CT is a powerful tool for the characterization of materials with a meso-structure (such as porous solids and multi-phase composites), in a non-destructive way. It is similar to CAT scan imaging that is extensively used in hospitals, but with a much higher resolution and more appropriate for smaller length-scales. A series of 2D planar X-ray images are captured by the µCT scanner and reconstructed into 2D cross-sectional slices. These slices can be assembled into 3D solid models, producing this way an internal view of the specimen. Micro-CT provides high-resolution 3D imaging data that enable the quantitative analysis of material microstructure, and with its non-destructive nature further allows the subsequent testing of the analyzed specimens. This technology has been extensively used in very diverse applications ranging from biomedical engineering to electronics and palaeontology.

Fig. 2-3 shows the basic steps of the computed tomography process. X-rays are generated in an X-ray source, transmitted through the sample, and recorded by the detector on the other side as a 2D projection image. The detector measures the decline rate of X-rays passing through, which depends on the distribution of density within the specimen. The sample is then rotated a fraction of a degree on the rotational stage, and X-ray projection images are taken. This procedure is iterated until the sample has rotated 180°or 360°, depending on sample type, producing a series of projection images. This series of X-ray projection images is then post-processed using a modified Feldkamp Cone Beam reconstruction algorithm, where imaging errors such

as beam hardening and ring artifacts are corrected for. To improve the quality of the imaging data one can adjust the energy (or voltage) of the x-rays when setting the scanning parameters. The largest change of X-ray energy can be achieved by using additional filters, a technique called a "coarse adjustment" of x-ray energy. Filters increase the average x-ray photon energy by selectively removing the lower energy x-rays. Typically, no filter is used for objects with a lower X-ray absorption (for low-density materials), an aluminum filter of 0.5mm is appropriate for higher energies (for medium-density materials), while the copper plus aluminum filter is often used in high-density samples. After selecting a suitable filter, sometimes it is still necessary to "finely adjust" the X-ray energy by adjusting the applied voltage to further optimize the image contrast. Each filter has a different applied voltage range with increasing contrast between high and low density corresponding to decreasing voltage. Therfore, the contrast and quality of the projected image can be improved by adjusting both the filter and applied voltage. For the RVC foams considered here, the resolution chosen is 4K, no filter is used and the X-ray voltage is 30 kV.

2.2.2 RVC Foam Morphology

We then use our micro-computed tomography system (SkyScan 1172 by Bruker) to characterize the RVC foam microstructure. Fig. 2-4 (b) shows a reconstructed 3D view of a 30 ppi RVC foam specimen. We digitally extract a cross-section of the specimen to examine its structure in more detail. The random microstructure shown in Fig. 2-5 (a) consists of polyhedral cells of nearly uniform size (i.e., the foam is essentially monodisperse) with a varying number of faces. The distribution of the varying polyhedra follows the corresponding one of the polymeric foam precursor. For the same reason, the cells are somewhat elongated along the foaming direction, in which the originally liquid foam rose as carbon dioxide gas bubbles developed within the polymer melt (approximately the vertical direction of the image in Fig. 2-5 (a)

—designated as the rise direction). The ratio of the cell-length in the rise direction to the cell-width in the transverse plane defines the foam anisotropy. The same image reveals additional manufacturing-induced defects since one can easily notice a small number of remaining closed-cells that are present within the foam. Although these cell-faces increase the macroscopic stiffness and strength of the foam, they can also affect in a negative manner its performance e.g. by reducing its permeability.

To further examine the microstructure we subsequently analyze the shape of the foam ligaments. Fig. 2-5 (b) shows a ligament that has been sectioned and extracted from a foam specimen. The ligament has a characteristic three-cusp hypocycloid cross-section known as Plateau Border. This is directly in accordance with the polymeric foam template as it was expected. Imaging sections along the ligament reveals that the cross-sectional area is not uniform through the ligament's length, but is smaller in the middle and increases as it approaches the nodes, where different ligaments intersect. This area distribution can have an important effect on the foam properties (see Jang et al.[55]). Fig. 2-6 shows a plot of the normalized area ($A(\xi)/A_0$) vs. normalized length ($\xi = x/l$) that was generated from measurements on ligaments from different foams, including polymeric, metal and carbon. Gong et al.[13] and Jang et al.[55] have used similar techniques to examine the variation of the cross-sectional area in both PU and aluminum foams and have derived two fitting functions, also shown in the same figure. Our measurements on carbon foams, indicated here with red dots that correspond on mean values, seem to be in good agreement with previous observations but with one important difference: the variation is less pronounced when moving away from the nodes, which can be attributed to the pyrolysis process.

2.3 Crushing Strength of RVC Foams

Foam specimens of different sizes are first removed from the mother block that has a relative density of about 2.5%. Small spatial gradients in density were found to be

present in the specimens and consequently, the relative density of each specimen was measured before testing. Of course, as the specimen size increases the effect of these inhomogeneities is reduced significantly. In order to connect the foam strength to the underlying microstructure and identify any potential deviations induced by the domain-size and/or the experimental apparatus, we perform compression tests using three different experimental set-ups. In the first one, the free-boundary test shown in Fig 2-7 (a), foam specimens are crushed directly between the loading stage platens. In the second one, the fixed-boundary test shown in Fig. 2-7 (b), two thin aluminum plates are adhered to the foam before testing. Finally, we perform in-situ compressive experiments in smaller specimens using a loading stage within the micro-CT as shown in Fig. 2-7 (c). This process allows scanning the specimens at several intervals during crushing.

2.3.1 Free-Boundary Crushing

Cubical specimens of 2-inch edges (Fig 2-8 (a)) and different cell-size (30ppi, 65ppi, and 100 ppi) are used in crushing tests in order to extract the complete compressive response of the carbon foam. An MTS Criterion Series 40 testing stage is used and the displacement rate chosen is $\dot{\delta}/h_0 = 8.33 \times 10^{-5} s^{-1}$ which corresponds to the strain rate when the deformation is homogeneous (h_0 is the height of the specimen).

Fig. 2-8 (b) shows three characteristic nominal stress-displacement curves from different foam specimens. They correspond to three samples with nearly equal relative densities but different cell-size, i.e. $\overline{\rho}_{ave} = 2.31\% \pm 0.04\%$ for 30ppi, $\overline{\rho}_{ave} = 2.74\% \pm 0.10\%$ for 65ppi and $\overline{\rho}_{ave} = 2.37\% \pm 0.10\%$ for 100ppi. One can easily notice several key features that are common in the compressive response of most foams and many other cellular solids. The response starts as linear elastic and then terminates at a limit critical stress that corresponds to the foam strength. It then follows a constant stress-plateau that extends to average strains of about 80%. The response

then enters the densification regime with additional compaction of the crushed foam. What distinguishes however this macroscopic stress-strain curve to corresponding ones of metal and polymer foams is the dependence of the stress-plateau, and thus the foam strength, on the cell-size. Unlike the mostly independent relationship between ppi and strength in other types of foams, here we notice a very strong effect as shown in Fig. 2-8.

Several experiments were subsequently performed for each cell-size to examine the variations caused by the randomness of the microstructure and inhomogeneities such as density gradients, cell-anisotropy and remaining closed-cell faces within the specimens. Fig. 2-9 shows three compressive responses for the 30ppi RVC foam. One can easily notice that the deviation between the force-displacement curves is rather minimal. The responses reach a mean critical stress $\sigma_{cr} = 13.27 \pm 0.59 psi$ at a macroscopic strain $\varepsilon = 2.72\% \pm 0.09\%$. Then the response drops slightly to a mean plateau stress $\sigma_{pl} = 12.67 \pm 1.17 psi$. During the load plateau, rows of cells are crushed through the brittle fracture of ligaments and the successive breaking of cells causes the ruggedness of the response. It was observed that the deformation appeared to be mostly near the boundaries where the foam contacts the platens. At the end of the plateau, the remaining intact boundary cells combined with fallen broken fragments are compacted together leading into densification and a second stiffening part of the response.

Fig. 2-10 and Fig. 2-11 show respectively the corresponding set of responses for the 65ppi and 100ppi foams. The trend for all responses is similar to the one described for the 30ppi foam, albeit at different stress levels. For 65ppi, the critical stress is $\sigma_{cr} = 18.55 \pm 4.88 psi$ at a macroscopic strain $\varepsilon = 3.52\% \pm 0.09\%$ and the mean plateau stress is $\sigma_{pl} = 21.30 \pm 1.97 psi$. For 100ppi, the response reaches a higher critical stress $\sigma_{cr} = 44.68 \pm 4.56 psi$ at strain $\varepsilon = 4.46\% \pm 0.167\%$ and the plateau stress is $\sigma_{pl} = 44.09 \pm 5.13 psi$. Fig. 2-12 shows the plateau-stress as a function of the cell size

from all experimental measurements. An optimal power-law fit, included in the same figure with a solid line, reveals that the foam strength is inversely proportional to the cell-size, i.e. $\sigma_p = 0.41 l^{-0.99}$ (with R = 0.93594).

2.3.2 Fixed-Boundary Crushing

Previous works [35][36] have reported a dependence between the measured strength of brittle foams and the load distribution at the boundary. To examine this effect we performed experiments on foam specimens with metal plates attached to them. In particular, thin aluminum plates with a 0.025 inch thickness were bonded to two foam edges, as shown in Fig. 2-7 (b). A J-B Weld ExtremeHeat™ paste was used to bond the plates to the foam and the epoxy was cured at room temperature for 24 hours. Fig. 2-13 shows a set of compressive responses corresponding to fixed-boundary 65ppi specimens along with a free-boundary response (dashed line). It is easy to notice that the plate-induced support at the boundary foam-cells altered the response significantly. The first load peak, corresponding to foam strength, is higher than before at a stress 68.50 MPa. It is then followed by a significant drop indicating extensive failure within the specimen. However, with additional compaction the response rises again reaching the original plateau stress. Unfortunately, the strength increase induced by the constrained boundaries couldn't be quantified because of the large deviations in the responses, that we attribute here to the imperfect bonding between the carbon foam and the aluminum plates. We show in the next chapter that the true foam strength can be measured accurately if a perfectly fixed boundary is achieved.

2.3.3 In-Situ Crushing

In all experiments reported so far, the deformations are monitored through a camera facing the specimen which makes it difficult to establish the presence of any damage in the interior. For this reason, we perform a series of in-situ displacement controlled

experiments using an MTS loading stage within the micro-CT. Specimen-holder constraints dictated the machining of smaller cylindrical specimens having a 15mm diameter and 19mm height (see Fig 2-14 (a)). The stage is equipped with load cells with different ranges (40-440N) and a measurement error within 1% of the full scale of the load cell. For the results presented here, a 440N load-cell is used and the applied displacement rate is 0.00015/second. In this set-up, the specimen is crushed in increments of about 9%. After each increment, the compression is paused and the specimen is scanned so that several 3D images of the foam are captured at different macroscopic strains. Fig 2-14 (b) shows the response recorded for the three different cell-sizes. Despite the smaller specimen size, corresponding to fewer foam cells within the domain, the levels of the load-plateaus are close to the free-boundary responses reported before. The evolution of damage within the foam is shown for the 65ppi specimen in Fig 2-15. The images correspond to the points indicated on the response with circled numbers. The tomography analysis confirms that in the free-boundary set-up damage initiates and propagates at the moving boundary, crushing the foam cells row-by-row. Several in-situ tests were performed and the results are reported in Fig. 2-16 to Fig. 2-18. As aforementioned, although the stress levels are similar to the responses recorded for the larger specimens, the undulations during the plateaus in this case are more pronounced due to the smaller number of cells and the accuracy of the load cell. Note that bonding thin plates on these cylindrical specimens in order to perform in-situ fixed-boundary type tests was not possible due to practical constraints.

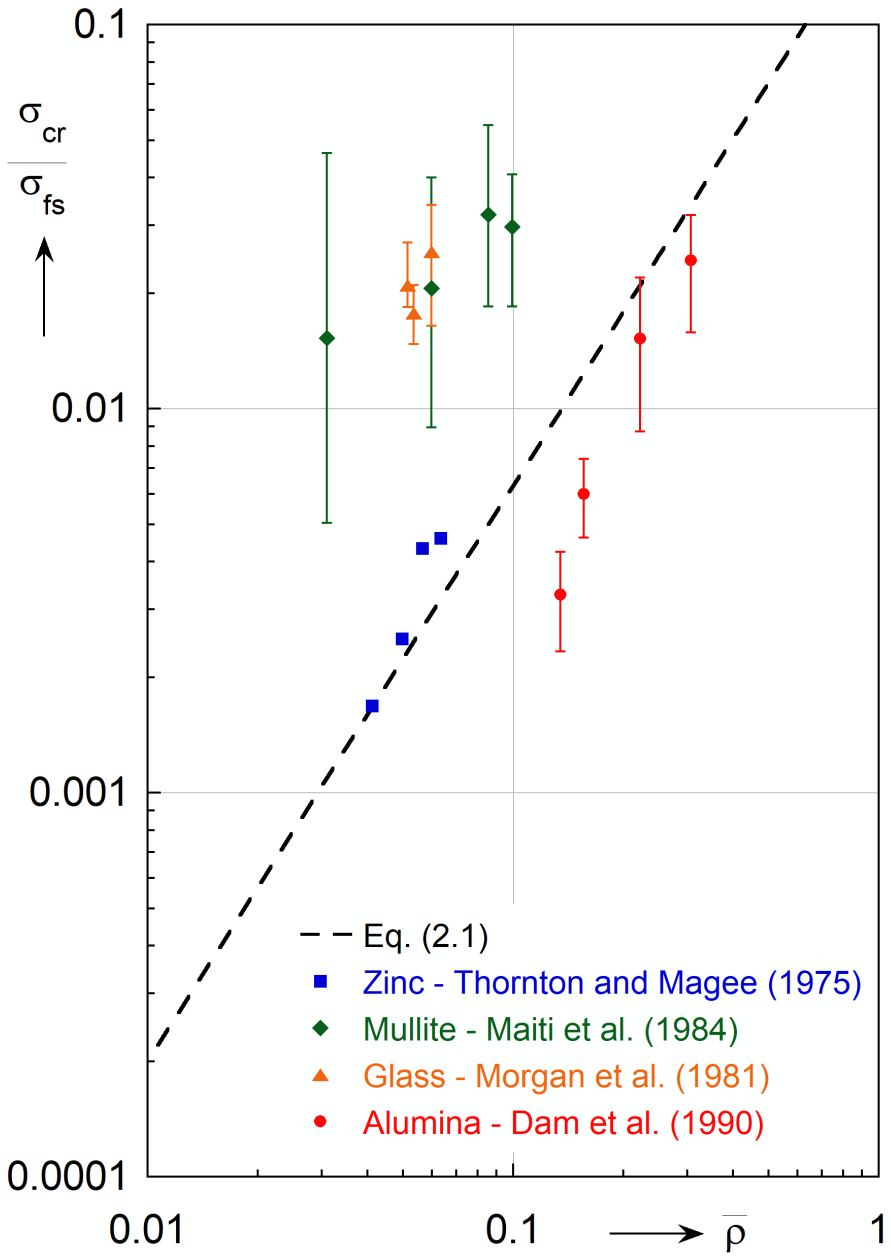

Figure 2-1. Crushing strength of brittle foams against relative density (adapted from (Gibson and Ashby [4], 1999)).

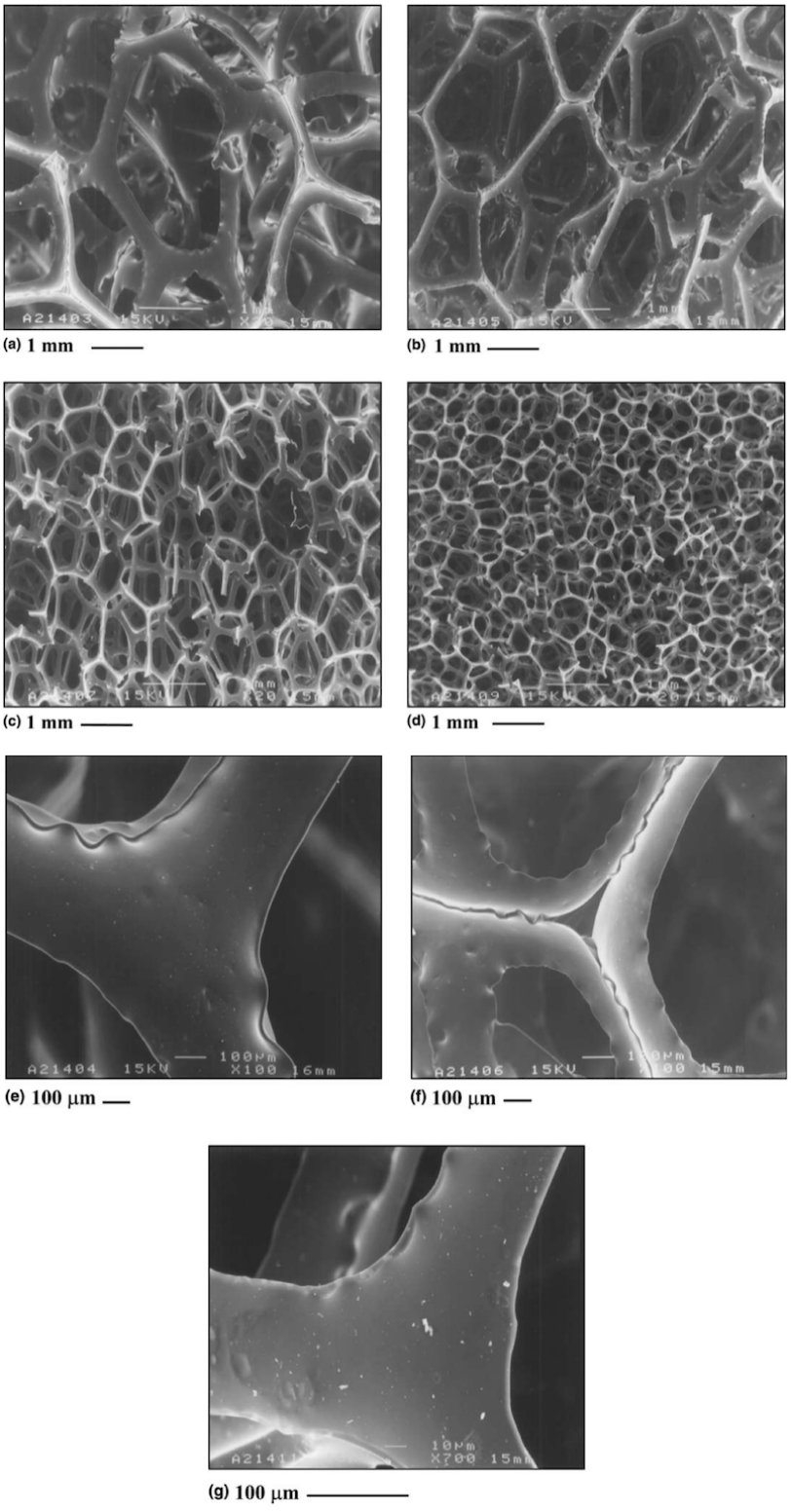

Figure 2-2. SEM micrographs of: (a) 10, (b) 30, (c) 60 and (d) 100 ppi RVC samples. Closeups of struts for: (e) 10, (f) 30 and (g) 100 ppi RVC samples. [49]

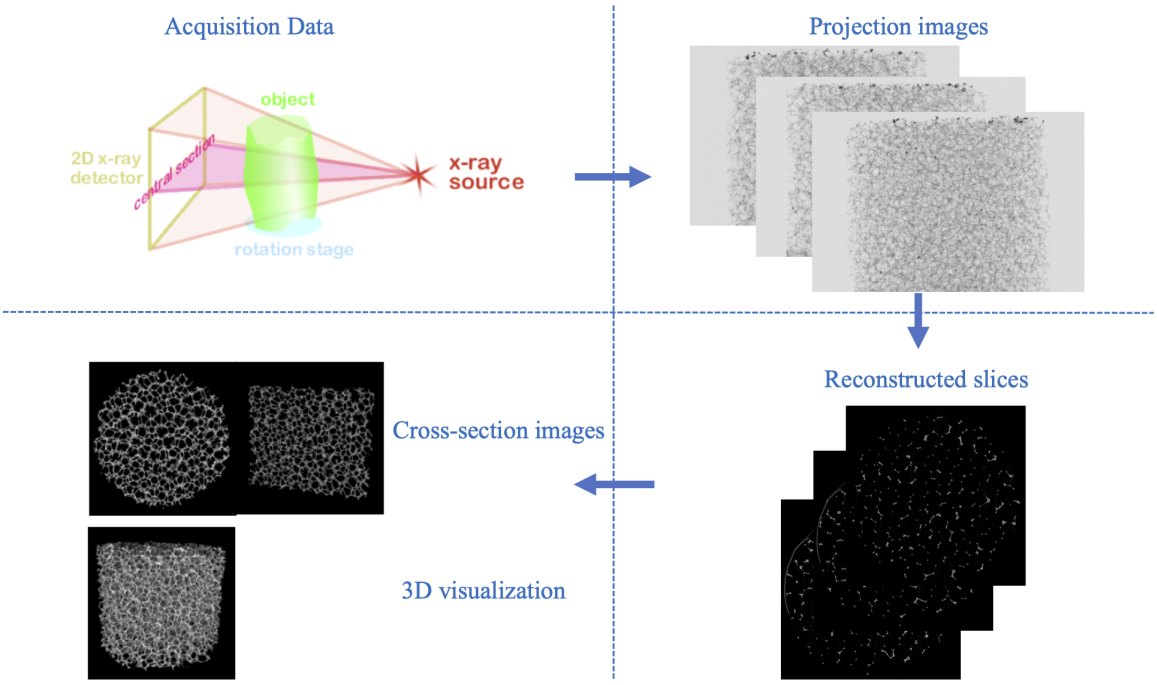

Figure 2-3. Schematic of microcomputed tomography analysis: scanning, reconstruction, and image processing.

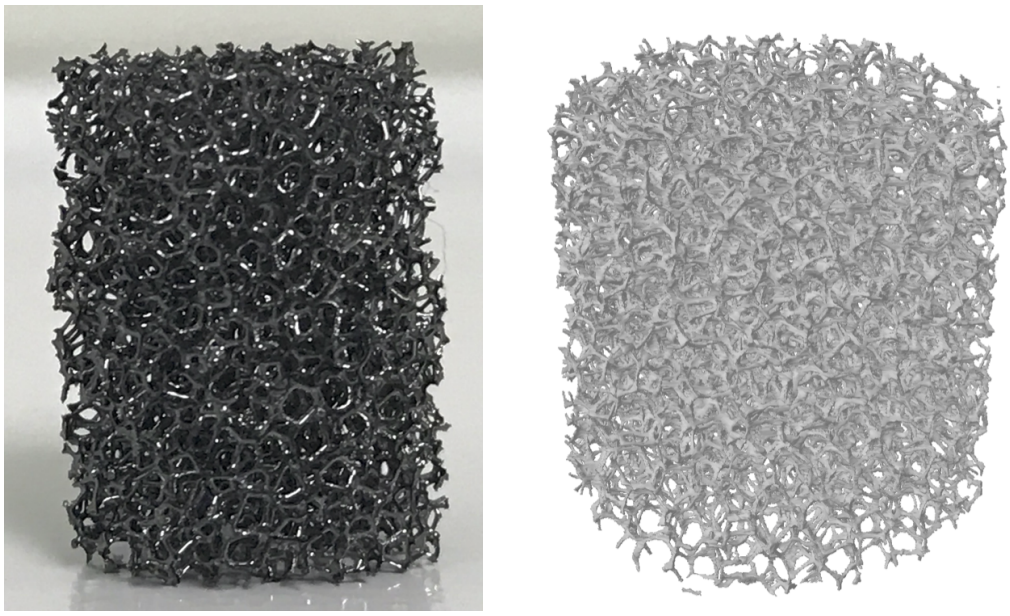

(a) (b)

Figure 2-4. (a) 30ppi open-cell RVC foam specimen and (b) Reconstructed 3D solid model.

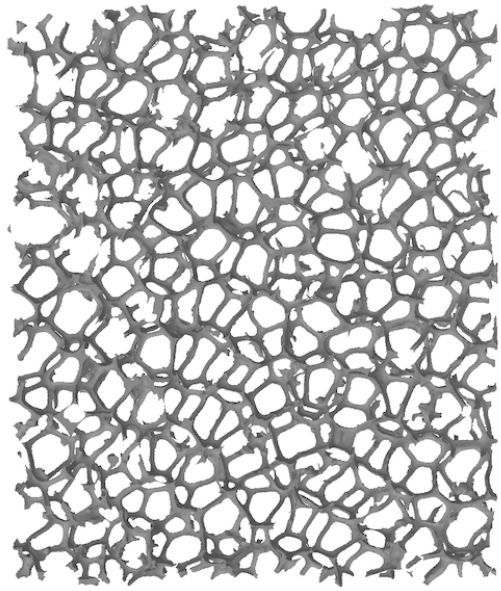

(a)

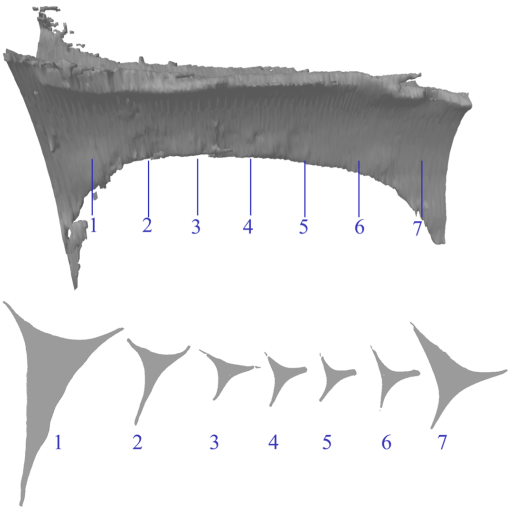

(b)

Figure 2-5. (a) Microcomputed tomography image of 30 ppi RVC foam (b) Ligament and cross section.

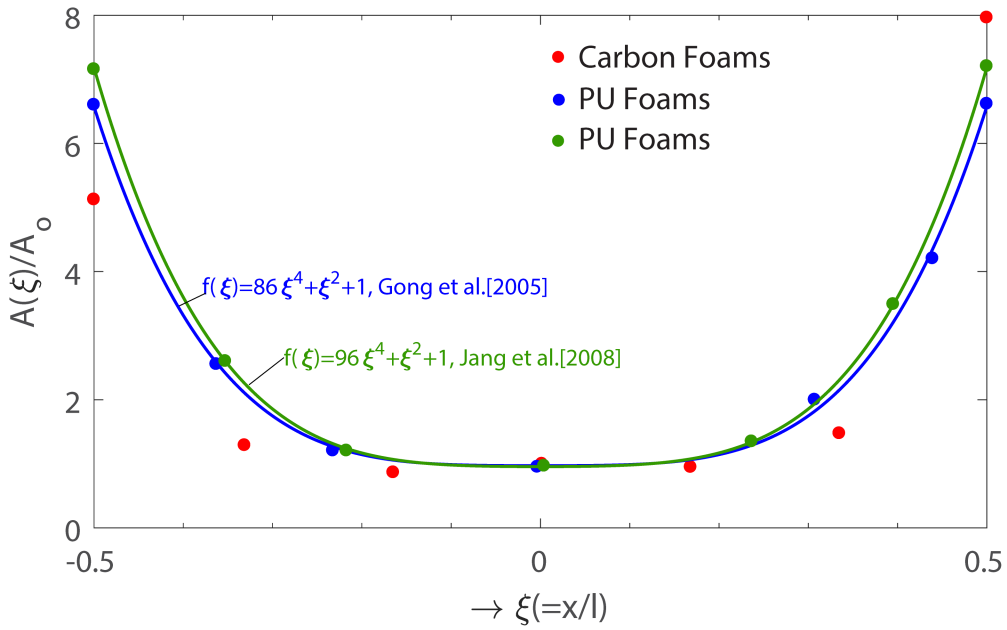

Figure 2-6. Measured variation of foam ligament cross-sectional area along the length fitted with function $f(\xi)$ (with data from [13] [55]).

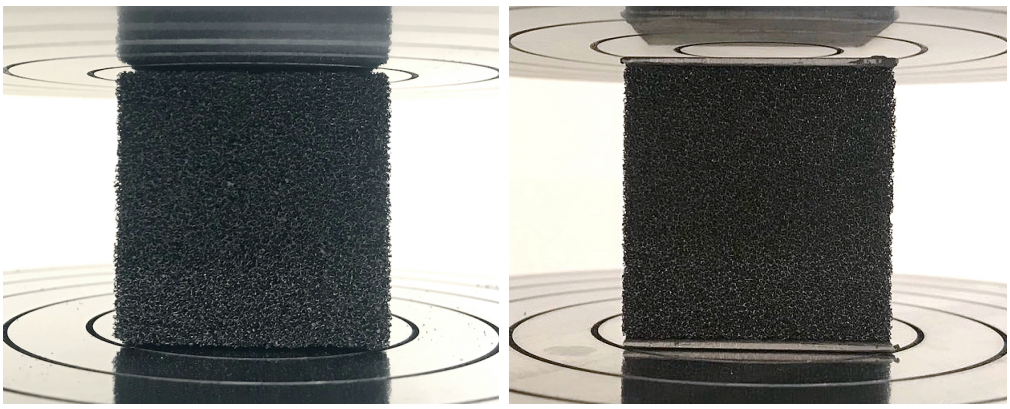

(a) (b)

(c)

Figure 2-7. Set-ups for crushing experiments: (a) free-boundary compression (b) constrained-boundary compression (c) in-situ testing.

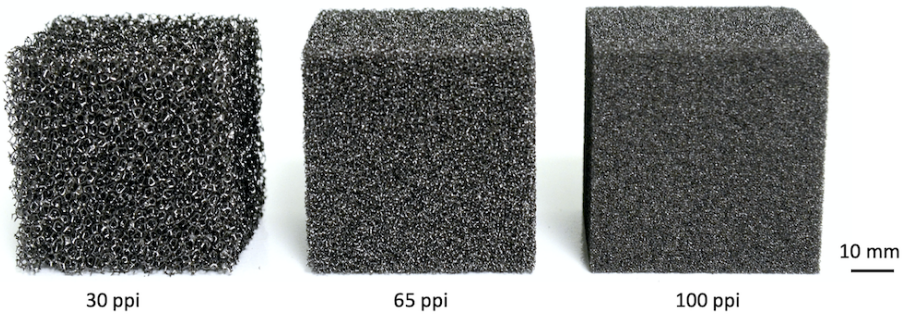

(a)

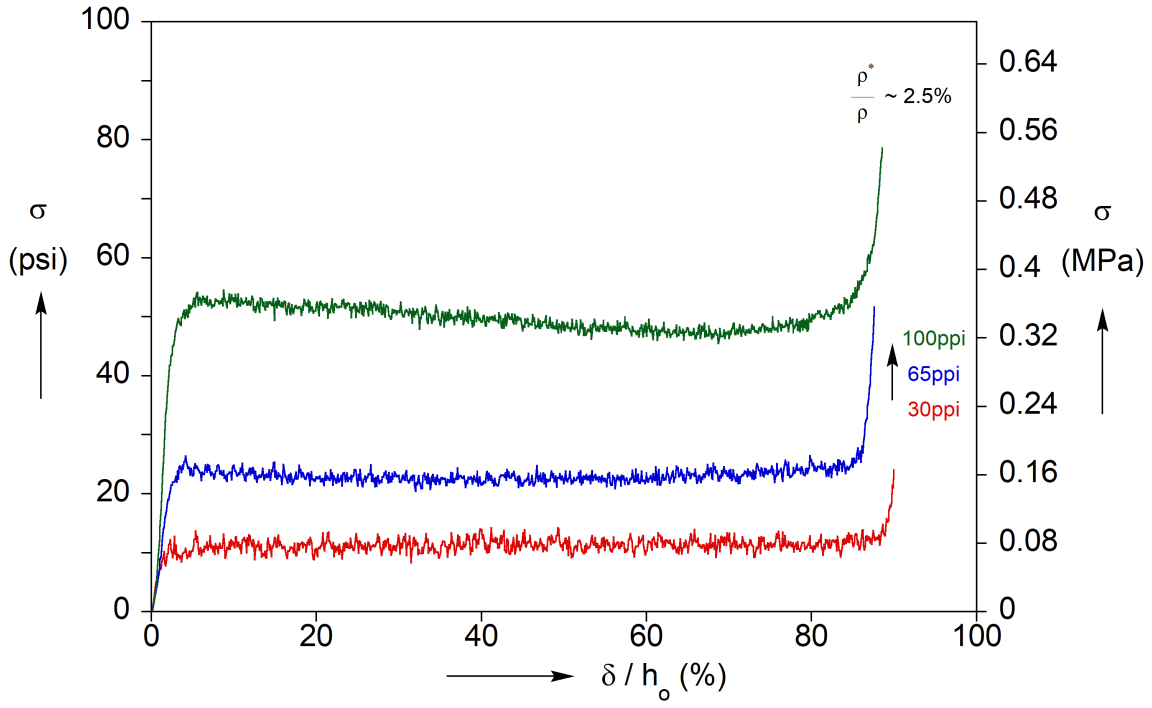

(b)

Figure 2-8. (a) Cubical RVC foam specimens with different cell-size (b) Nominal stress vs. normalized displacement responses.

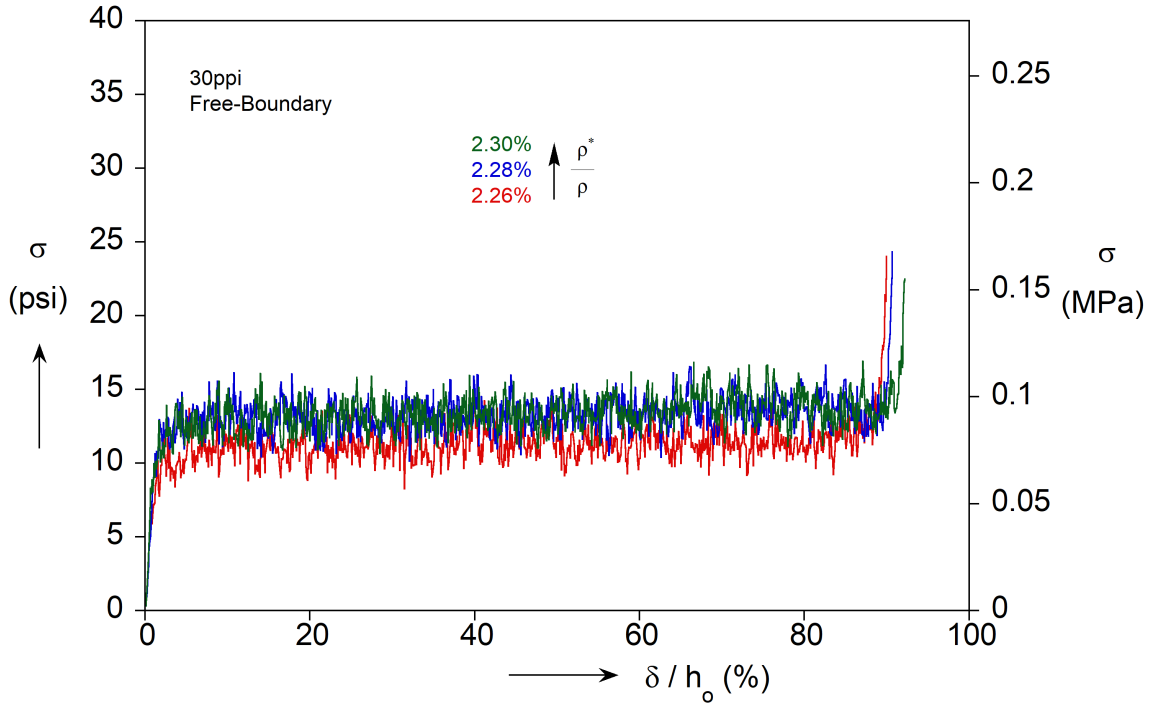

Figure 2-9. Compressive responses for 30ppi RVC foam.

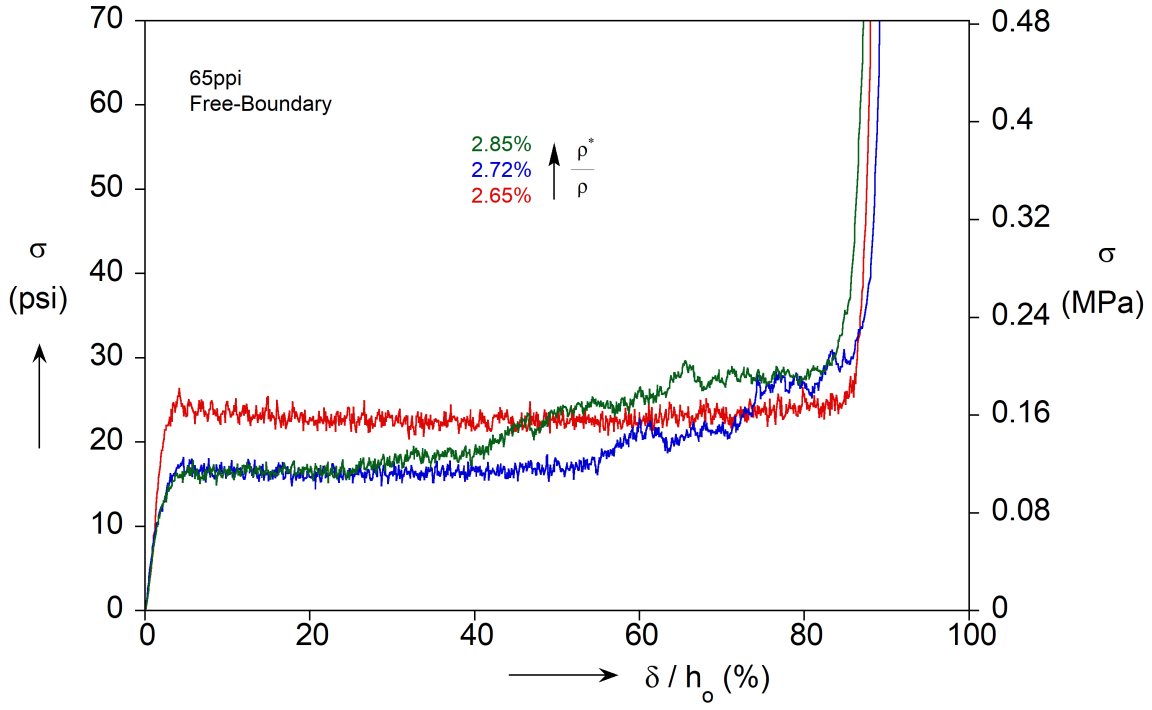

Figure 2-10. Compressive responses for 65ppi RVC foam.

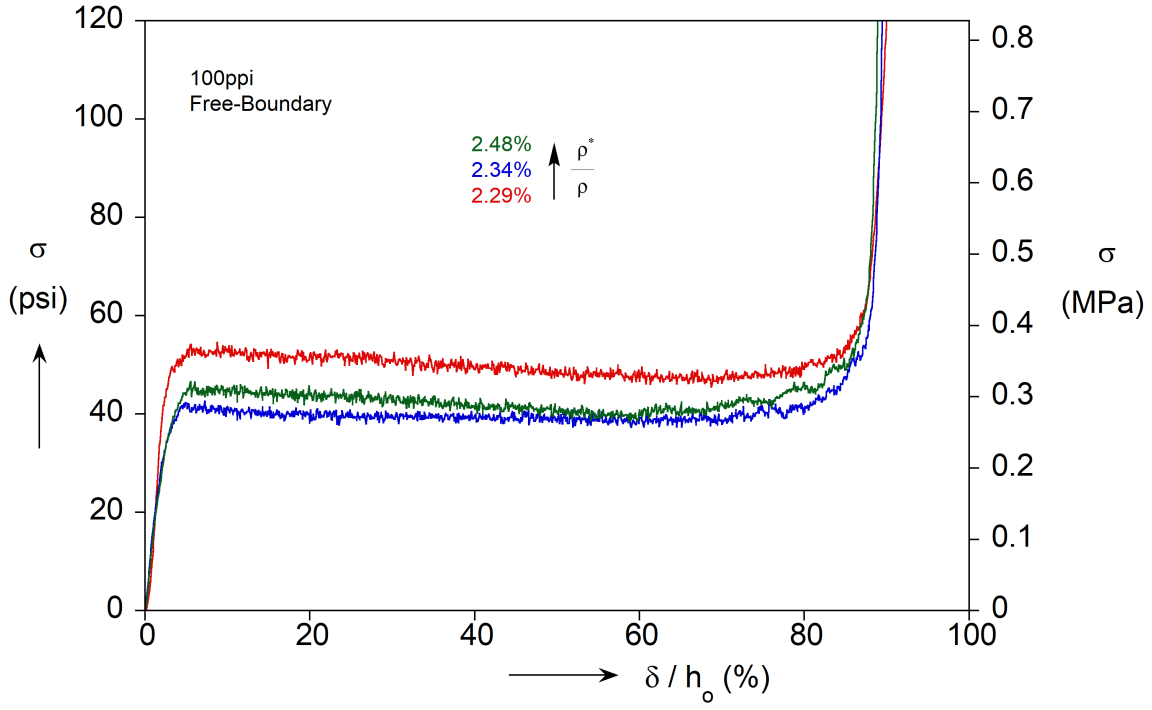

Figure 2-11. Compressive responses for 100ppi RVC foam.

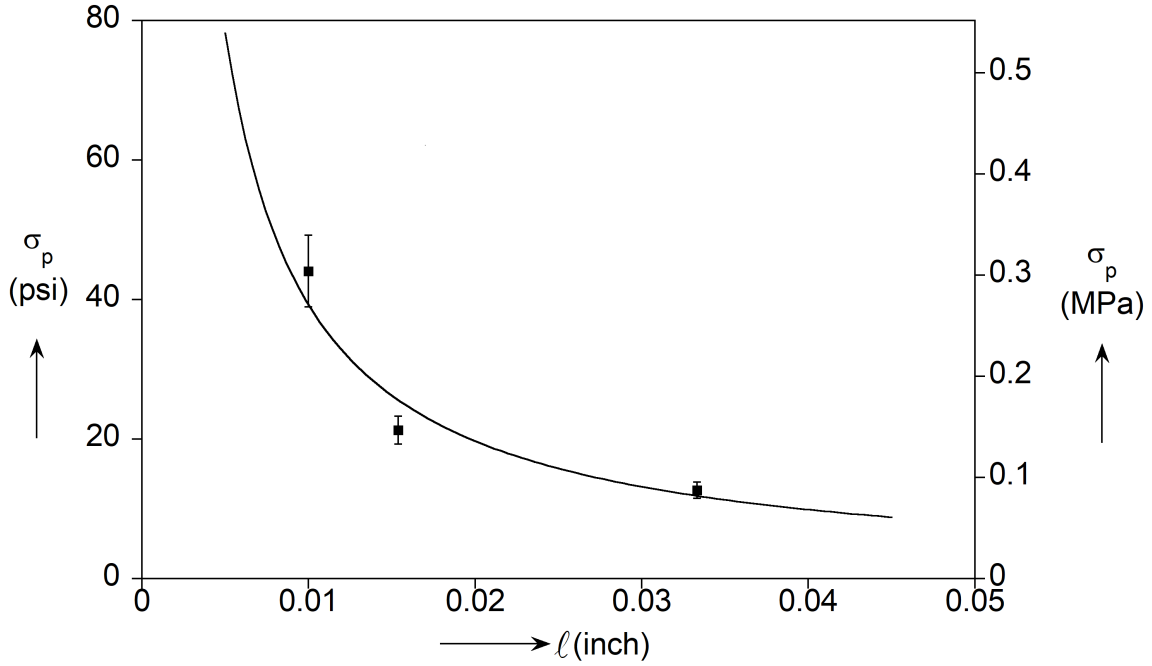

Figure 2-12. Plateau stress vs. cell-size.

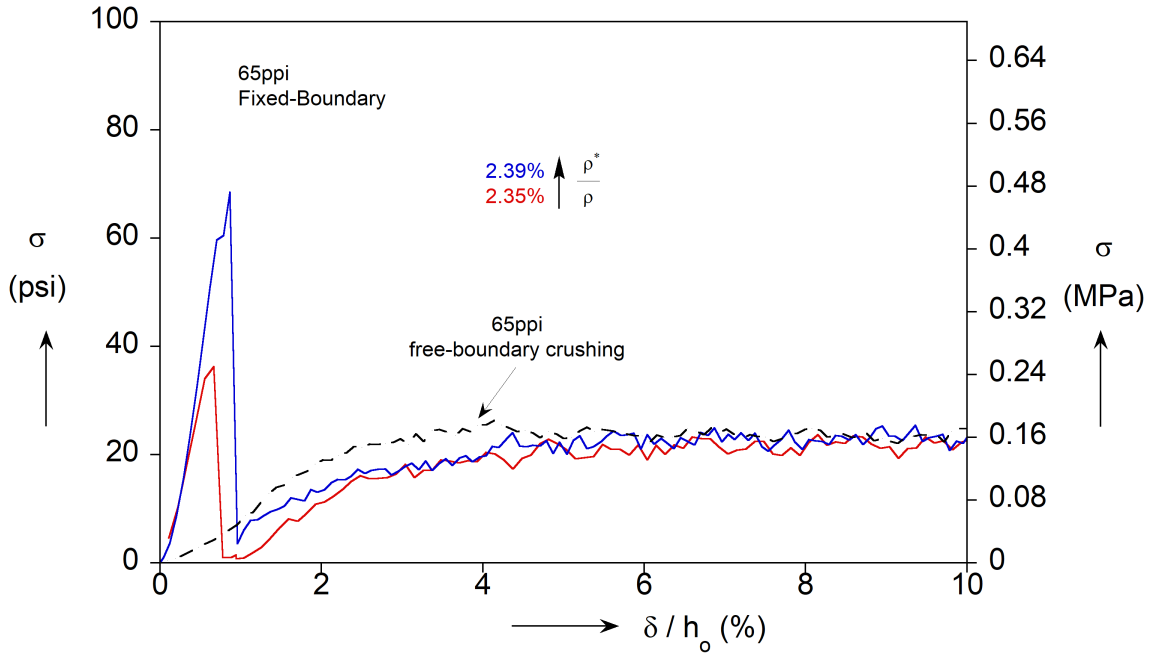

Figure 2-13. Compressive response for 65ppi specimens with fixed boundary.

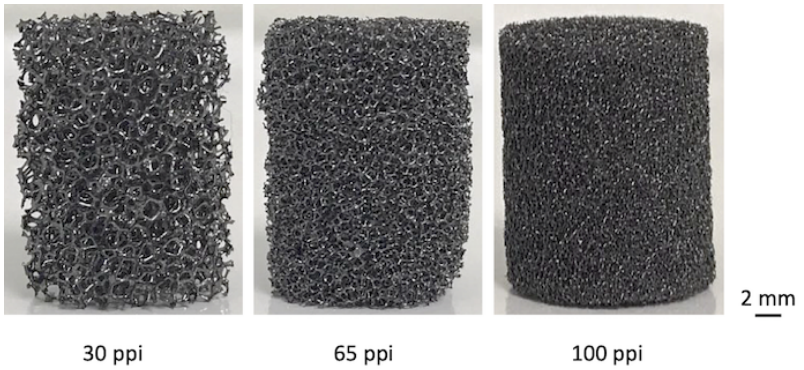

(a)

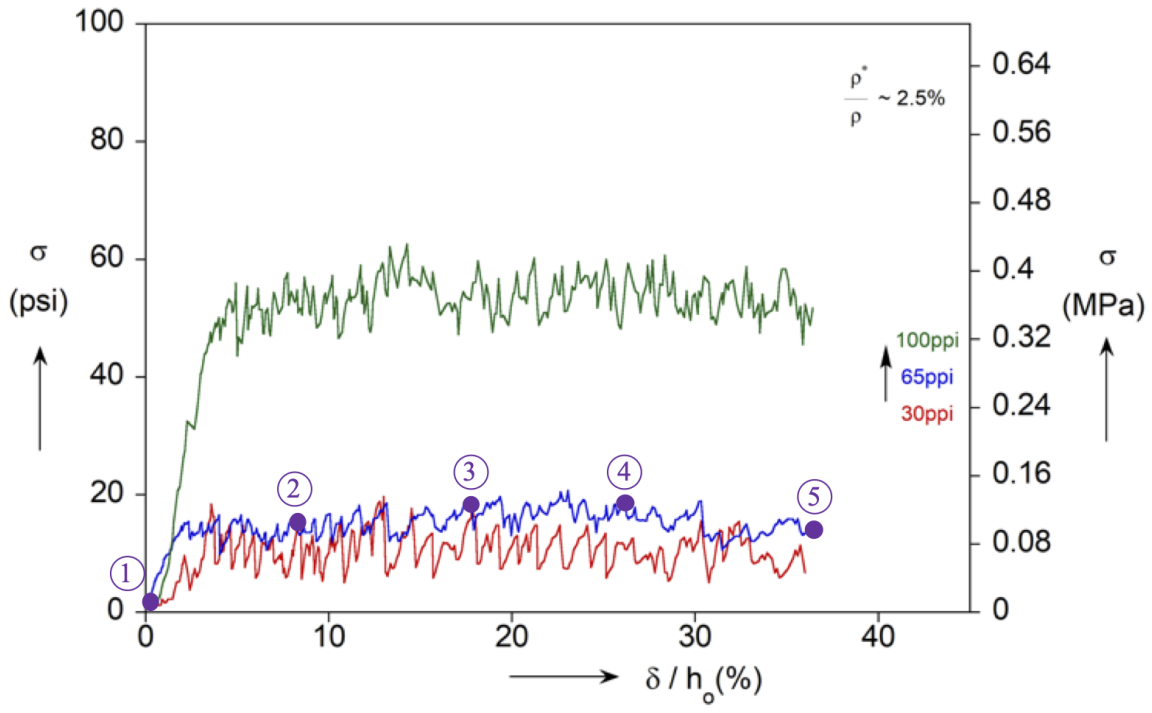

(b)

Figure 2-14. (a) Cylindrical RVC foam specimens for in-situ testing (b) Compressive response for foam specimens with different cell-size.

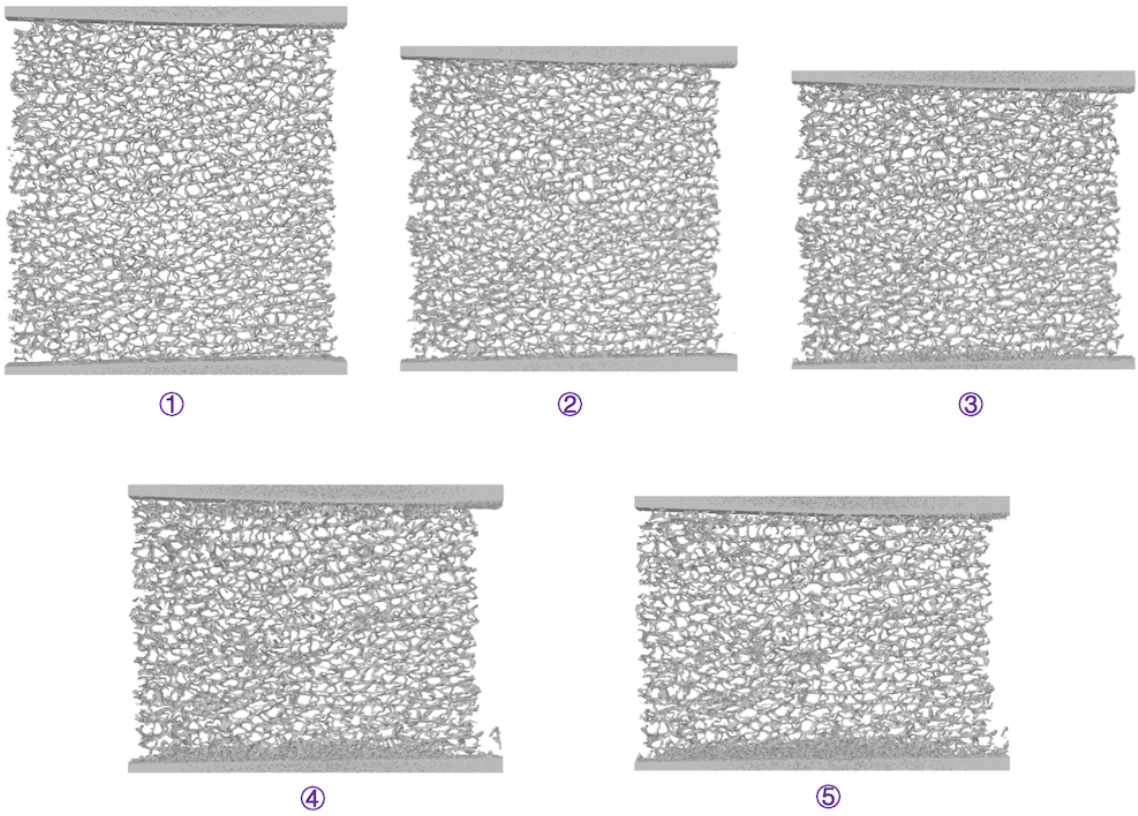

Figure 2-15. Sequence of deformed configurations corresponding to points marked on the 65ppi response in Fig. 2-14 (b)

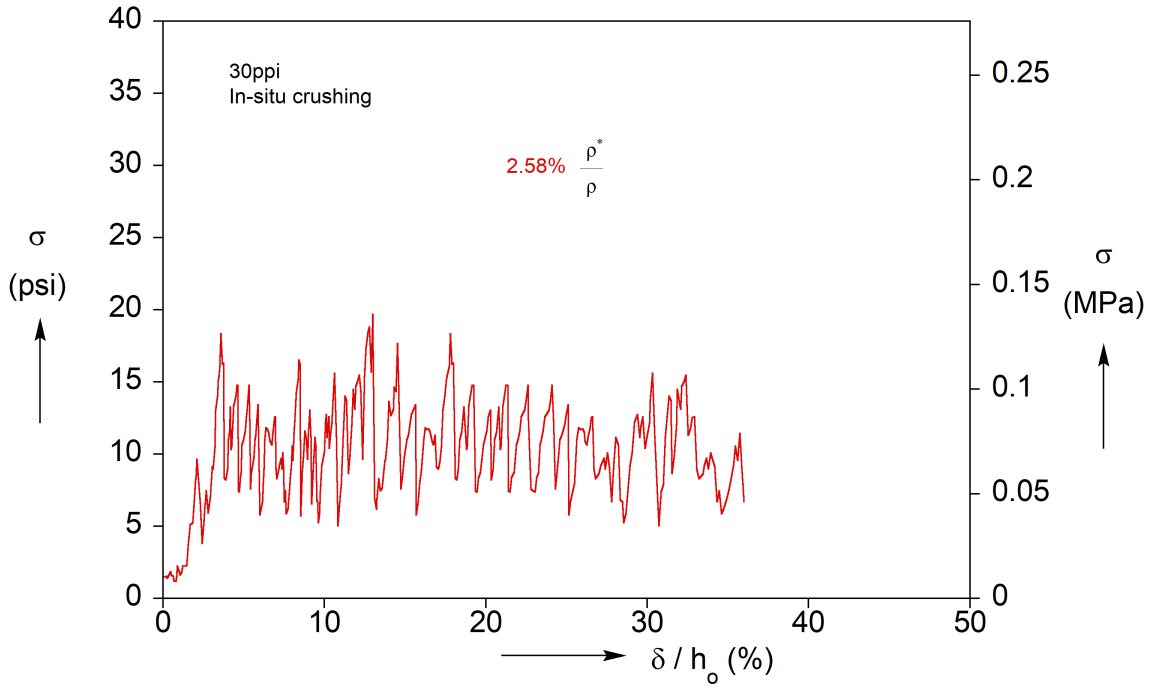

Figure 2-16. In-situ compressive response for 30ppi foam.

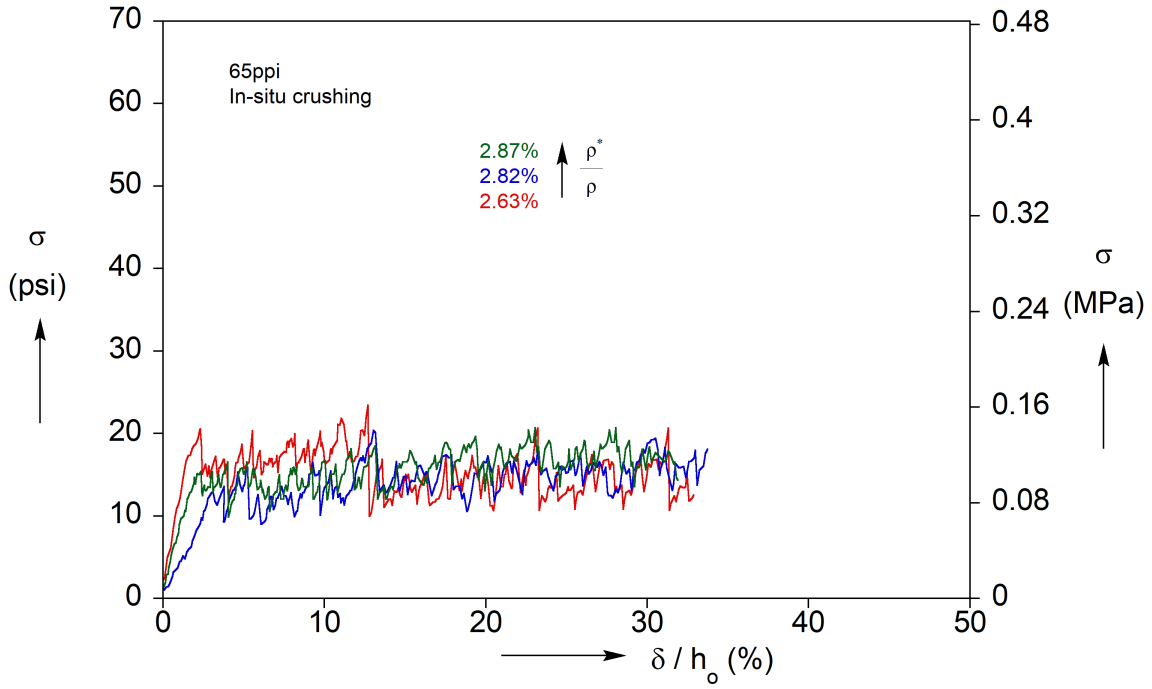

Figure 2-17. In-situ compressive response for 65ppi foam.

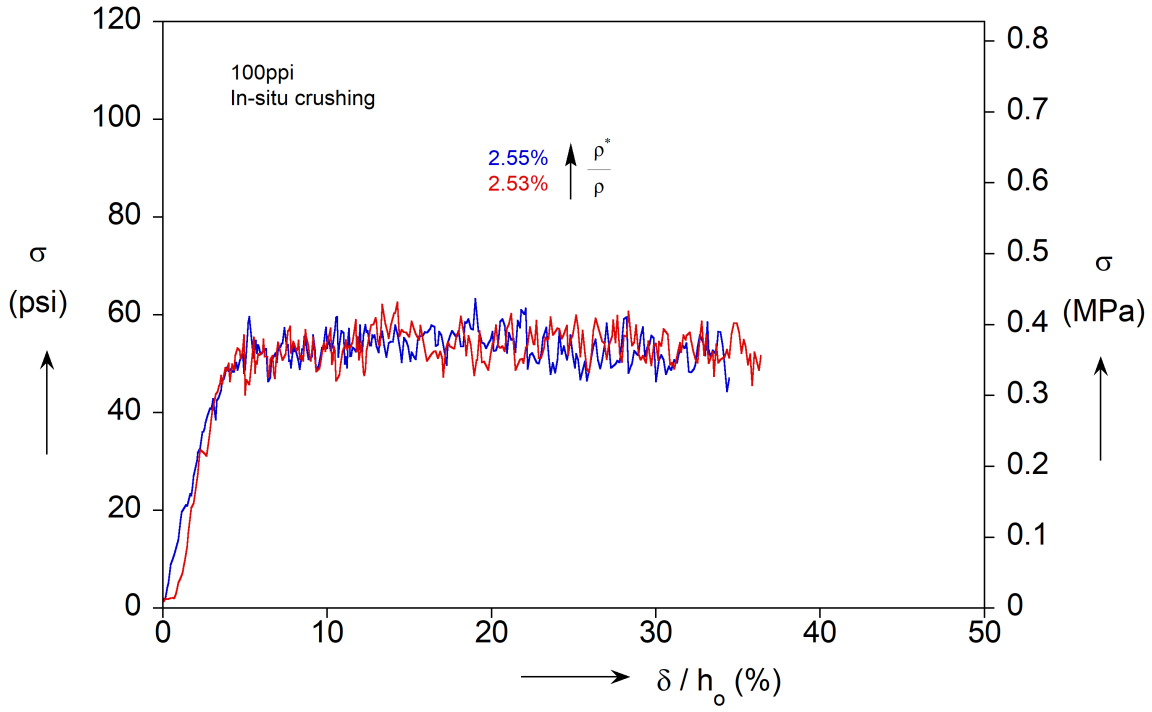

Figure 2-18. In-situ compressive response for 100ppi foam.

Chapter 3

Additive Manufacturing, Characterization and Crushing of Brittle Polymeric Foams

It is clear that the complexity of the brittle failure of cellular materials is directly correlated to the intricate connection between microstructure and base material failure. In recent years there has been a continuously increasing number of works that take advantage of additive manufacturing as a means to study cellular materials with enhanced control over microstructural characteristics. Hernández-Nava et al. [56] (2015) used a tomography-based three dimensional structure to design stochastic foams of different relative densities, but with the same underlying topology, and subsequently synthesize metal foams by additive manufacturing. Yang et al. [57] (2018) manufactured and tested gyroid titanium alloy microstructures using selective laser melting (SLM). In Seiler et al. [58] (2019) brittle honeycombs made by rapid prototyping were tested under tensile loads and the effect of designed and manufacturing-induced imperfections on the resulting strength was examined. The influence of imperfections and disorder on deformation and fracture of lattices made by Fused Deposition Modeling (FDM) was studied recently in Xu et al. [59] (2019). In Latture et al. [60] (2018) lattices with filleted nodes were synthesized to measure the effect on the compressive response. Several recent studies have focused on both static and dynamic load with a focus on

energy absorption. Ling et al. [61] (2019) tested lattices made of one tough and one brittle resin material, while Tancogne-Dejean et al. [62] (2016); Amani et al. [63] (2018) combined experiments and modeling to examine the behavior of metallic lattices made with selective laser melting. In Wang et al. [64] (2018) closed-cell polylactide foams were fabricated by FDM and foam strength was found to depend on the layer deposition strategy.

This chapter focuses on the synthesis and characterization of brittle open-cell foams with controlled morphological features [65]. Laguerre tessellations are used to create random foam topologies which are then additively manufactured by stereolithography (SLA). The base material used is a high-temperature photopolymer with low fracture strain, i.e. elongation at break. Over-curing is used to enhance the brittleness of the solid. In-situ experiments are performed in dog-bone 3D-printed specimens to measure the parent solid's stress-strain response and the associated microscopic fracture strength. The microstructure of foam specimens is analyzed using microcomputed tomography in order to quantify manufacturing-induced morphological deviations. We subsequently perform a series of compression experiments to measure the foam crushing strength and relate it to the loading conditions and the underlying microstructure. Scaling the ligaments' cross-sections enables the measurement of the crushing strength against relative density.

3.1 Additive Manufacturing of Open-Cell Foams

3.1.1 Generating Virtual Foam Microstructures

Our first foal here is to create realistic open-cell foam microstructures that share the key morphological characteristics of commercial foams but with minimal synthesis-induced imperfections and practically eliminating any anisotropy, closed- faces, and/or broken struts that are always present in conventional foaming processes. The numerical

framework (see Fig. 3-1) for generating open-cell foam topologies (Kraynik et al. [66], 2003; Kraynik et al. [67], 2004) starts with a dense sphere packing produced by molecular dynamics. The packing can be either monodisperse, i.e. with equal sphere volume, or polydisperse depending on the target microstructure. The sphere packing is used to create a Laguerre tessellation which is then introduced as an initial condition in a surface-area minimizing code, the Surface Evolver (Brakke [68], 1992). The total surface area of the polyhedral topology is then minimized under the constraint that cell volumes remain constant and equal to the corresponding ones of the initial Laguerre polyhedra, while spatial periodicity is conserved in the boundary cells. The Surface Evolver simulations produce random soap froth with curved 2-D surfaces as cell faces. This equilibrium foam structure satisfies Plateau's laws: (Plateau [69], 1873) (I) the cell faces are surfaces of constant mean curvature; (II) three faces meet a cell edge at equal dihedral angles of 120°; and (III) four edges meet a cell vertex at the tetrahedral angle, $\cos -1(-1/3) = 109.47°$. An "annealing" process, involving large-deformation tension-compression cycles, produces additional topological transitions and further relaxes the topology that now resembles a closed-cell foam (see Fig. 3-1 (c)). Finally, an open-cell foam structure is generated by joining the cell vertices with straight lines and removing all cell faces. The resulting topological characteristics of the numerical foam are in excellent agreement with experimental measurements on foam bubbles (Matzke [70], 1946). The comparison involves all relevant microstructural features including the statistics of the number of faces per cell, the distribution of cells with n-faces, surface free energy density, and foam-cells population (Kraynik et al. [66], 2003). Furthermore, due to the foaming manufacturing process, the similarity between morphological characteristics has been shown to hold for commercial foams too (Jang et al. [55], 2008). This type of microstructure modeling framework can also be used to develop micromechanically accurate finite element models. Such three-dimensional mesoscale models have been proven to accurately predict the mechanical

response of commercial metal foams under both static and dynamic loads (Gaitanaros et al. [17], 2012; Gaitanaros and Kyriakides [71], 2014; Bayat and Gaitanaros [72], 2019; Yang and Kyriakides [73], 2019) as well as to quantify the uncoupled effect of specific microstructural features on the foam macroscopic properties (Gaitanaros and Kyriakides [74], 2015; Gaitanaros et al. [75], 2018). Note that one can introduce, if needed, additional observed morphological features such as the one reported in Chapter 2, i.e. foam anisotropy and ligaments having non-uniform cross-sectional areas.

3.1.2 Foam Synthesis by Stereolihography

Cubical models of monodisperse topologies with N^3 cells are generated using the preceding framework. Fig. 3-2 (a) shows the skeletal structure of such a soap froth with 1000 cells, which is the precursor to the open-cell foam. The coordinates and connectivities of all nodes and edges are imported in nTopology, which is a design software focusing on lattice materials, and subsequently all edges are assigned a uniform circular cross-section. Different foam relative densities can be attained by controlling the value of the cross-sectional area (Fig. 3-2 (b). An iterative process is followed to achieve the maximum accuracy for the relative density, accounting for the material overlap at the nodes. There is always some error introduced by the meshing algorithm of the final structure, but that is typically less than 1%. The ligament connections close to the nodes are smoothed to avoid any imperfections and stress concentrations during mechanical loading. Fig. 3-2 (c) shows a close-up view of the node connection in a cluster of 3 foam cells.

The resulting 3D foam model is synthesized using a stereolithography-based printer (Form2 by Formlabs) with 50 μm layer thickness using a high-temp photocurable resin (see https://archive-media.formlabs. com/upload/HighTemp-DataSheet-v1.pdf). Stereolithography (SLA) uses an ultraviolet (UV) laser beam on the resin to initiate

a chain reaction where UV- active monomers convert to polymer chains. After polymerization, a pattern inside the resin layer is solidified in order to hold the subsequent layers. The base material was chosen for its nominal elongation at break which is about 2%. Our post-processing protocol involves washing in isopropyl alcohol for 15 min in order to clean liquid resin off of the 3D-printed foams, followed by UV-curing for 120 min in 60 °C. All specimens were over-cured in order to increase their brittleness. The foams were synthesized using the same printing orientation and layer thickness to maintain consistency over the resulting mechanical properties.

3.1.3 Base Material Properties by In-Situ Testing

Extracting the mechanical properties and failure stress of the base parent solid is very important in order to understand the macroscopic foam failure. This, however, is not a trivial task. Several works [76] [77] have reported that the mechanical behavior of the material within the ligaments is different that the original, pre-foamed, solid because of the thermomechanical treatment. Here, the mechanical properties of the underlying solid were examined using in-situ micro-tensile testing on 3D-printed dog-bone specimens with diameters matching the cross-sectional area of the foam ligaments. Fig. 3-3 (a) shows the dimensions of a typical dog-bone specimen while Fig. 3-3 (b) shows a sketch of the ligament in the loading stage that operates within the micro-CT. Several characteristic stress-strain curves of the base material under tension are reported in Fig. 3-4. The tests confirmed the brittleness of the photopolymer with x-ray imaging (see Fig. 3-5) showing the ligament breaking abruptly with minimal plastic deformation before failure. The stress-strain curve is slightly nonlinear until fracture occurs and the stress drops to zero. The cured photopolymer was found to have an average fracture strength $\sigma_{fs} = 62.58 \pm 4.91$MPa at a corresponding failure strain $\varepsilon_{fs} = 3.15 \pm 1.47\%$. Note that Formlabs reports an ultimate fracture strength of 51.1 MPa under tension. We attribute the difference with our results to the smaller

size of our specimens which is known to cause an increase in strength that is typical for brittle materials. Furthermore, increased UV exposure has also been shown to affect the properties of 3D-printed specimens.

3.2 Microstructure Characterization and Synthesis-Induced Variations

The photopolymerization process typically leads to volume shrinkage and curl distortion that depends on many synthesis parameters such as scanning speed and path, pitch, and thickness among others (Huang and Lan [78], 2006). In order to quantify any variations in the 3D-printed microstructure, that result from our synthesis protocol that was described in the previous section, we characterize the foams using tomography and image analysis (Rhino3D). Figs. 3-6 (a) and 3-6 (b) show a solid model of a foam with 43 cells and the scanned reconstruction of the 3D-printed sample. The two microstructures appear to be almost identical however a more detailed and quantitative analysis is needed to calculate any deviations.

A global comparison between target and synthesized architectures can be performed by calculating the Hausdorff Distance

$$\mathrm{d}_H(X,Y) = \max\left\{\sup_{x\in X}\inf_{y\in Y}\mathrm{d}(x,y), \sup_{y\in Y}\inf_{x\in X}\mathrm{d}(x,y)\right\} \tag{3.1}$$

of the corresponding meshes (this functionality is implemented in the open source code MeshLab). The algorithm basically starts from sampling vertexes edges and faces in CAD mesh and searches for the closest counterpart in the scanned mesh and calculated the distance between two sets. Fig. 3-7 shows a contour plot of the Hausdorff Distance between the microstructures of Fig. 3-6. The maximum and mean values were found to be 0.95 mm and 0.11 mm, and when normalized by the diagonal of the bounding foam volume, these metrics give deviations of 3.1% and 0.36% correspondingly. These results indicate that our synthesis protocol is quite accurate in reproducing the desired

geometries.

However, the connection between these global geometric deviations and their effect on the macroscopic material behavior is not straight- forward and more local microstructural features need to be examined. Here we focus on two key morphological descriptors for foams that are known to govern their mechanical properties: (a) their volume fraction (or relative density) and (b) ligament orientation. As aforementioned, SLA can cause volume shrinkage and curl distortion, both of which might not be accurately captured by the Hausdorff Distance. Fig. 3-8 shows an overlap between the design and the (scanned) synthesized foam models, as well as side and top views from an extracted ligament. It is obvious that the curing and photo- polymerization processes led to small but non-negligible volume shrinkage. We found that the difference in volume fractions between target and synthesized materials was in the range of 7-16%. This deviation will later be accounted for in the analysis of our crushing experiments.

In order to measure manufacturing-induced distortions, we further compare the orientations of foam ligaments. Recall that the simulated froth in the Surface Evolver is constrained by Plateau's laws and therefore four edges meet at the tetrahedral angle 109.47°. Fig. 3-9 shows a close-up view of foam ligaments near a node. The corresponding angles between pairs of ligaments for the design and the synthesized foam show a minimal distortion ($< 2°$) between the two 3D objects, with both being very close to the idealized froth topology. Having established control over microstructural characteristics and the underlying solid material behavior, we perform next a series of compression experiments to examine the foam strength and the resulting failure mechanisms.

3.3 Crushing Strength of Brittle Foam

3.3.1 Effect of Boundary and Load Distribution

In the previous Chapter we mentioned the strong effect of load-transferring conditions on the strength measurements of brittle cellular materials that has also been reported by (Mora and Waas [35], 2002 and Letellier et al. [36], 2017). This effect, however, remains to be systematically quantified. We use here our ability to design and synthesize specimens with different boundaries in order to calculate the effect of load distribution on the foam strength. In particular, two types of monolithic specimens are synthesized: type (A) has two plates attached to the foam on both ends while type (B) has a free end on top. Fig. 3-10 shows designs and 3D-printed foams with 1000 cells for both types of specimens. The existence of supporting plate at the other end, i.e. the bottom side, is necessary for the feasibility of the printing process.

Note here that the addition of supporting plates introduces an additional challenge on achieving a precise relative density for the specimen as well as estimating it. The volume and total mass, including the one of the plate(s), is first measured for each 3D-printed specimen post-curing. After each crushing experiment, we measure the mass of the plate(s) and subtract it from the specimen so we can estimate the relative density of the foam. However, the plate can often be slightly damaged during the experiment and/or the extraction of the foam which can lead to some error in the density estimate. This process, along with the reported volume shrinkage caused during printing, makes it difficult to predict the relative density a priori, during the design phase. One has to account for the volume shrinkage of the whole specimen caused by the SLA process together with the curling and shrinking of the plate(s). Therefore, there will always be slight deviations in the final relative densities compared to the nominal values (i.e. of the design) as well as small measurement errors in their reported values.

All compressive experiments are carried out at a constant strain rate $\dot{\varepsilon}$= 0.005/min using an MTS Criterion Series 40 testing stage. The dimensions of all specimens are 48 × 48 × 48 mm. A typical compressive response of a type A specimen, bounded by plates on top and bottom, can be seen in Fig. 3-11 (a) which depicts the nominal stress (force/undeformed area) vs. macroscopic strain (shortening/original height) curve. Initially all ligaments are under compressive and bending loads and the base material behavior is elastic. The macroscopic foam response is almost perfectly-linear elastic up to a stress value of approximately 0.9 MPa and a macroscopic strain = 4.75%. At that load, the local stress at some ligament(s) reaches the critical fracture strength of the base photopolymer. The foam then suffers brittle failure with damage initiating at the area within the specimen where the first ligament(s) break. Failure propagates instantaneously through the specimen by cracking neighboring undeformed cells (see Fig. 3-11 (b)). The macroscopic stress at this point drops to zero and all strain energy is released.

On the other hand, experiments on type B specimens, having a free end, produce a very different type of response and associated deformations as is shown in Figs. 3-12 (a) and 3-12 (b). As was shown before, the response is initially linear elastic but with a slightly reduced stiffness (see dashed line corresponding to the response from the type A experiment). The elastic regime in this case ends at a somewhat lower macroscopic strain ε= 3.4%. More importantly, this critical strain is associated with a significantly decreased crushing strength σ_{cr} = 0.58 MPa. It is obvious that the presence of a support plate and the uniform load-distribution that it provides cause a strength increase, similar to our previous observations from the experiments on the carbon foams. On the other hand, in type B experiments, crushing initiates and propagates at the free boundary, breaking ligaments and foam cells in a row-by-row manner. This can be clearly seen in Fig. 3-12 (b) which shows the foam crushed on top but the rest of specimen being essentially intact. The initial breaking of ligaments

causes a sudden drop of the stress and the response then traces a jagged plateau. The undulations in the plateau correspond to the crushing of each row of cells therefore one can expect a slightly smoother response as the number of foam cells increases. In fact, we've seen this in the corresponding response of carbon foams where all specimens had a minimum of 50 cells per edge, compared to the 10 cells in the 3D-printed foams. In the end of the plateau, the additional compaction of remaining intact cells leads to the densification regime, common among all foams under compression. Next, we will examine the consistency of the trends reported here, analyze their connection to the foam microstructure, and measure the true foam strength as a function of its relative density.

3.3.2 Effect of Microstructure Randomness

The results presented so far, on the compressive response of brittle 3D-printed foams, are consistent with our previously reported experiments on commercial reticulated carbon foams. The ability, however, to accurately reproduce identical but still random microstructures, combined with the increased control over the underlying solid behavior allows for a systematic study of these trends and directly relating them to specific microstructural characteristics. We first investigate how manufacturing-induced deviations, which we measured and analyzed using microcomputed tomography, combined with the variability of the fracture strength of the underlying printed photopolymer affect the macroscopic foam response.

Fig. 3-13 shows two sets of compressive responses from foam specimens that share nearly equal relative densities $\overline{\rho}_{avg} = 11.5\% \pm 0.3\%$. One can see that the deviation between the responses is minimal, independently of the loading conditions and the existence of the supporting plate, further reinforcing our synthesis protocol's robustness. The ability to synthesize an identical random microstructure repeatedly is crucial for minimization of scatter in experimental measurements and the ability to

accurately identify trends in the responses. In order for these results to be general enough however, they should not depend on the particular random microstructure chosen or the number of foam cells used. We have already seen that in commercial foams, where heterogeneities (in the form of broken ligaments, closed cells, density gradients, etc.) are present, one needs a large enough specimen size since smaller specimens (that have fewer cells) are more prone to those defects. In our additively manufactured foams, however, the responses are independent of specimen size and convergence needs to be checked only for the number of foam cells, which in this case is predefined by the target design.

Fig. 3-14 shows two sets of compressive responses, one corresponding to specimens with free ends and the other to the ones having the attached plates. The results indicate that the randomness of the microstructure and the number of cells have a little effect on the macroscopic foam response. Even though the foam with the larger cell-number appears to have a slightly larger strength in type A crushing and a smaller one for type B, this was not consistent across different experiments and is attributed to typical variations in relative density and base material strength. Furthermore, as expected, the plateau of the foam with the 3375 cells is smoother, since the number of cell-rows that are crushed increased by 20%. Note here that we don't expect the response to be in general independent of the number of cells. On the contrary, a foam specimen with a significantly larger number of cells, but the same relative density, would have ligaments with a much smaller cross-section and thus increased fracture strength.

3.3.3 Effect of Relative Density

We next synthesize foams with the same random microstructure but different relative densities by scaling the cross-sectional area of their ligaments (see Fig. 3-15). The responses of these foams are shown in Figs. 3-16 (a) and 3-16 (b) for specimens of

type A and B respectively, and one can easily notice the significant increase of the material strength with density. The responses are consistent with the results reported in the previous sections, showing an abrupt brittle failure for type A specimens and a fuzzy stress plateau to densification for type B. It is important to notice that at high relative densities, i.e. for $\overline{\rho} \approx 17\%$, the elastic part of the response is not perfectly linear. This is attributed to the ligaments' cross-sectional area, which is now larger, making the ligaments more bulky and thus stiffer.

Several experiments were performed to specimens with a range of relative densities in order to quantify the effect of density on the foam strength for both type of loading conditions. In particular, we synthesized three groups of foams with nominal densities $\overline{\rho} \approx 5\%, 10\%$, and 15%(see Fig. 3-15). Note that typical values of relative densities for commercial open-cell brittle foams vary between 2% and 20% so the range studied here is quite representative. We report all experimental details and measurements in Table 3-I.

We first measure the increase in strength caused by the load- transferring conditions offered by the supporting plate, and how this difference is affected by the relative density. Fig. 3-17 shows the ratio of foam crushing strength for specimens of type A to the ones of type B as a function of density. The graph shows clearly that this ratio is not constant but is strongly dependent on density. At low-density foams the increase due to the supporting plate is more than 200%, but as the density increases the ratio reaches a value of ~ 1.5. This is related to the strength of the ligaments at the free boundary. For densities $\overline{\rho} \approx 5\%$ those ligaments are slender and easier to break at a low stress, but as the volume fraction increases the fragments involve a higher number of ligaments and/or complete foam cells, giving rise to an increase in strength that approaches the true one obtained in type A specimens.

We report the crushing strength σ_{cr} normalized by the mean underlying solid fracture strength σ_{fs} as a function of density in Fig. 3-18. An optimal power-law fit

gives

$$\frac{\sigma_{cr}}{\sigma_{fs}} = 0.57\overline{\rho}^{1.68} \tag{3.2}$$

with $R^2 = 0.991$ and is also included in the figure with a solid line. Comparing it to the Gibson-Ashby formula (Gibson and Ashby [4], 1999) (see Fig. 2-1) we find a coefficient that is 3 times larger than theirs and the power exponent is also slightly higher. This can be attributed to the fact that at low relative densities, instabilities will be initiated before the stress in the ligaments reaches the value σ_{fs} . Considering that in elastic foams, where there is no material failure in the form of yielding or fracture, the plateau stress scales with density by a power of n = 2, then one expects that the effect of instabilities will cause the power-law exponent in the brittle foams to be larger than 1.5.

Table 3-I. Specimen data and experimental measurements.

Boundary A (constrained) B (free end)	Specimen Edge length, L*W*H (mm)	Relative Density (%)	Crushing Strength psi (MPa)	Plateau Strength (Avg.) psi (MPa)
Type A	NA	4.75	32.71 (0.226)	NA
Type A	NA	4.75	32.53 (0.224)	NA
Type A	47.78*47.47*42.82	4.10	20.15 (0.139)	NA
Type A	47.14*47.46*42.06	4.38	25.73 (0.177)	NA
Type A	45.58*45.49*42.39	4.69	29.28 (0.202)	NA
Type A	45.36*45.25*43.00	4.45	23.26 (0.166)	NA
Type A	45.46*45.47*43.72	4.32	24.14 (0.166)	NA
Type A	45.51*45.44*42.21	11.83	146.54 (1.01)	NA
Type A	45.33*45.25*42.39	11.23	132.51 (0.914)	NA
Type A	45.43*45.51*43.02	11.27	158.01 (1.089)	NA
Type A	45.24*45.31*43.54	17.3	243.49 (1.679)	NA
Type A	45.34*45.15*43.77	17.06	231.07 (1.593)	NA
Type A	45.49*45.38*43.78	16.6	248.37 (1.712)	NA
Type B	NA	4.75	10.05 (0.069)	3.93 (0.027)
Type B	NA	4.75	9.63 (0.066)	5.38 (0.037)
Type B	47.15*47.07*44.25	3.61	8.56 (0.059)	5.4 (0.037)
Type B	47.14*47.00*44.66	3.25	5.74 (0.04)	5.01 (0.035)
Type B	45.38*45.15*44.24	11.54	84.44 (0.582)	41.27 (0.285)
Type B	45.33*44.87*44.57	11.11	92.95 (0.641)	38.91 (0.268)
Type B	45.24*45.36*44.83	11.52	66.02 (0.455)	30.12 (0.208)
Type B	45.19*45.35*44.35	16.07	145.33 (1.002)	68.88 (0.475)
Type B	45.69*45.53*44.91	17.36	161.84 (1.116)	91.9 (0.634)
Type B	45.27*45.17*45.42	16.66	144.92 (0.999)	62.04 (0.428)

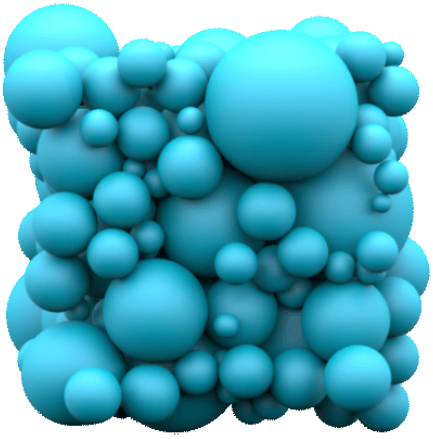

(a)

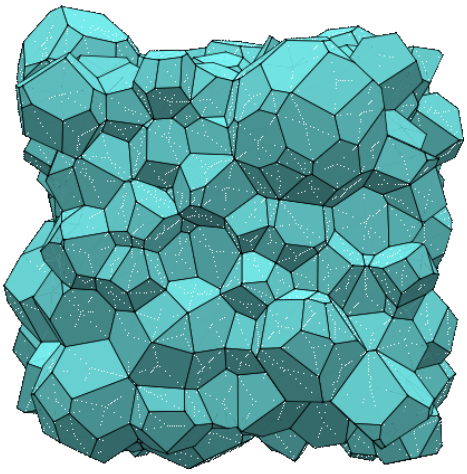

(b)

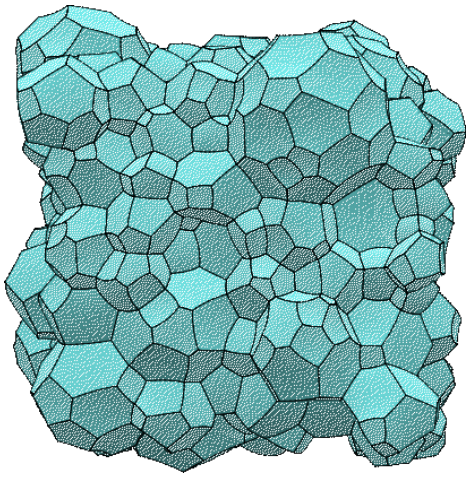

(c)

Figure 3-1. Generating random foam topologies: (a) sphere packing, (b) Laguerre tessellation, (c) random froth structure.

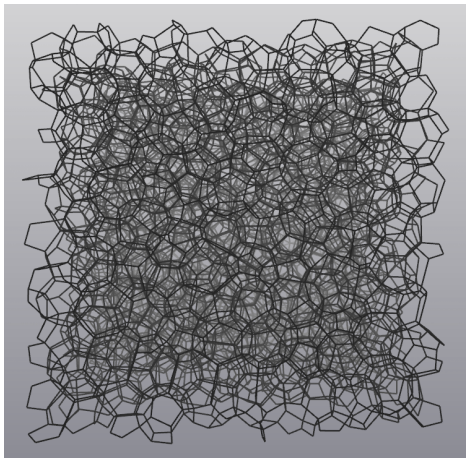

(a)

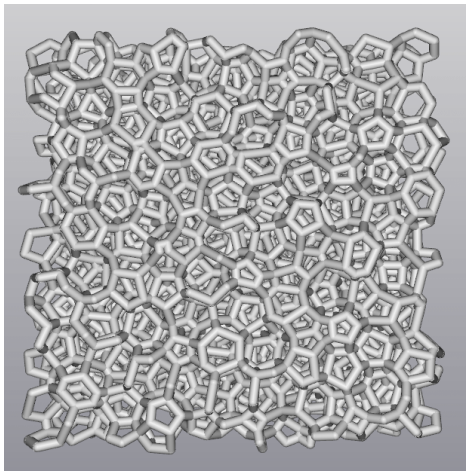

(b)

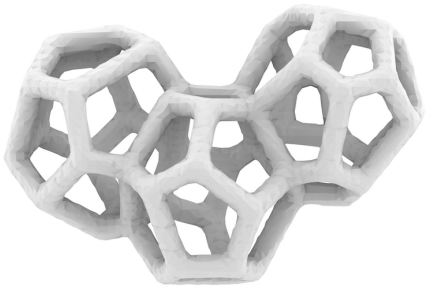

(c)

Figure 3-2. Design of open-cell foams with controlled morphological features: (a) foam topology, (b) 3D-model with prescribed relative density, (c) cluster of foam cells.

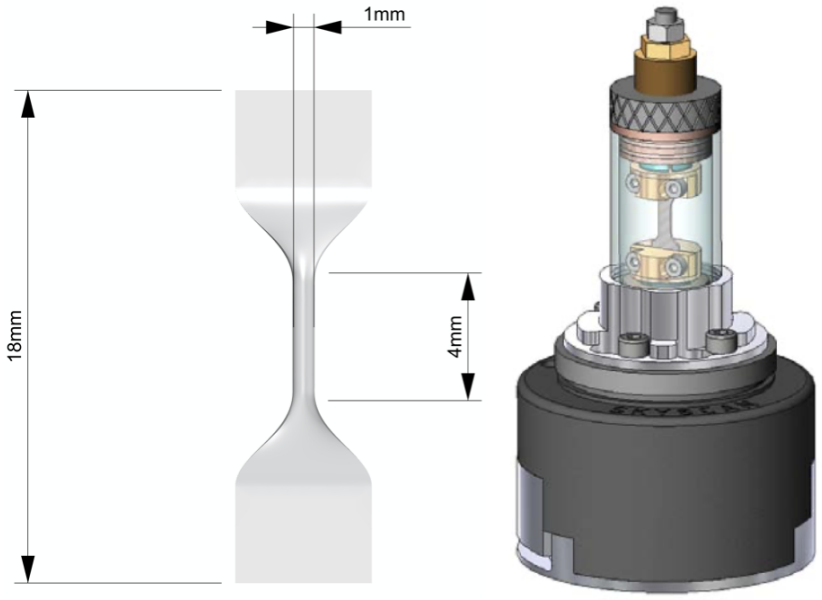

(a) (b)

Figure 3-3. Schematics of (a) dog-bone specimen for base-material testing and (b) in-situ tensile test apparatus [79].

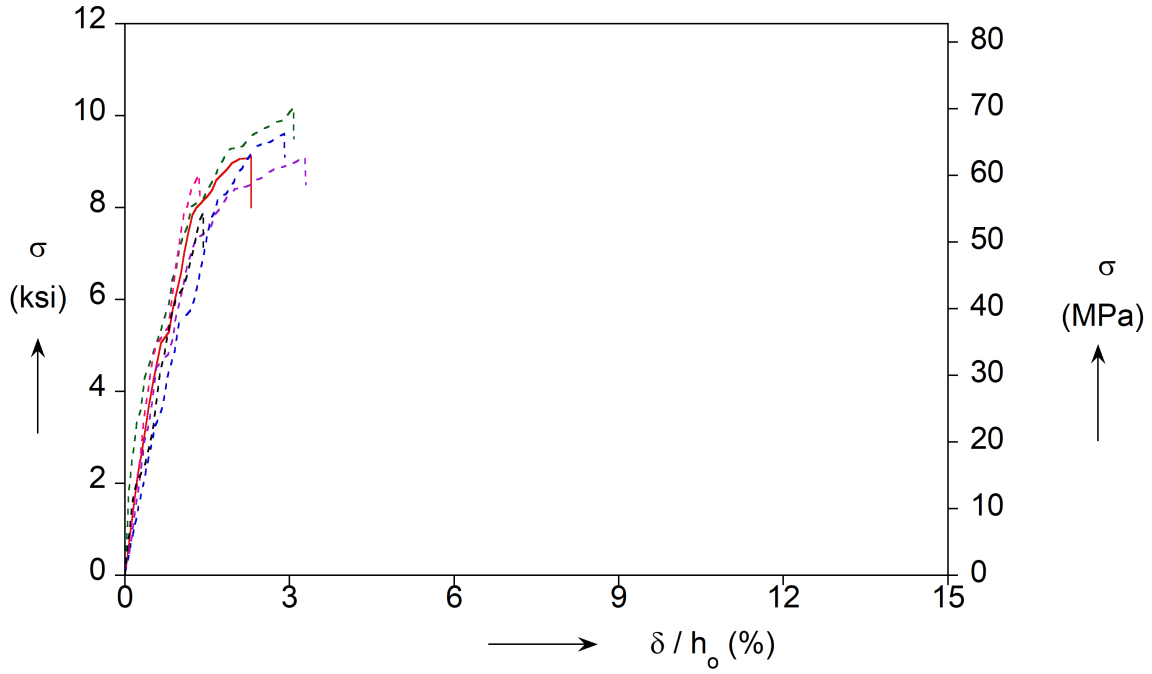

Figure 3-4. Typical tensile responses of 3D-printed dog-bone specimens.

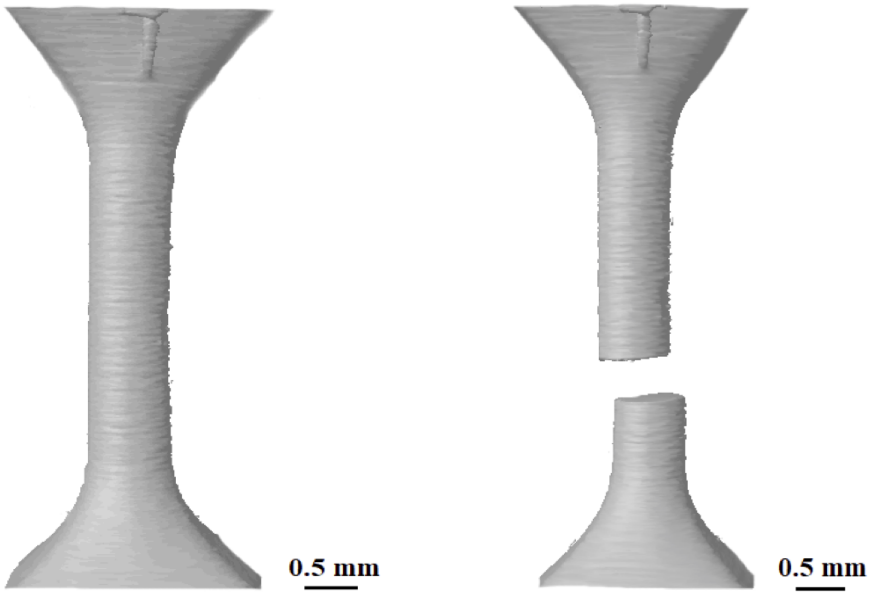

(a) (b)

Figure 3-5. Tomography images showing brittle failure of 3D-printed dog-bone specimen.

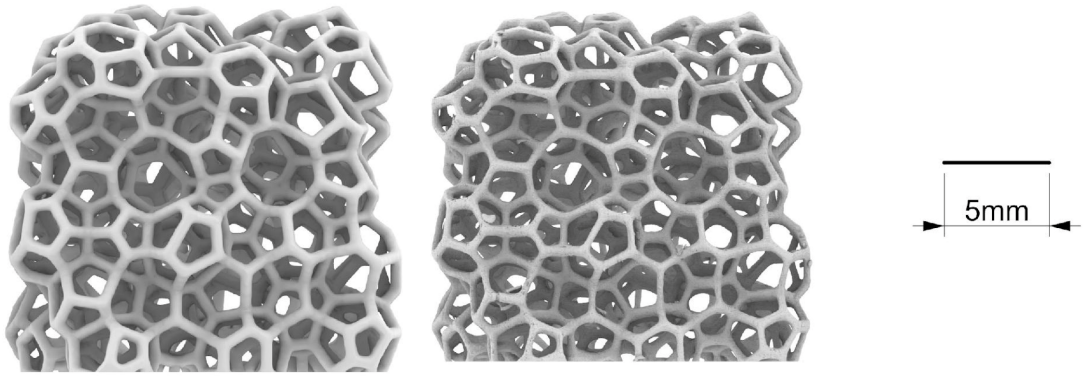

(a) (b)

Figure 3-6. (a) Design of foam with 64 cells and (b) Scanned reconstruction of the 3D-printed foam.

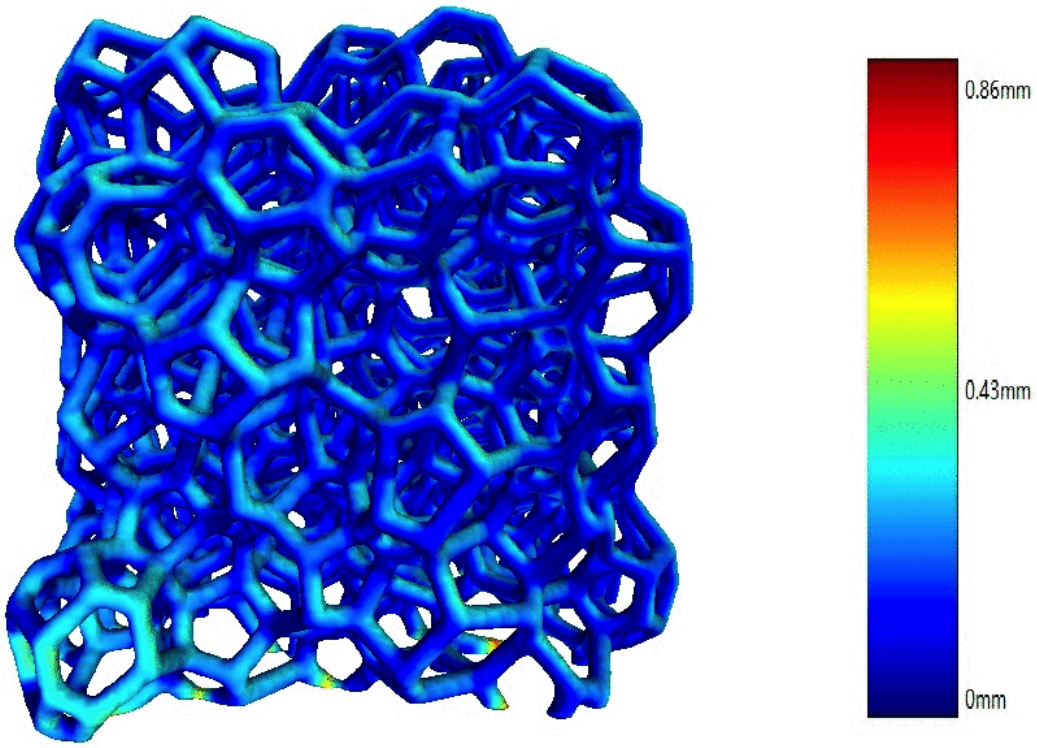

Figure 3-7. Contour plot of Hausdorff Distance between design and synthesized foam.

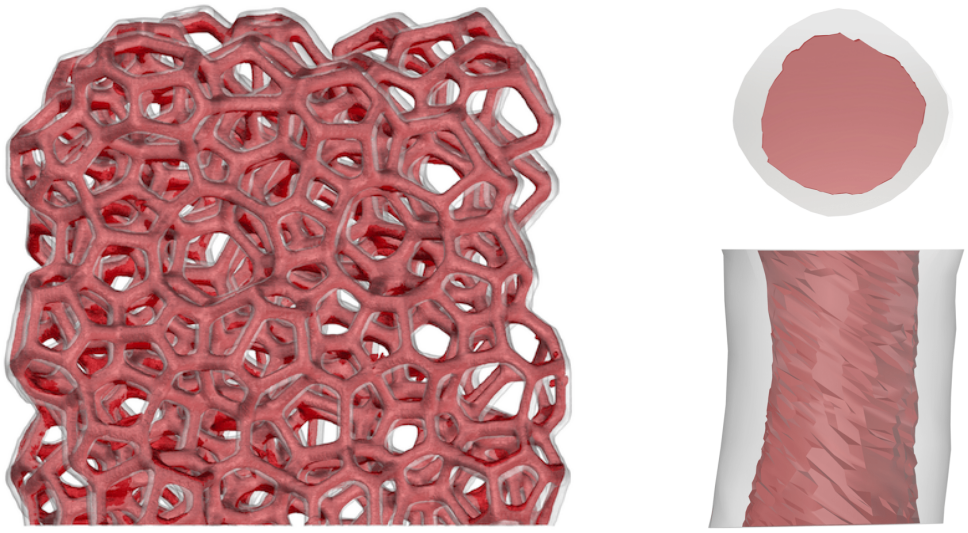

(a) (b)

Figure 3-8. Relative density comparison by microcomputed tomography (a) overlap of foam design (transparent) and synthesized (red) foam (b) ligament cross- section shrinkage.

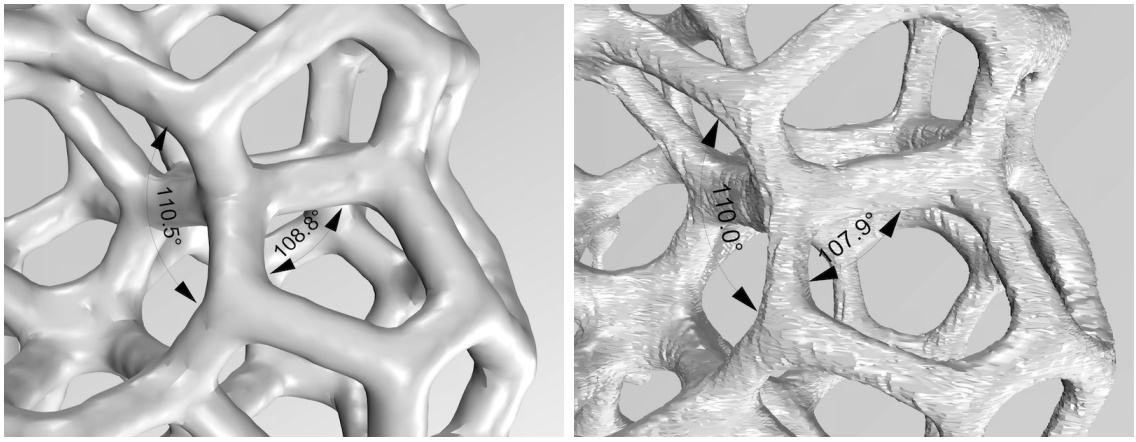

(a) (b)

Figure 3-9. Ligament orientations in (a) foam design and (b) synthesized foam.

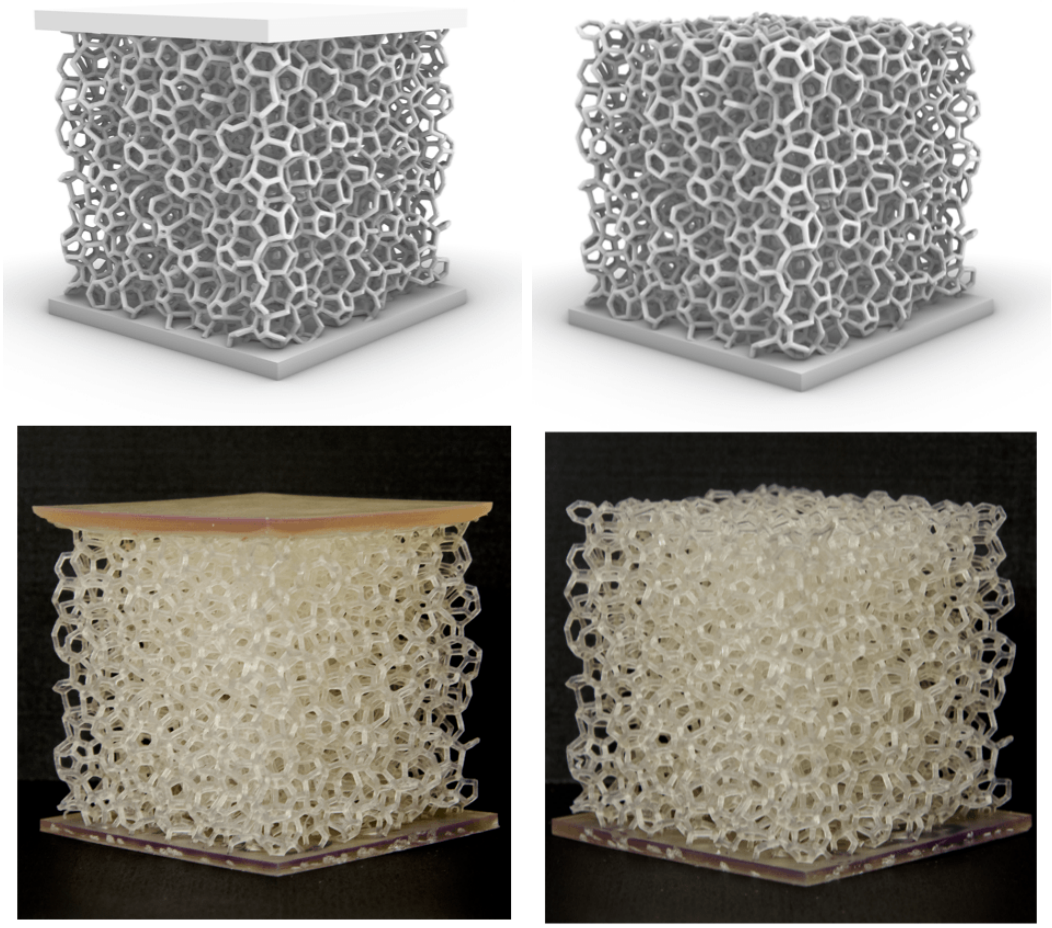

(a) (b)

Figure 3-10. Foam designs (top) with 1000 cells and 3D printed specimens (bottom) having (a) plates attached on both ends and (b) one free end.

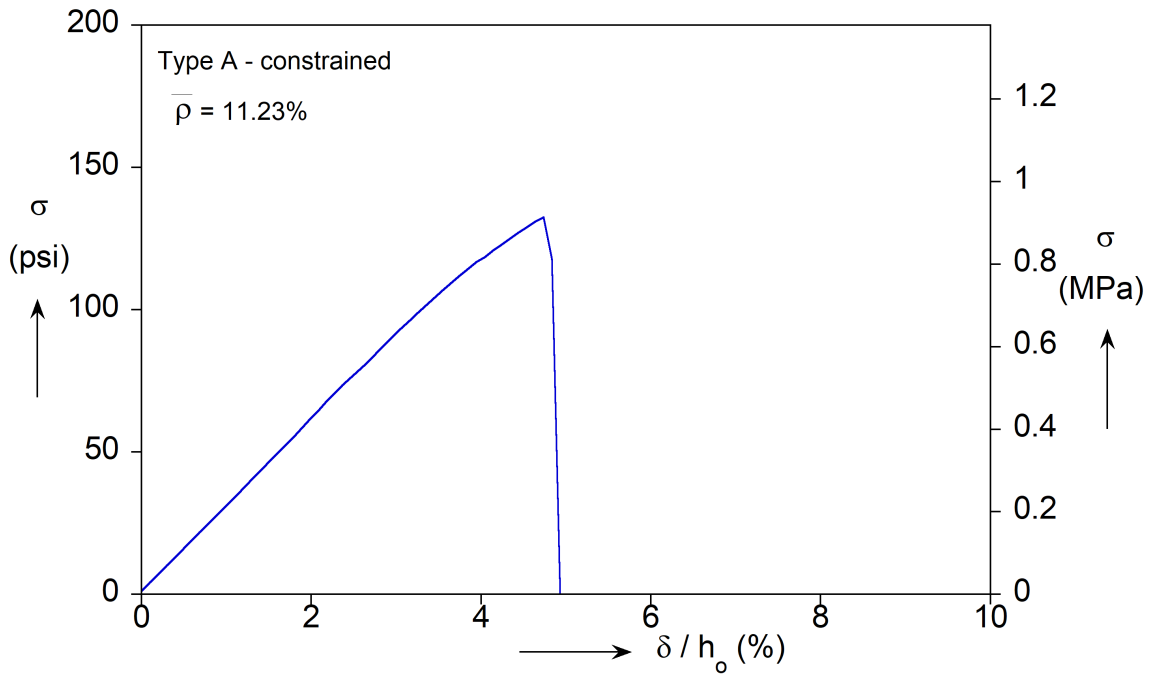

(a)

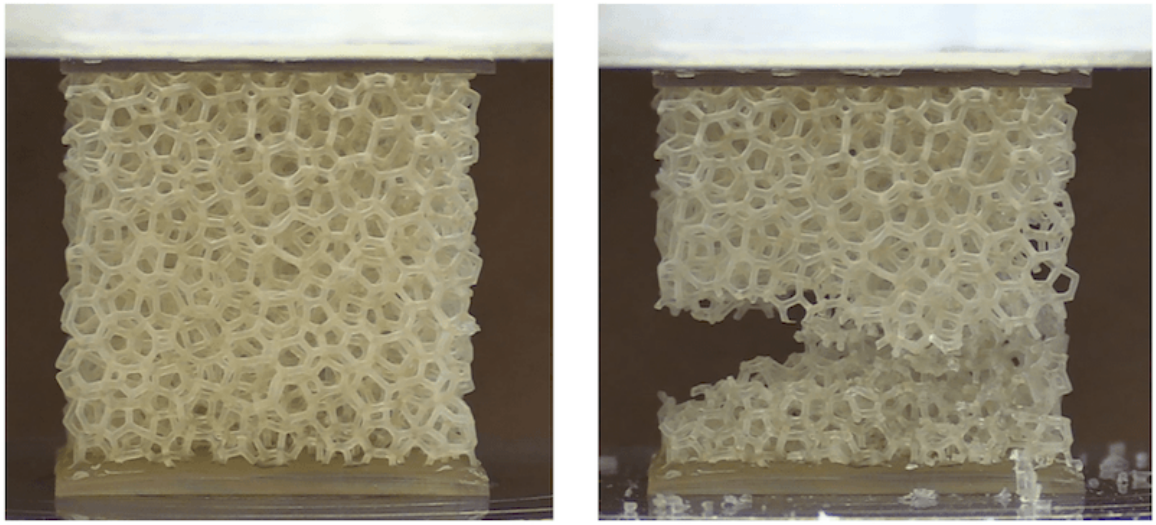

(b)

Figure 3-11. (a) Compressive response of Type A foam specimen (b) Undeformed foam (left) and brittle failure (right).

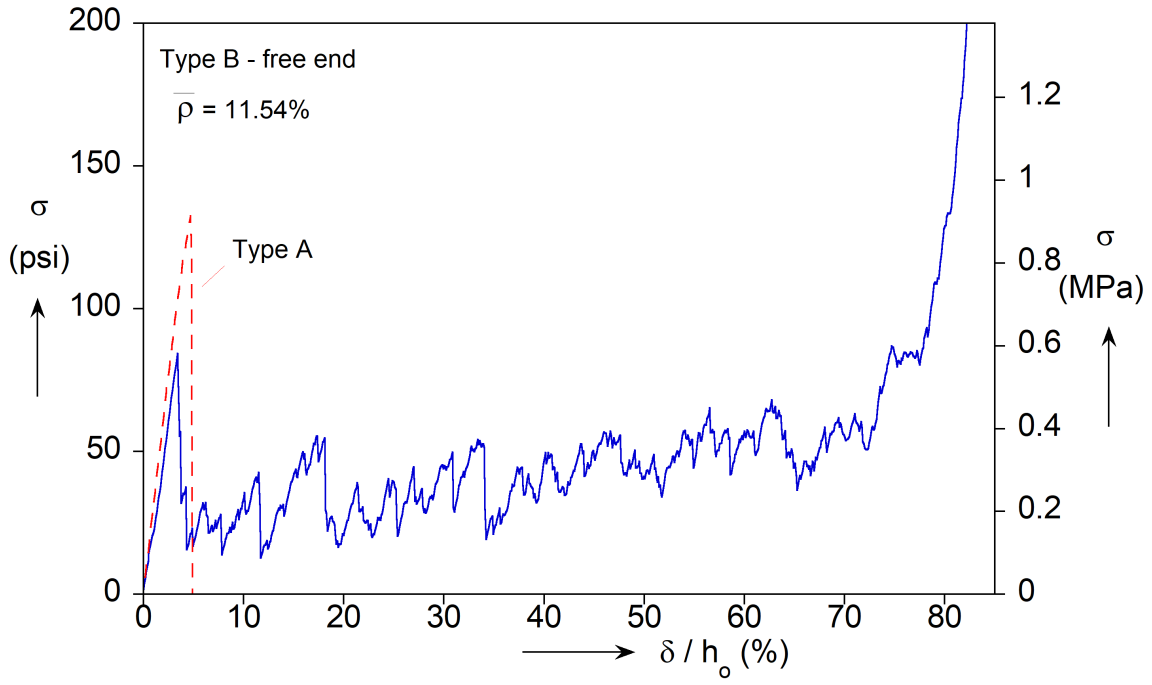

(a)

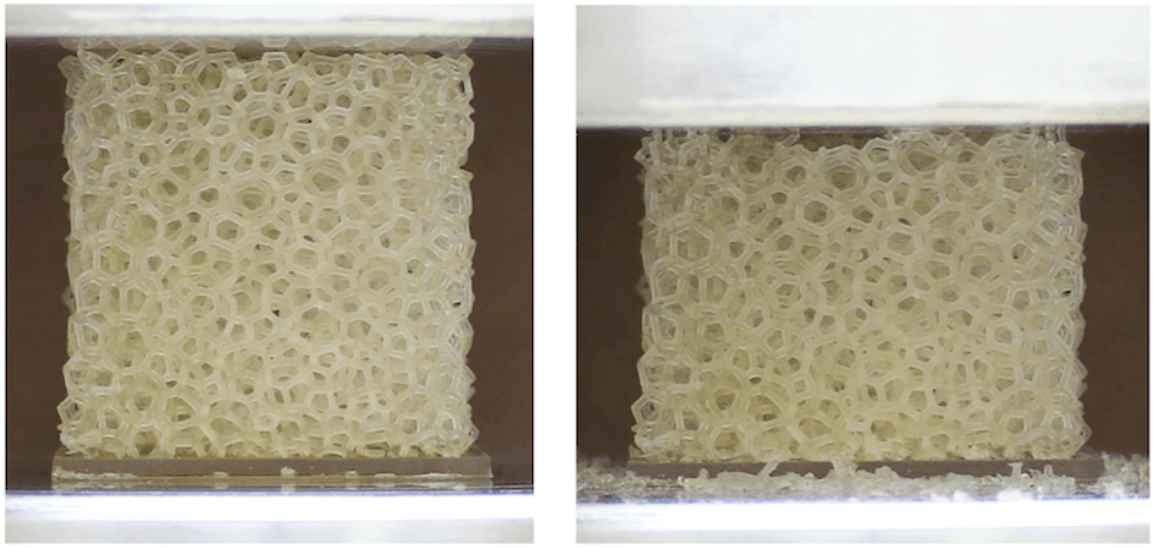

(b)

Figure 3-12. (a) Compressive response of Type B foam specimen (b) Undeformed foam (left) and crushing at the free end (right).

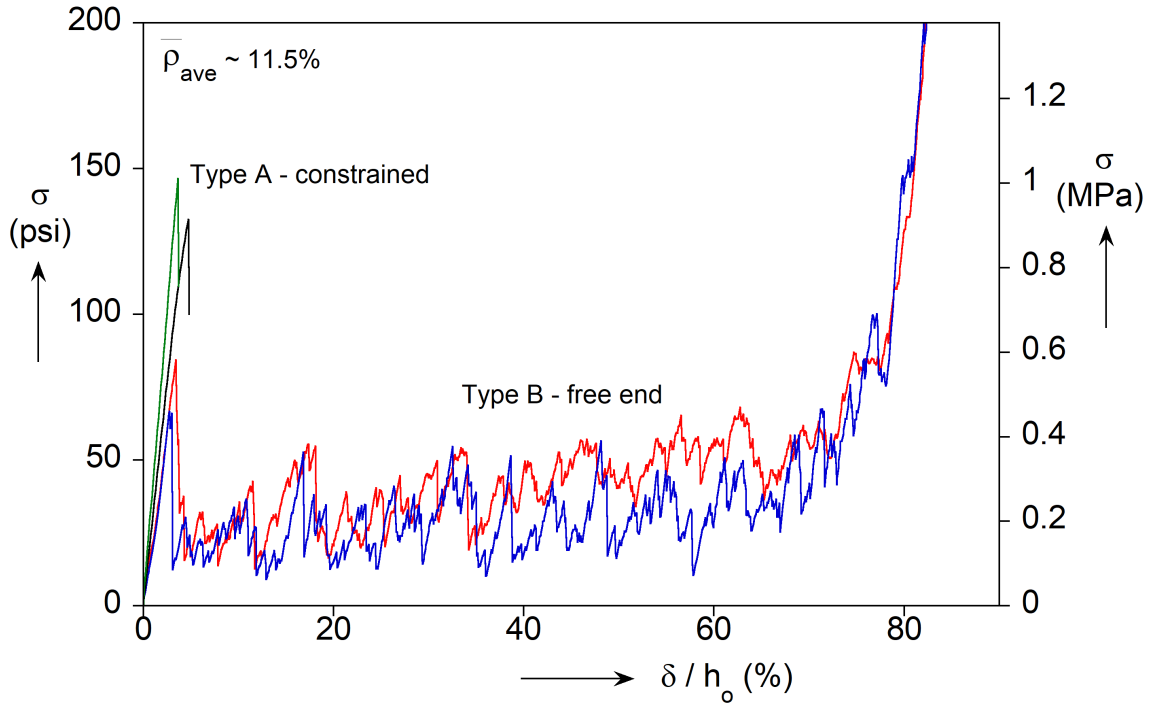

Figure 3-13. Comparison of crushing responses of foams with identical random microstructures and the same relative density for both Type A and Type B foam specimens.

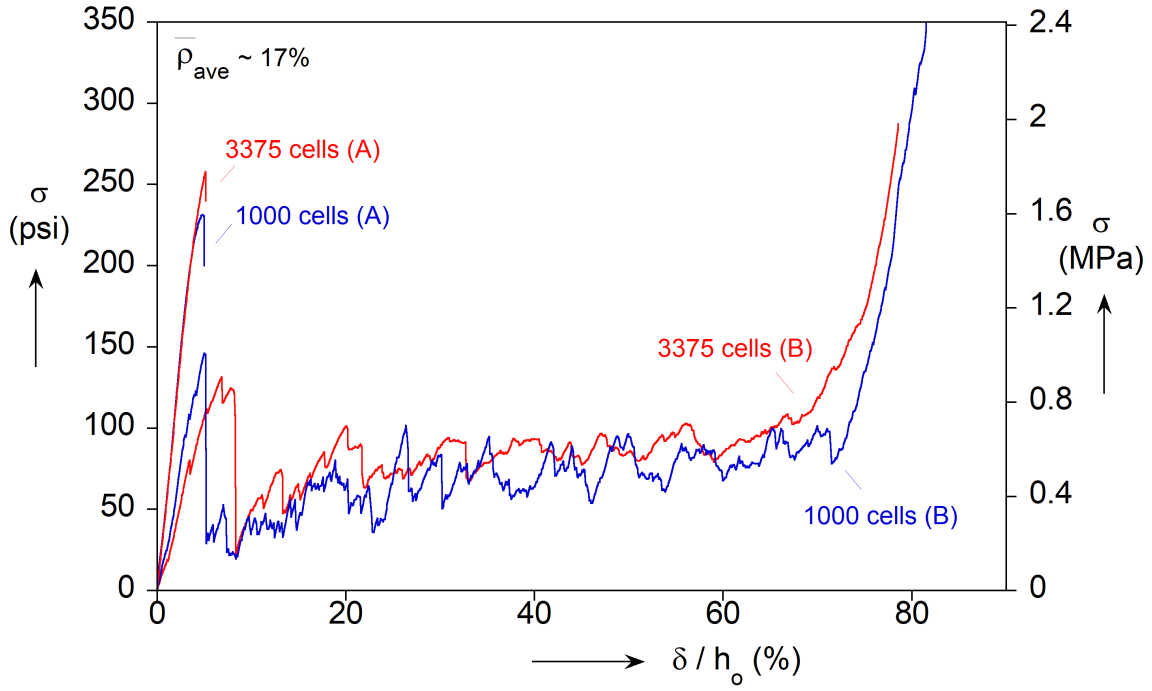

Figure 3-14. Comparison of crushing responses of foams with different microstructures and number of cells for both Type A and Type B foam specimens.

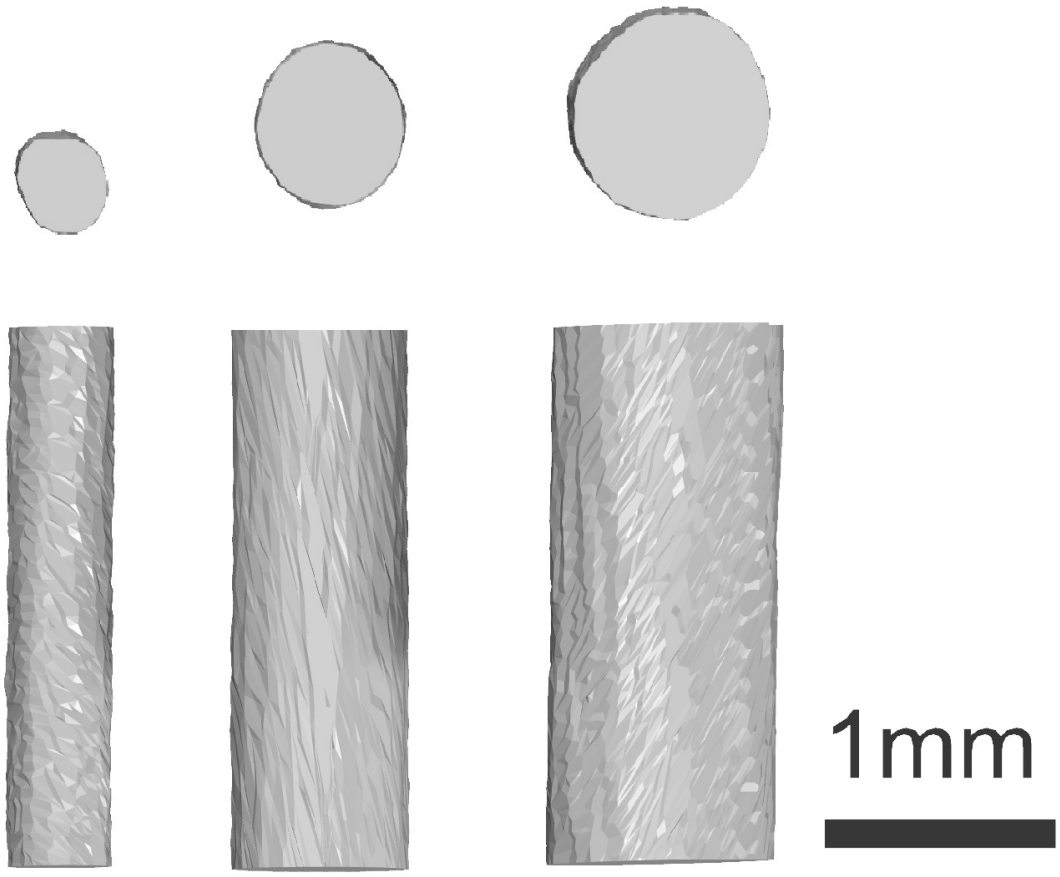

Figure 3-15. Ligaments and their cross-sections corresponding to (from left to right) foam relative densities of 5%, 10%, and 15%.

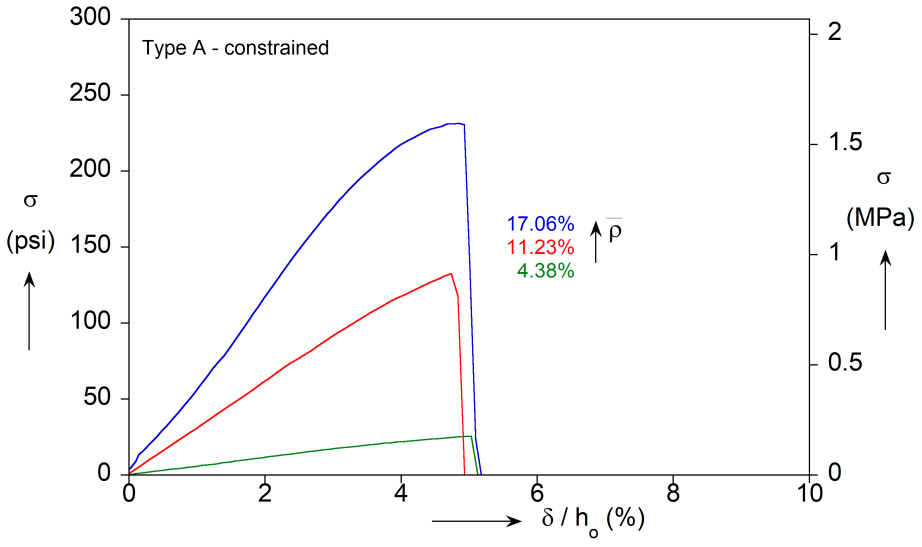

(a)

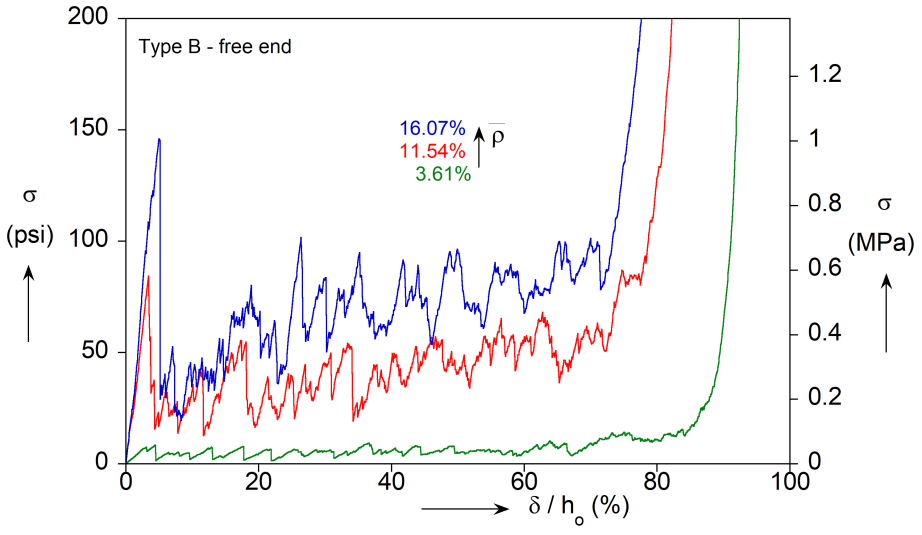

(b)

Figure 3-16. Compressive response for foams with the same random microstructure but different relative densities (a) Type A specimens (b) Type B foam specimens.

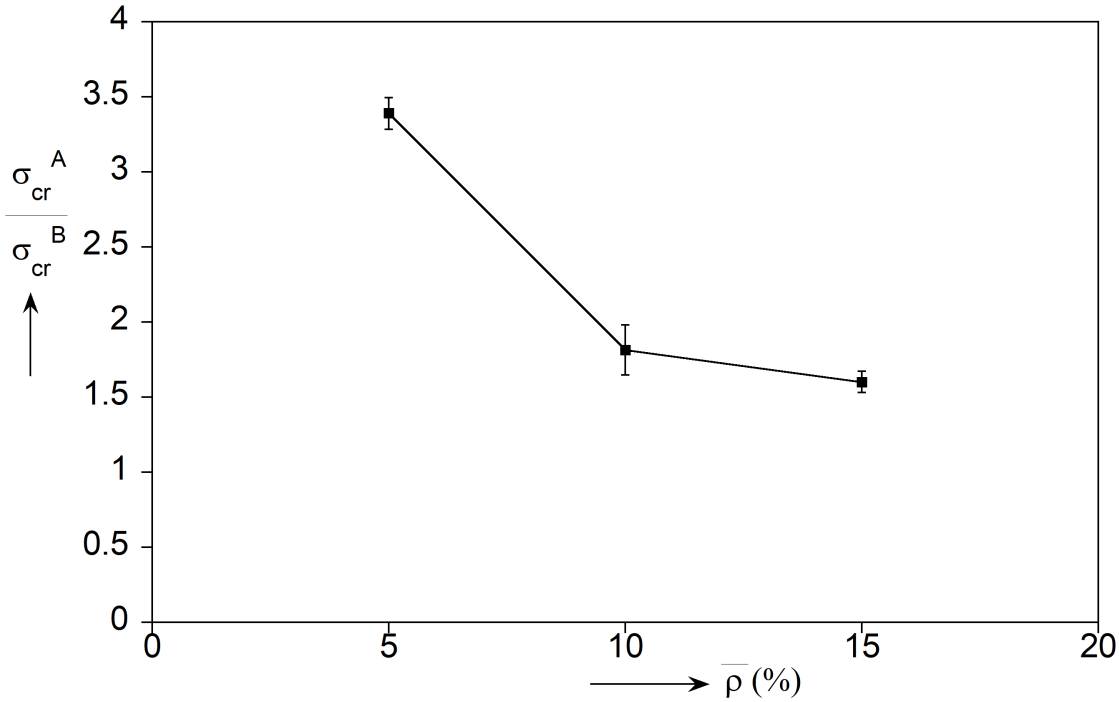

Figure 3-17. Strength ratio of Type A to Type B foam specimens against relative density.

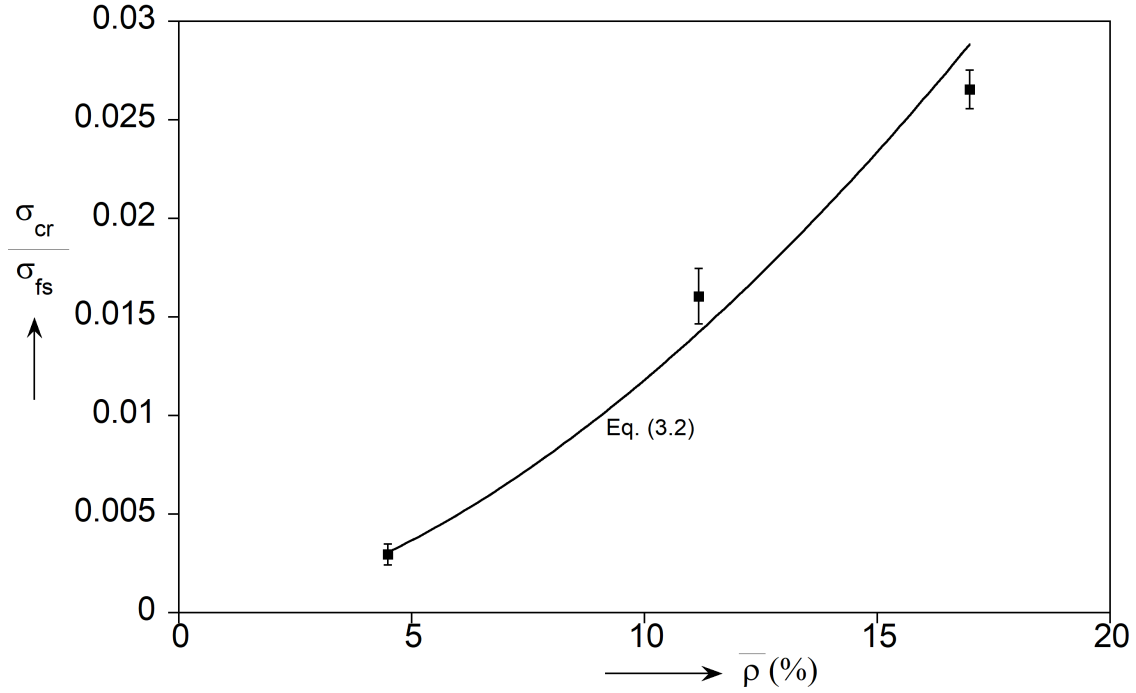

Figure 3-18. Crushing strength of brittle foams normalized by the fracture strength of the base photopolymer against relative density.

Chapter 4

Crushing of Metal Foams at High-Temperatures

The mechanics of cellular materials under extreme temperatures has been largely understudied, especially in the case of open-cell foams, in comparison to their mechanical behavior at room temperature. Cady et al. [80] (2009) examined the effect of cryogenic temperatures on the crushing strength of closed-cell foams and measured the strength enhancement as temperature decreases. Wang et al. [81] (2014) investigated the mechanical properties of closed-cell foams under elevated temperatures and found an increased rate-sensitivity with high temperatures, while Movahedi et al. [82] (2018) found a linear degradation of the stress plateau and the energy absorption capacity as temperature increases. Linul et al. [83] (2018) studied the combined effect of anisotropy and temperature on the compressive response of closed-cell foams and observed that elevated temperatures have a higher effect when closed-cell foams are compressed in the axial (rise) direction. They also reported a linear relation between energy absorption and temperature. Similar trends were found by several works that focused on syntactic foams, which attain their porosity by filler particles, and their compressive response at high temperatures (Mondal et al. [84], 2012; Taherishargh et al. [85], 2018; Linul et al. [86], 2019).

The present work aims to use crushing experiments on metal foams within an

environmental chamber to quantify the effect of elevated temperatures on the compressive response and the associated limit stress, densification strain and total energy absorption [87]. Furthermore, DIC and imaging data analysis are used to examine how high temperatures alter the initiation and evolution of crushing within the material.

4.1 Metal Foams Microstructure

The foam examined in this study (Fig. 4-1) is a Duocel® aluminum (Al 6101-T6) foam by ERG Materials and Aerospace Corp. The manufacturing process involves casting metal on a polymeric foam template (Ashby et al. [3], 2000). The template foam is coated with ceramic powder, baked in order to dissolve the polymer and subsequently filled with the aluminum alloy. The resulting open- cell foam has a cell-size that can range from 5 pores per inch (ppi) to 40 ppi and a relative density between 3 and 12%. A detailed study on the microstructure of the Duocel® aluminum foam and its connection to the resulting mechanical properties has been performed by Jang et al. [55] (2008) so we choose here to merely summarize the main characteristics. The underlying foam topology consists of irregular polyhedra with a varying number of faces. The ligaments are nearly straight beams with a non-uniform cross-section. During the foaming process and metal solidification, the shape of this cross-section changes from a three-cusp hypocycloid (Plateau border) in the polymeric foam to a rounded triangle for the metal one (see Figs. 3 and 11 in Jang et al. [55], 2008). In monodisperse foams, such as the one considered here, all cells have nearly the same volume. This is dictated by the original polymeric foam replica that is used for the casting. The foaming process can furthermore produce, typically inadvertently, other morphological characteristics such as anisotropy, i.e. an elongation of cells in the foaming direction, as well as the existence of a small number of remaining closed-cells in the final foam, as one can notice in Fig. 4-2(a). In the foam specimens considered here, the anisotropy parameter $\lambda = h/w$ (see Fig. 4-2 (b)) has an approximate value

of 1.2. The foam specimens analyzed have cell-sizes of 10ppi and 40ppi and this effect on the response will also examined.

4.2 Compressive Response at Room Temperature

The compressive response of open-cell metal foams at room temperature has been examined by several researchers and is now properly understood. Jang and Kyriakides [88] (2009a) combined experiments with microcomputed tomography to examine in detail the foam crushing response and the associated deformation patterns. Here, for the sake of completeness, and more importantly to allow direct comparisons with the results for crushing at elevated temperatures presented next, we first perform quasi-static experiments at room temperature. A typical compressive response of a 40 ppi cubical specimen with an edge of 50 mm can be seen in Fig. 4-3 which depicts the nominal stress (force/undeformed area) vs. macroscopic strain (shortening/original height) curve. The response is initially linear elastic, with an effective modulus E = 262 MPa. As the load increases, however, the response becomes gradually nonlinear and at a macroscopic strain of about 2% reaches a limit load $\sigma_I = 2.16MPa$, which is known as the initiation stress. The stress peak is followed by a small drop and the response then traces a long plateau under an average plateau stress $\sigma_P = 2.22MPa$,. The plateau terminates at a macroscopic densification strain $\varepsilon_D = 0.52$, at which point the response picks up and a second stiffening part initiates. The plateau stress here σ_P is defined as the average stress from the lowest point of the response right after the initiation peak, to a value 1.2 times higher on the second ascending part at the initiation of densification. The densification strain ε_D is the macroscopic strain corresponding to the plateau stress. Note that the gradual stress increase observed along the plateau, starting at a macroscopic strain of about 15% and continuing until the abrupt rise during densification, is attributed to strengthening from the foam ends that are bonded to thin plates and variations of the density caused by remaining

closed-faces (see similar effect in Fig. 1a of Jang and Kyriakides [88], 2009a). These features however, would be negligible in a much larger specimen size.

Imaging during crushing reveals the deformation characteristics associated with this response. Fig. 4-4 (a) shows images of the compressed foam at the points marked on the response of Figs. 4-3 and 4-4 (b) presents the results of DIC analysis on the same images. In image ⓪ the foam is undeformed but at image ①, and a macroscopic strain of about 6%, the material has localized and a band of collapsed cells has formed in the lower half the specimen, tracing its entire width. The band angle and the joining with the bottom of the specimen, where foam cells are strengthened by the attached plates, results in the continuously positive slope of the stress response past the limit stress. In image ②-⑥, crushing continues through the widening of the band by the collapse of neighboring cells, while the average strain goes from 13% to 40%. The specimen has two very distinct zones: one of cells that have collapsed and one with cells that are essentially intact. With increased compression the bands broadens as neighboring cells are crushed. At image ⑦ nearly all cells have collapsed except from a few located near the boundary, that as we mentioned have additional stiffness. Now that there are no more cells to collapse, the response increases abruptly and the deformation becomes homogeneous again. The crushed cells are subsequently further compacted and the stress rises to more than 3 times the value of the plateau. It is important to note that the above observations are based on images of the front view of the foam specimen and not its interior. However, all of the aforementioned remarks agree completely with the corresponding ones of Jang and Kyriakides [88] (2009a) that also examined the foam deformation at its interior using x-ray tomography. Of course, images from a cross-section of the crushed foam, or even a different boundary side, would be slightly different. Both Jang and Kyriakides [88] (2009a) and Gaitanaros et al. [17] (2012) have shown that the bands of crushed cells are not planar but rather trace a complex path following "weak" cells across the domain.

4.3 Crushing at High Temperatures

4.3.1 Experimental Set-Up

Aluminum (Al 6101-T6) foam specimens of two different sizes (50 × 50 × 50mm and 30 × 30 × 30mm) were tested in uniaxial compression inside an MTS 651.06E-03 environmental chamber with a maximum operating temperature of 315 °C. The environmental chamber has a viewing window in the front door, which enables the use of a DIC system which is located outside the chamber. The temperature inside the furnace was controlled through a 2404 Temperature Controller by Eurotherm. An MTS 810 load frame with an MTS FlexTest SE controller was used for displacement-controlled testing within the chamber, see Fig 4-5. The temperature was increased at a rate of 8 °C/min until the target temperature was reached. The specimen was then allowed to equilibrate for 20 min before the application of the compressive load. The temperature within the environmental chamber was maintained to within 2 °C of the desired test temperature throughout the test. The loading rate for all experiments was $\dot{\delta}/h_0 = 8.33 \times 10^{-5} s^{-1}$ where h_0 is the specimen height.

Images of the test specimen were captured using a high resolution PointGrey Grasshopper®3 camera (2824 × 4240 pixels) with an Edmund Optics HP Series 35mm fixed focal length lens. These images were then analyzed using a MATLAB toolbox for Digital Image Correlation (DIC) available at https://www.mathworks.com/matlabcentral/fileexchange/12413-digital-image-correlation-and-tracking. Digital Image Correlation has been used by Bastawros et al. [89] (2000) to study the deformation mechanisms in closed cell aluminum foams as well as by Lee et al. [90] (2006) for open cell aluminum foams. During the DIC analysis, the program correlates the position of a set of control points in a reference configuration image to a corresponding configuration of the deformed foam specimen and computes the incremental displacements and local (microscopic) strains. In DIC, a speckle pattern

is employed on surfaces without sufficient texture or contrast to allow the algorithm to uniquely identify the location of points being tracked from one image to another. In the case of the open cell aluminum foam, the ligaments of the foam material provide a pattern which is used in lieu of a speckle pattern to track the location of a set of points from one image to the next. The peak-width of the autocorrelation of the intensity values at the pixels of each image provides an estimate of the average feature size in the image. The average feature size for the 40 ppi foam was computed to be 15 pixels. Using a subset of the image of at least 3 times the average feature size is reasonable to obtain accurate measurements (Sutton et al. [91], 2009). The subset size used in the DIC analysis was 51 $\times$ 51 pixels, which is large enough to provide displacement measurements with reasonable accuracy. Local strains were measured by using a gauge length of 50 pixels. The axial component of the nominal engineering strain was computed from these displacement measurements using a central difference method. For temperatures up to 200 °C, a Krylon flat white spray paint was used to reduce the glare from the aluminum. For higher temperatures, a Zynolyte Hi-Temp paint was used which hardened during the heating phase of the test in order to ensure that the paint adhered to the specimen would not peel.

4.3.2 Response at 300 °C

The main characteristics of foam crushing at high temperatures are explored first through a typical test. Fig. 4-6 shows the compressive response of a 40 ppi foam specimen crushed at 300 °C. The response displays the three characteristic regions identified in the room-temperature response (included in Fig. 4-6 with a dashed line): a linear elastic part for low macroscopic strains, an extended stress plateau, and the densification regime. There are however, some key differences between the two responses. First, there is a significant drop at the stress levels. The initiation stress σ_I goes from approximately 2.16 MPa to 0.79 MPa while the decrease of the

plateau stress σ_P is even larger (2.22 MPa at room temperature to 0.52 MPa at 300 °C). Part of this decrease is naturally expected because of the lower yielding stress of the base aluminum alloy at elevated temperatures. Nonetheless, as we will show next, the correlation between the underlying solid material behavior and the macroscopic foam stress is not straightforward. Note here that the decrease of the plateau stress observed in this case is exaggerated, compared to the corresponding one of the limit stress, because of the continuously increasing slope that follows the first peak in the room-temperature response (and was analyzed in Section 4.2). A second important deviation is the prolonged plateau and delayed densification that corresponds to a higher densification strain and is attributed to several factors. First, there is softening of the base aluminum alloy at high temperatures that leads to increased load redistribution and increased compaction at the cell level. The additional local compaction is caused by the decrease of the base alloy's Young's modulus with temperature that softens the contact between ligaments, as well as the reduction of work hardening with increasing temperatures that limits the load that each ligament can carry and therefore increase local bending. Both of these effects, i.e. the more distributed crushing and the increased cell compaction will be analyzed through image analysis and DIC.

Fig. 4-7 (a) and (b) depicts front views of the foam specimen that correspond to the bullet points marked on the response of Fig. 4-6. In image ①, and a macroscopic strain of about 7%, it is easy to observe that instead of localization in one area and the formation of a band of crushed cells, as was the case in room-temperature crushing (see image ① in Fig. 4-4), deformation is now more widespread with several zones of cells collapsing simultaneously. Cell compaction in those areas intensifies in image ②, and at image ③, corresponding to a macroscopic strain of about 22%, we see some of these zones to have merged and transverse the specimen's width. In contrast with image ③ in Fig. 4-4 where strains are strongly concentrated in a single band, deformation here

is more spread out across different regions and one can easily notice the formation of new regions of localization. With additional compression these zones expand and cells in different areas collapse too, as shown in image ④. A comparison with the corresponding image of Fig. 4-4 indicates that at high temperatures, localization in different areas is the governing collapse mechanism, rather than the formation and propagation of a single band. At image ⑦, and a macroscopic strain of 47%, even though most of the foam cells have collapsed, there are still regions with undeformed cells. The crushing of these remaining cells and the base material softening contribute to the plateau extending well beyond this point so the foam can be compacted an additional 15% before the stress reaches the level of the initial limit load. In order to examine in more detail the difference between the collapse mechanisms at room- and high-temperature crushing, Fig. 4-8 shows histograms of the local nominal strains calculated from the DIC analysis at the same level of macroscopic strain (47%). One can easily notice that for the foam specimen crushed at room- temperature, most of the cells have collapsed and the local strain values for the majority of the crushed cells are between 45% and 55%. On the other hand, the strain distribution corresponding to high-temperature crushing has a few distinct characteristics. First, there are remaining foam cells that are essentially undeformed, i.e. with local strains that are less than 10%. Moreover, the strain distribution is wider with a larger number of cells existing with both lower and higher local strains than the ones at room temperature. This reinforces the aforementioned observation that high temperature enables a more widespread collapse mechanism with increased local compaction that is shown here to exceed 80% in some foam cells.

Note that the two main effects on the foam compressive response caused by the temperature increase, i.e. the reduced stress levels and the increased densification strain have opposite effects on the energy absorption capacity of the foam. The way these competing mechanisms affect the strain energy under a range of different

temperatures will be examined in detail in Section 4.4.

4.3.3 Effect of Cell-Size

The key morphological characteristic of open-cell foams is their relative density. Several other features however such as anisotropy, cell-size (ppi), cell-size distributions (monodisperse vs. polydisperse), density gradients, can also affect the response significantly. Jang and Kyriakides [88] (2009a) found a negligible effect of cell-size on the crushing of the same aluminum open-cell foam at room temperature (see their Fig. 15). Here we examine if this observation is still valid when crushing is performed at elevated temperatures. The compressive response under 250 °C of two specimens with equal density but different cell-size, i.e. one with 10 ppi and one with 40 ppi, is shown in Fig. 4-9. It can be seen that the two responses are very similar; however the 10 ppi foam clearly has a noticeably higher initiation stress that is followed by a more abrupt drop past this limit load. The increased initiation stress and more pronounced stress-drop are attributed to the larger cell(s) that collapse at the beginning of localization. Note here that both specimens have the same dimensions. The two plateaus also have a small deviation but less noticeable compared to the limit stresses. In the next section we show that this is indeed the case for all temperatures considered. Therefore it can be concluded that even at high temperatures the relative density remains the governing feature for the microstructure of metallic open-cell foams.

4.4 Foam Strength and Energy Absorption vs. Temperature

A series of crushing experiments under elevated temperatures was performed for the two different pore sizes discussed in the previous section. The effect of temperature on the complete compressive response is seen in Fig. 4-10 (a) and (b) for the 40 ppi and

the 10 ppi foam correspondingly. The results shown follow closely the trends observed in Figs. 4-6 – 4-9. The limit load decreases significantly as crushing is performed under higher temperatures. The same holds for the plateau stress. Furthermore the plateau's slope flattens with increasing temperature and is seen to have a concave up shape for $T \geq 250\,^{\circ}\mathrm{C}$. This indicates that, at high temperatures, there is also a macroscopic softening of the foam that affects the stress plateau and thus in turn the energy absorption capacity of the material. The densification strain is seen to increase from 0.5 to around 0.65 for the highest temperatures considered here. These observations hold for both the 40 ppi and the 10 ppi foam with the latter having somewhat larger initiation and plateau stresses, together with a more pronounced stress drop following the limit load local maximum. Next, we aim to quantify these effects and examine their correlation with the thermomechanical properties of the underlying constituent aluminum alloy.

Fig. 4-11 (a) depicts the initiation stress as a function of temperature for the responses shown in Fig. 4-10 (a) and (b). An optimal fit shows that the decrease with temperature is nearly linear. The equations of the linear fits are $\sigma_I = 2.277 - 0.0043T$ (with $\mathrm{R} = 0.997$) for the 40 ppi foam and $\sigma_I = 2.691 - 0.0049T$ (with $\mathrm{R} = 0.994$) for the 10 ppi foam. This indicates that the decrease rate of limit stress is somewhat higher for larger cells. The decrease is directly related to the corresponding decrease of the base material's (aluminum 6101-T6) yielding stress under high temperatures. To examine if the two stress drops are proportional, in Fig. 4-10 (b) we plot the initiation stresses divided by the yielding stress of the base material against temperature as reported in Kaufman [92] (2008) and Table 4-I. The data points show that for intermediate temperatures (i.e. $T \leq 200\,^{\circ}\mathrm{C}$) the ratio remains approximately constant. This means that the limit stress follows the drop of the yielding stress which is also linear. However, for $T \geq 250\,^{\circ}\mathrm{C}$ the ratio starts increasing and the limit stress is not proportional to the base material yielding stress. Similar conclusions can be drawn about the drop

of the plateau stress as is seen in Fig. 4-12 (a) and (b). The relation between this stress and temperature is again almost linear with the equations of the fits being $\sigma_P = 2.528 - 0.0064T$ (with R = 0.991) for the 40 ppi foam and $\sigma_P = 2.169 - 0.0059T$ (with R = 0.997) for the 10 ppi foam.

The deviation of the initiation and plateau stresses from being proportional to the constituent alloy's yielding stress at high temperatures is very important for design purposes. It confirms that although yielding is the governing mechanism for the initiation of collapse in metal foams, its connection with local instabilities cannot be ignored. In this case, performing plastic collapse analysis on a single ligament is not able to capture accurately the macroscopic limit stress of the foam. We need to emphasize here that the data reported in Table 4-I refer to the base material but not the foamed material, which is not expected to have the exact same properties post-manufacturing. A more systematic connection between the foam response and the plastic behavior of the base metal would require a thermomechanical characterization on foam ligaments which is beyond the scope of this study that focuses on the macroscopic effects.

Fig. 4-13 shows the effect of temperature on the densification strain ε_D. As was clearly illustrated in the responses of Fig. 4-10 (a) and (b) the crushing of foam specimens under elevated temperatures leads to an extension of the plateau and an associated increase of the densification strain. This increase also follows the linear trend of the stresses with the fits being $\varepsilon_D = 0.477 + 0.0005T$ (R = 0.969) for the 40 ppi foam and $\varepsilon_D = 0.506 + 0.0005T$ (R = 0.933) for the 10 ppi foam. The effect of temperature on the densification regime is attributed to both the more distributed collapse at different zones within the foam specimen as well as the softening of the base material that allows for more compaction at the cell-level as was demonstrated by Figs. 4-7 and 4-8.

As mentioned in Chapter 1, open-cell metal foams are excellent energy absorbers

because of their ability to sustain low, and nearly constant, loads under large deformations. The energy absorption capacity of the foam is defined by their macroscopic strain energy density, i.e. the integrated macroscopic stress–strain response

$$U_0 = \int_0^{\varepsilon_D} \sigma d\varepsilon \tag{4.1}$$

Note here however, that this is only the case for quasi-static compression. At super-critical impact velocities, where shocks form, the energy absorption capacity increases and one needs to use the jump conditions to calculate it (see Barnes [93] et al., 2014; Gaitanaros and Kyriakides [71], 2014). Here we examine how crushing under high temperatures affects the energy absorption capacity. Fig. 4-14 shows the strain energy density as a function of temperature. It can be seen that it also follows a linear decrease, which is expected considering that the drop of the plateau stress is considerably larger than the corresponding increase of the densification strain. The loss of energy absorption capacity is rather significant with the energy absorbed at 300 °C being between 35% and 45% of the corresponding one at room temperature. The related linear fits are $U_0 = 1.245 - 0.0028T$ (with R = 0.986) for the 40 ppi foam and $U_0 = 1.259 - 0.0023T$ (with R = 0.972) for the 10 ppi foam.

Note here that experiments were also performed using smaller cubic specimens with 30mm sides. The size of those specimens was dictated by the largest specimen we could additionally characterize through microcomputed tomography. We found a slight specimen size effect (see Fig. 4-15) and we therefore chose not to include those results in the analysis of Figs. 4-10–4-14 and the associated fits, however we report all of our results in Table 4-II along with each foam specimen characteristics.

Table 4-I. Yield-stress of the base Al 6101-T6 under elevated temperatures (from Kaufman [92], 2008).

T (°C)	25	100	150	177	205	230	260	315
σ_y psi (MPa)	28000 (193)	25000 (172)	23000 (159)	22000 (152)	20000 (138)	16000 (110)	12000 (83)	6000 (41)

Table 4-II. Measured mechanical properties of Al 6101-T6 foam under high temperatures.

T (°C)	Cell-size ppi	Specimen edge length mm	$\frac{\rho^*}{\rho}$ (%)	E psi (MPa)	σ_I psi (MPa)	σ_P psi (MPa)	ε_D	U_0 psi (MPa)
20	40	30	7.03	24654 (169.98)	254.69 (1.76)	255.62 (1.76)	0.50	126.29 (0.87)
20	40	50	8.19	38100 (262.69)	313.32 (2.16)	341.81 (2.36)	0.50	167.76 (1.16)
20	10	50	8.23	46514 (320.70)	370.06 (2.55)	367.35 (2.53)	0.50	181.13 (1.25)
20	10	50	8.37	46934 (323.60)	367.69 (2.54)	352.06 (2.43)	0.53	173.19 (1.19)
150	40	50	7.42	33660 (232.08)	243.04 (1.68)	231.71 (1.60)	0.53	122.36 (0.84)
150	10	50	7.47	19880 (137.07)	296.23 (2.04)	271.64 (1.87)	0.56	149.68 (1.03)
200	40	50	7.52	34474 (237.69)	211.75 (1.46)	186.48 (1.29)	0.58	107.38 (0.74)
200	10	50	7.53	20007 (137.94)	240.78 (1.66)	213.60 (1.47)	0.59	124.38 (0.86)
250	40	50	7.79	26231 (180.86)	173.17 (1.19)	138.29 (0.95)	0.62	85.13 (0.59)
250	10	50	7.79	36873 (254.23)	211.70 (1.46)	159.21 (1.10)	0.66	104.85 (0.72)
300	40	30	7.35	16448 (113.41)	95.00 (0.66)	68.31 (0.47)	0.69	48.17 (0.33)
300	40	30	8.11	28261 (194.85)	140.29 (0.97)			
300	40	50	8.12	19880 (137.07)	115.52 (0.80)	75.29 (0.52)	0.65	49.42 (0.34)
300	10	50	8.17	18013 (124.20)	170.46 (1.18)	118.41 (0.81)	0.66	78.48 (0.54)

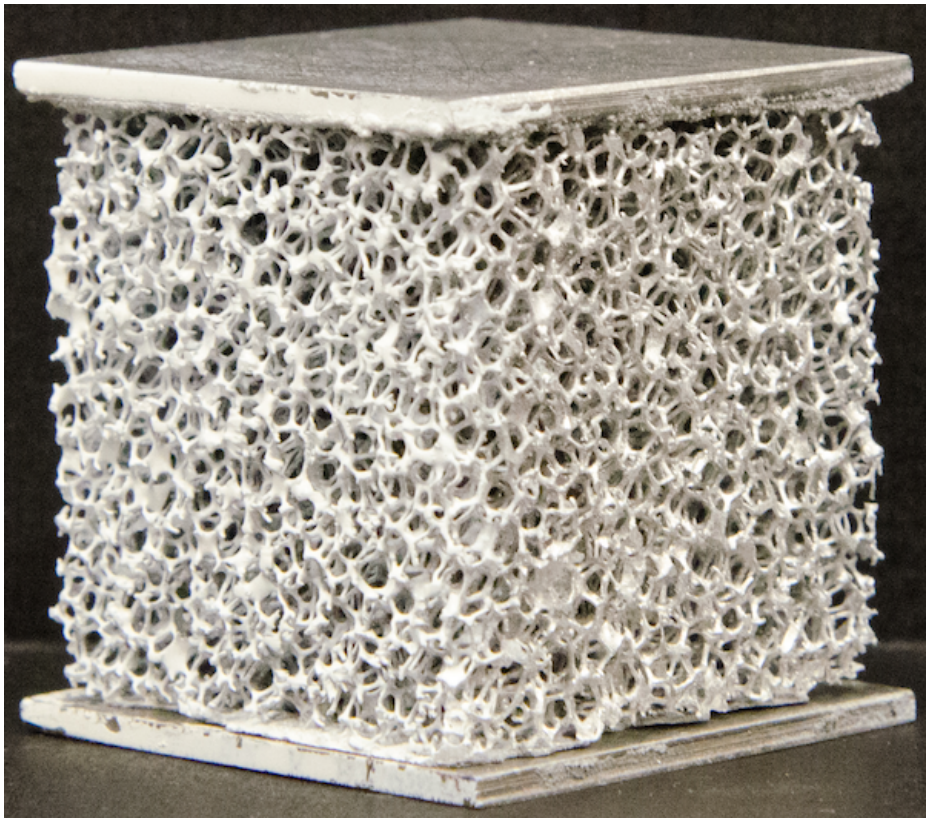

Figure 4-1. Foam specimen: open-cell aluminum foam with steel endplates attached using high-temperature resistant metal paste.

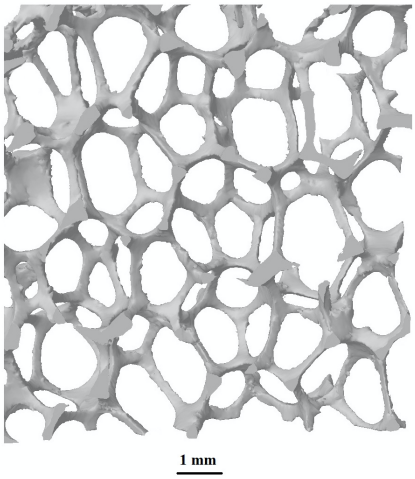

(a)

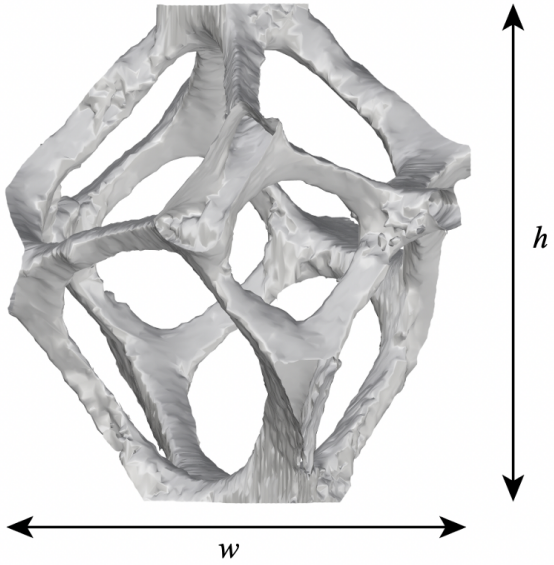

(b)

Figure 4-2. (a) Microcomputed tomography image of 40 ppi aluminum foam. (b) Single cell showing anisotropy induced by the foaming process.

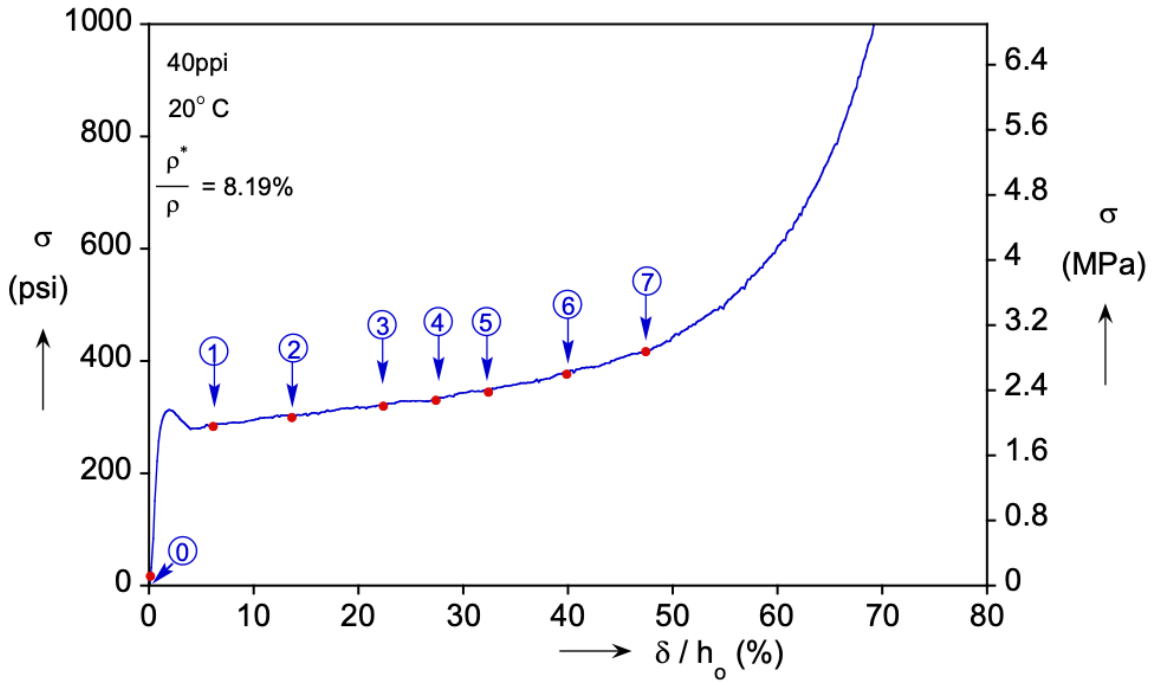

Figure 4-3. Typical compressive response of an Al alloy open-cell foam at room temperature.

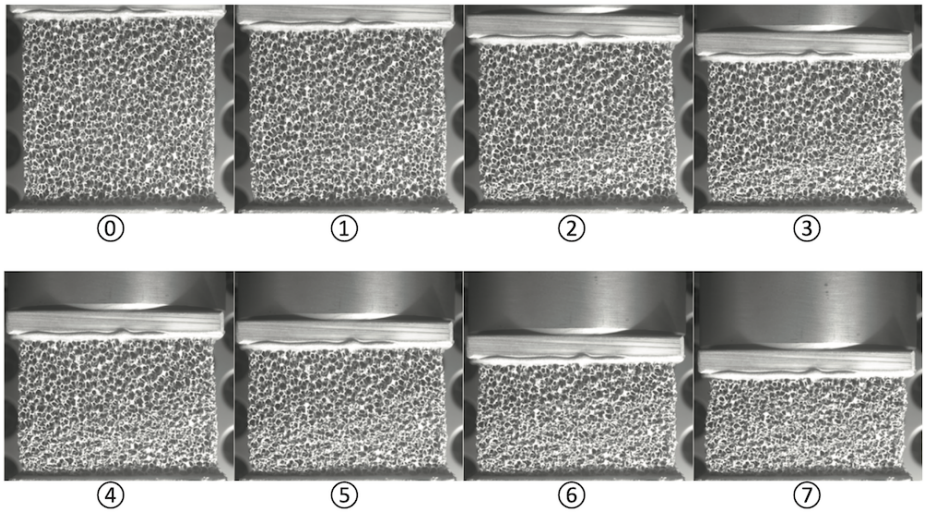

(a)

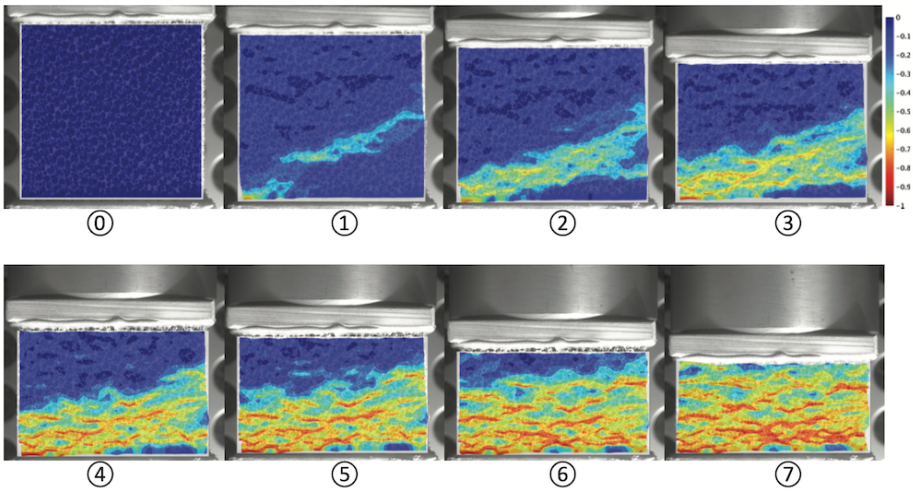

(b)

Figure 4-4. Evolution of crushing at room temperature: (a) sequence of images corresponding to points in Fig. 4-3 (b) DIC strain contours superposed on the images that illustrate band formation and propagation

Figure 4-5. An MTS environmental chamber and DIC system.

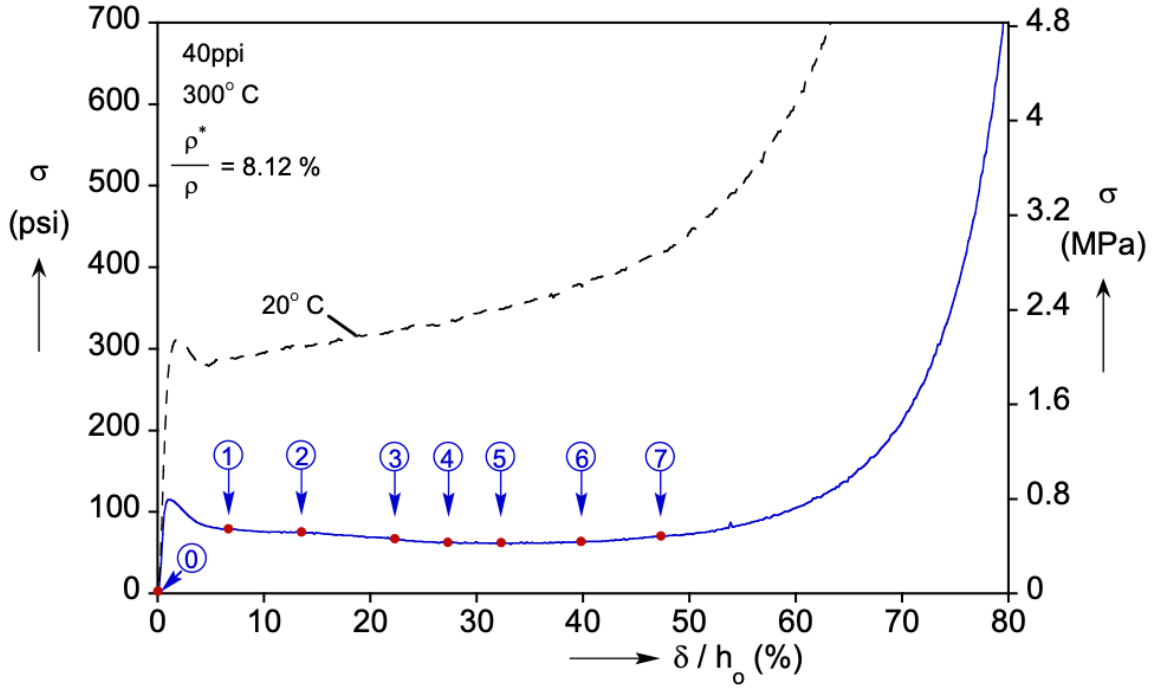

Figure 4-6. Typical compressive response of an Al alloy open-cell foam at high temperatures (T=300 °C).

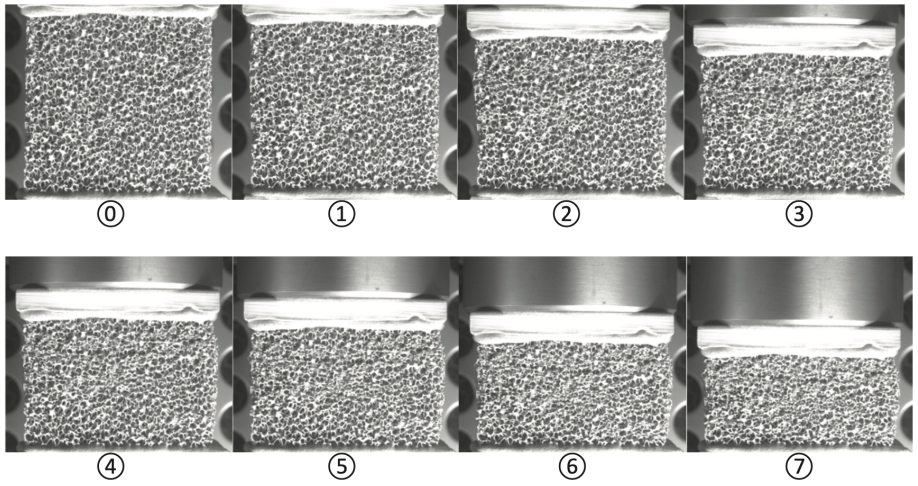

(a)

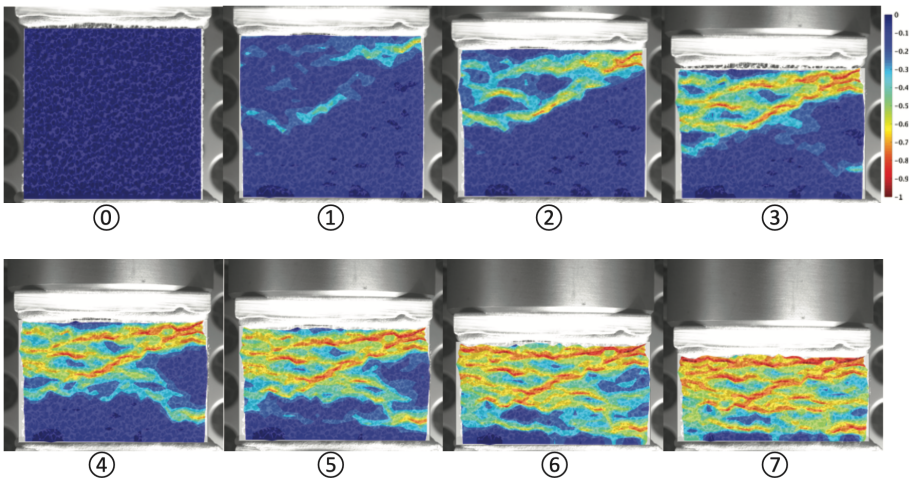

(b)

Figure 4-7. Evolution of crushing at high temperatures (T=300 °C): (a) sequence of images corresponding to points in Fig. 4-6 (b) DIC strain contours superposed on the images that illustrate the distributed collapse of cells in different areas within the foam.

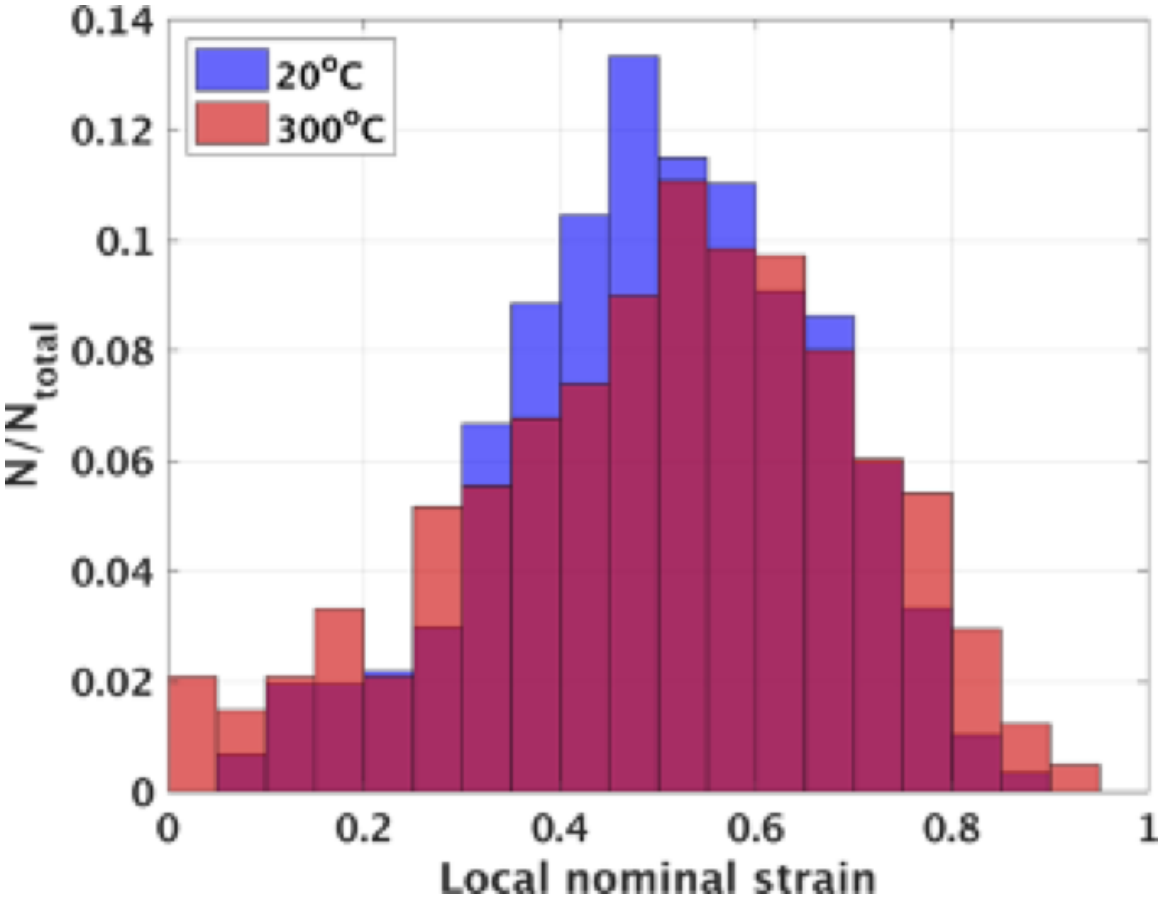

Figure 4-8. Histograms of local strains for crushing at T=20 °C and T=300 °C at the same level of average macroscopic strain 47%.

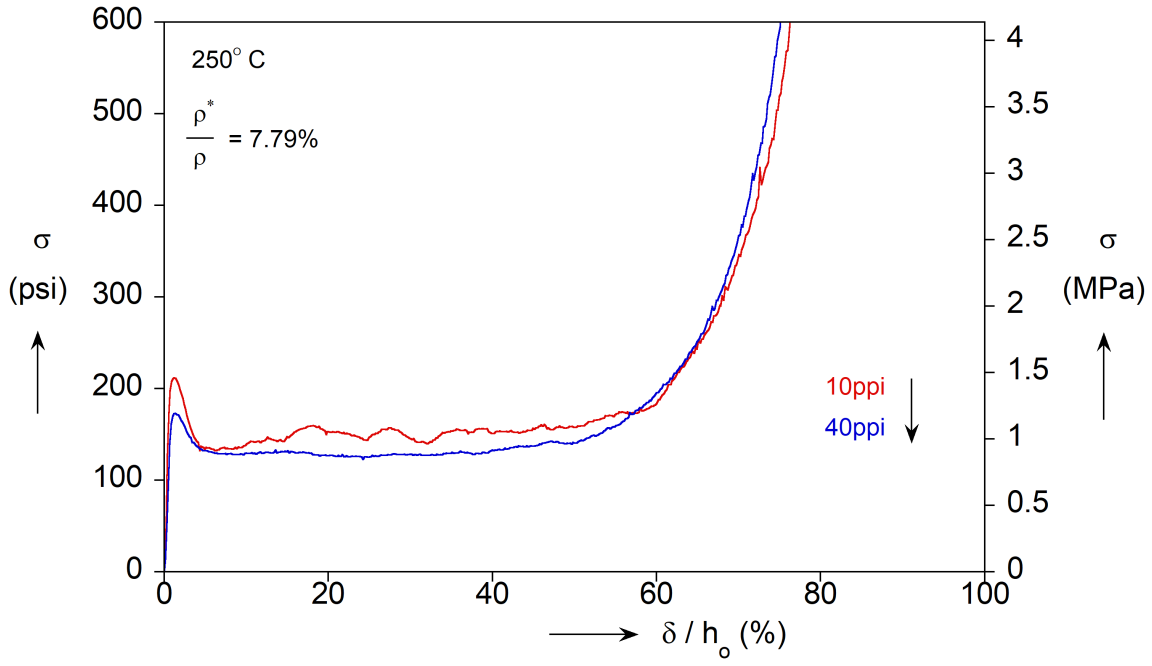

Figure 4-9. Effect of cell-size on the compressive response at high temperatures (T=250 °C) for foam specimens with equal relative density (7.79%).

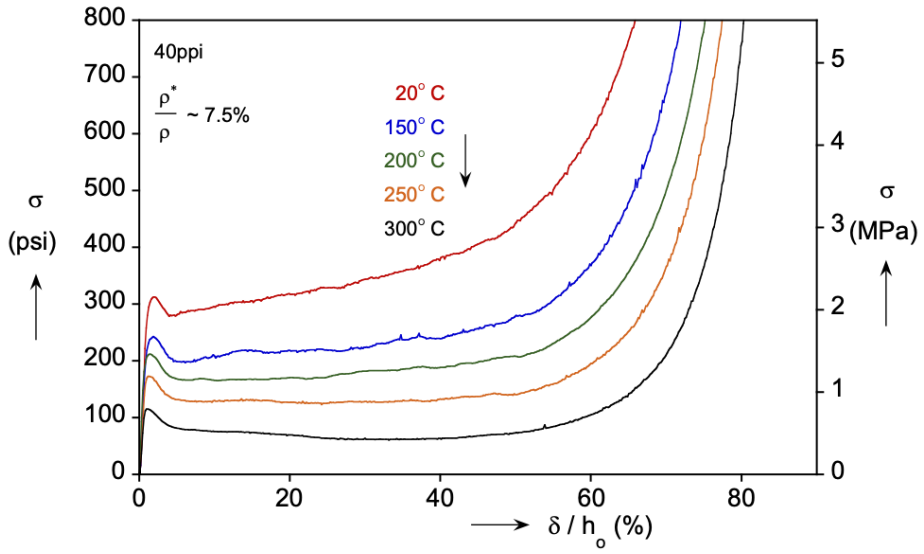

(a)

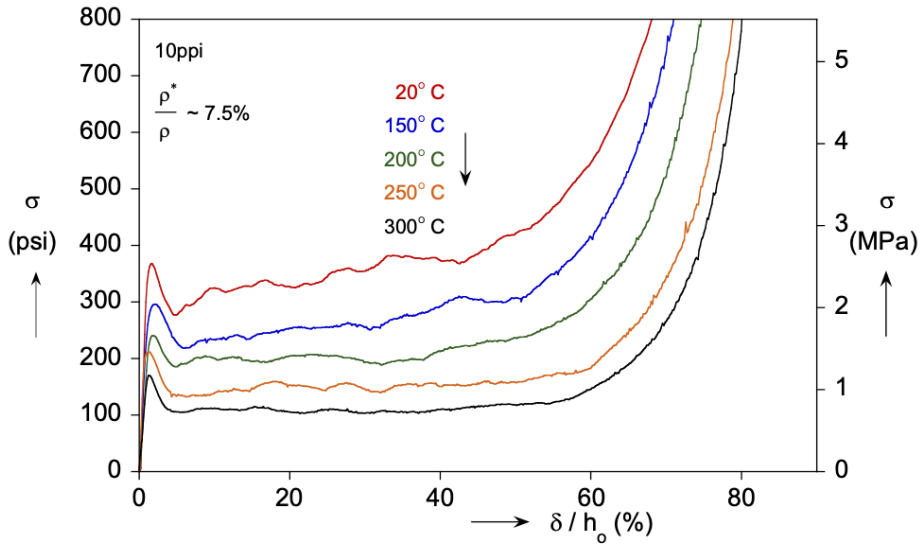

(b)

Figure 4-10. Compressive responses at a range of temperatures $20 \leq T \leq 300\,^{\circ}\mathrm{C}$ for the (a) 40 ppi foam and (b) 10 ppi foam (average relative density 7.5%).

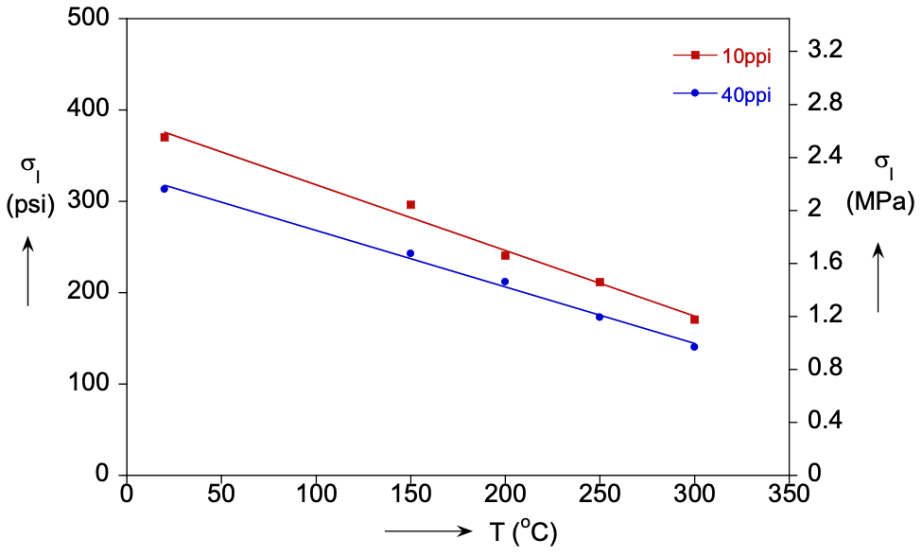

(a)

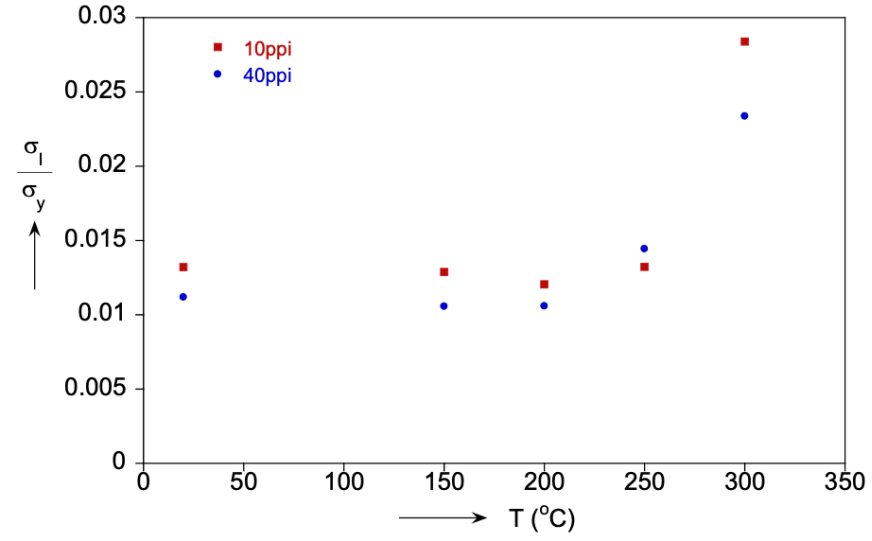

(b)

Figure 4-11. (a) Initiation stress vs. temperature for 40 ppi and 10 ppi foams, (b) Ratio of initiation stress to the yield limit of Al 6101-T6 as a function of temperature.

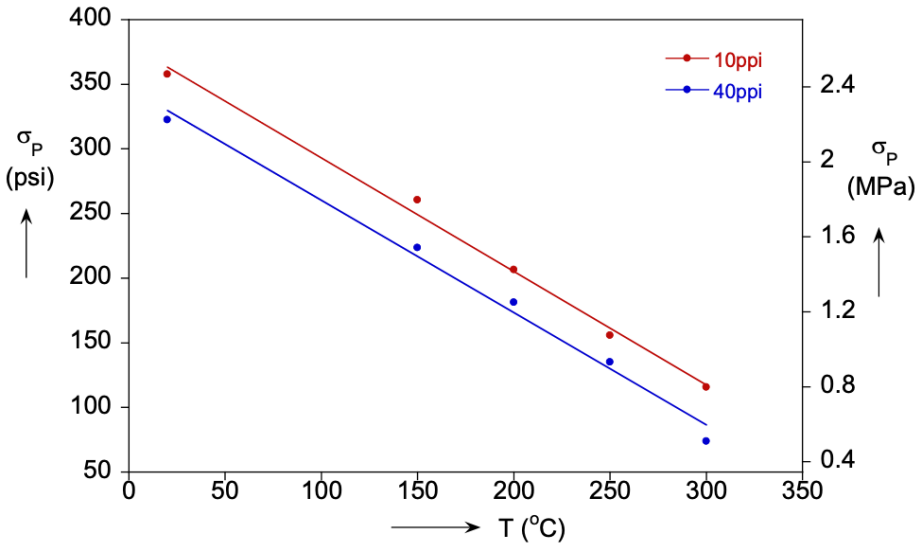

(a)

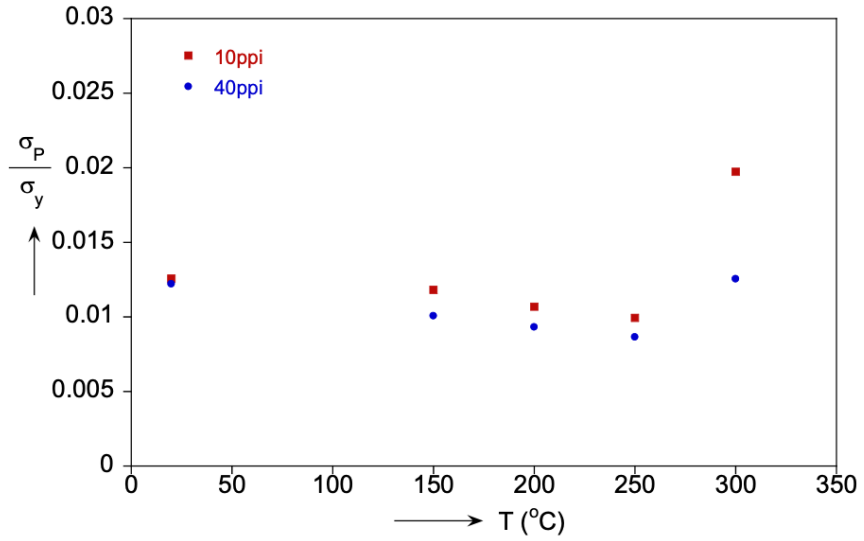

(b)

Figure 4-12. (a) Plateau stress vs. temperature for 40 ppi and 10 ppi foams, (b) Ratio of plateau stress to the yield limit of Al 6101-T6 as a function of temperature.

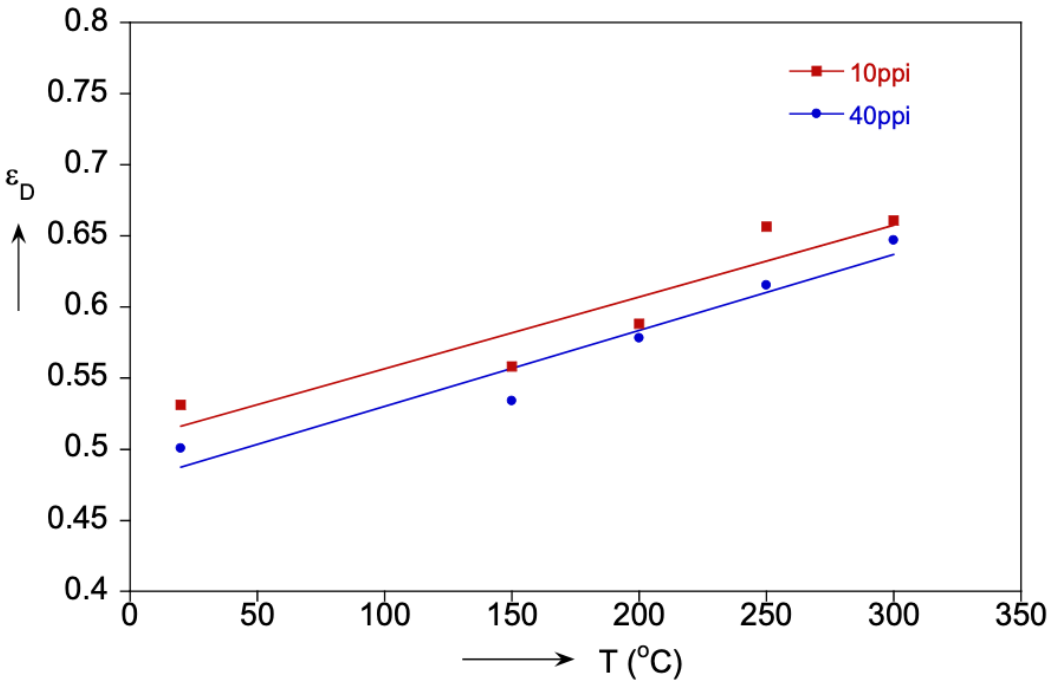

Figure 4-13. Densification strain vs. temperature.

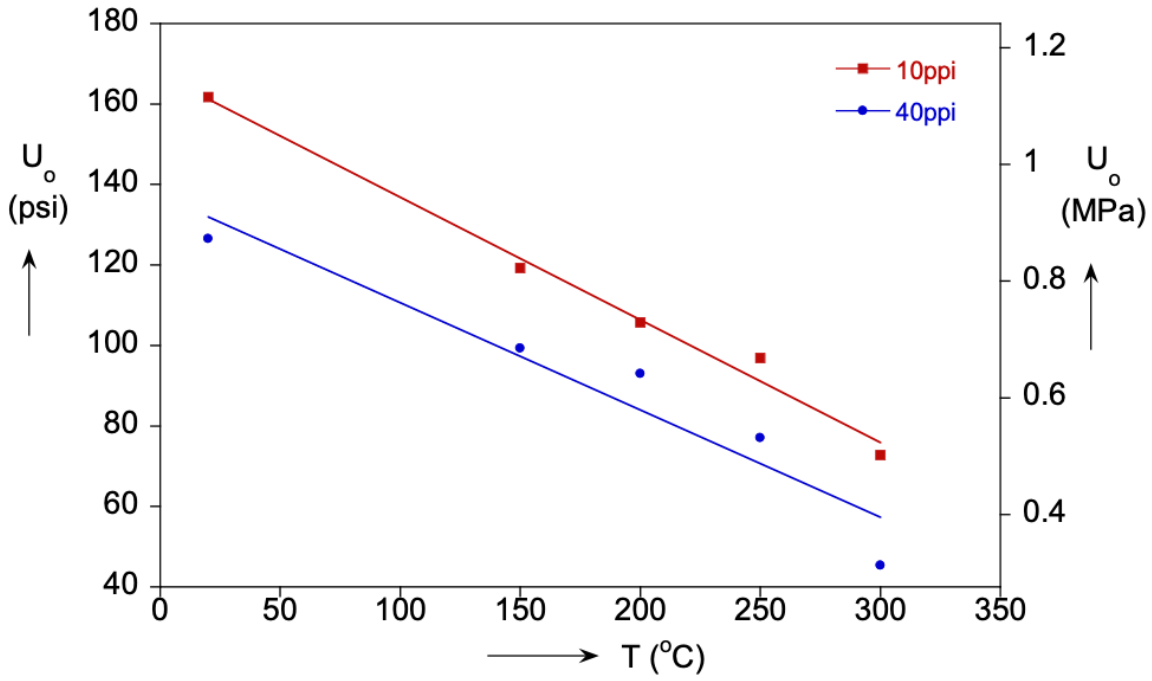

Figure 4-14. Strain energy absorption capacity vs. temperature.

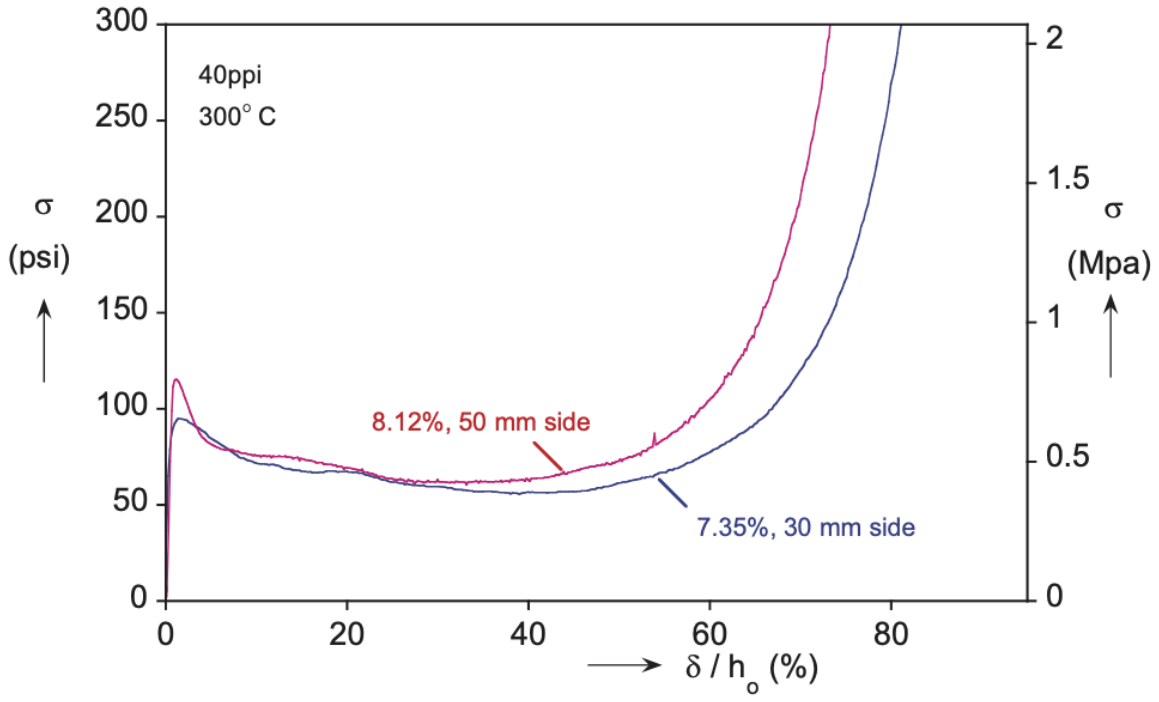

Figure 4-15. Effect of specimen size on the compressive response at high temperatures for foam specimens with the similar relative density.

Chapter 5

Conclusions and Future Work

This thesis explored the relationship between microstructure and strength of solid foams. In particular, microcomputed tomography and crushing experiments on (a) carbon, (b) additively-manufactured polymeric and (c) aluminum foams, were combined in order to understand how material synthesis, microstructure and loading conditions affect their mechanical properties.

5.1 Summary of Results on the Strength of Brittle Foams

We performed a series of tests on commercial carbon foams, including in-situ experiments within a tomography scanner. Foams of different cell-sized were crushed and the response was characteristic of cellular materials: it starts with a short linear elastic regime that ends on a limit-stress, followed by a constant load-plateau that extends to large macroscopic strains and densification. The results showed an inversely proportional increase of foam strength with cell-size, a phenomenon that is specific to brittle foams and has not been observed in the compression of soft polymeric or metal foams. The crushing response was also found to be highly sensitive on the load distribution at the boundary. Specimens with free-ends failed by sequential crushing of cells at the moving boundary while damage was initiated within the domain in specimens

with rigid plates attached to their ends. The change of deformation mechanism is associated with a significant increase in foam strength, that was however challenging to measure because of the large scatter, that is attributed on the foam-epoxy-plate interfaces and the strength of the parent carbon.

These results prompted the need for increased control over foam-microstructure and the base material properties, which was pursued here through additive manufacturing. Tessellation-based topologies were used to generate realistic microstructures of open-cell foams that were subsequently 3D-printed with an SLA printer. The fracture strength and brittle behavior of the base photopolymer was measured using tensile tests on small dog-bone specimens having the dimensions of foam ligaments. The material response was brittle with a fracture strength of about 60 MPa and a mean failure strain close to 3%. Synthesized foams were scanned by microcomputed tomography and manufacturing-induced variations were quantified through image analysis. Metrics such as the Hausdorff Distance were used to compare the geometry of 3D-printed foams to the corresponding design and the results showed a great accuracy of the synthesis protocol. Ligament orientations were found to be almost identical to the idealized tetrahedral angle. Characterization also showed that there is a small amount of volume shrinkage of the material caused by the additive manufacturing process, which of course alters the target relative density and has to be taken into account in the analysis of the foam properties. A series of experiments was performed to measure the compressive response and strength of the 3D-printed foams and connect it to load-transferring conditions, the strength of the base solid material and the foam relative density. Foam specimens bounded by supporting plates suffered a brittle failure when the response reached a critical stress level. Damage initiates at some area within the specimen and instantaneously traverses the foam. The stress level drops to zero and all strain energy is released. On the other hand, foams with a free end crush in a row-by-row type failure. Ligaments at the free end start breaking and the stress traces

a rugged plateau during which foam-cells in contact with the loading platen break. The plateau terminates at the densification regime where the response rises again. The foam strength, in this case, is much smaller than the corresponding one of the specimens with the plates. As the relative density increases, the difference between them decreases from 200% at $\overline{\rho} \approx 5\%$ to 50% at $\overline{\rho} \approx 15\%$. This is attributed to the increased strength of the ligaments at the boundary. Plotting the true foam strength against relative density for all experiments gives a power-law fit with C = 0.5706 and n = 1.6838. The coefficient is almost 3 times larger than the Gibson-Ashby formula (Gibson and Ashby [4], 1999) but is close to the original fit suggested by Ashby in (Ashby [24], 1983). The influence of elastic instabilities on the power exponent as the relative density approaches zero is an open subject that is left for future work.

5.2 Summary of Results for the Crushing of Metal Foams Under High-Temperatures

We further explored how high-temperatures affect the mechanical properties of metal foams, and in particular their plateau stress and associated energy absorption capacity. Cubical foam specimens with different cell-sizes (10 ppi and 40 ppi), were tested in uniaxial compression within an environmental chamber. The specimen was allowed to equilibrate for 20 min at the target temperature before the application of the compressive load. High resolution imaging and DIC were used to monitor and analyze the deformation characteristics and collapse mechanisms associated with crushing under high temperatures. To prevent peeling and facilitate the DIC analysis, the front side of the specimens was sprayed with paint resistant to very high surface temperatures.

The responses under high-temperatures seem qualitatively similar to corresponding results at room temperature exhibiting the initial elastic branch that terminates in a local stress maximum. This limit stress is then followed by a stress plateau that

extends to large deformations and ends with the second branch of rapidly increasing stiffness. However, the values of the limit and plateau stress as well the extension of the plateau and the associated densification strain, were seen to change significantly with temperature. When the foam is crushed at 300 °C the initiation stress is almost one-third of the corresponding one at room temperature while the decrease of the plateau stress is even larger. It is interesting to note that the decrease seen in both stresses is not proportional to the corresponding one of the base aluminum alloy's yielding stress.The densification strain on the other hand was seen to increase with temperature, and rise from around 50% to values reaching 65% before the response starts stiffening. These observations were supplemented with DIC analysis of the associated deformation mechanisms. Imaging revealed that localization and cell collapse under high temperatures happens in several different zones within the foam specimen. With increasing compaction the zones of crushed cells expand, some of them merge, and cell- collapse in different areas initiates as well. This is a significant deviation from the localization and collapse mechanism at room temperature; that is from a single complete band of crushed cells that traverses the foam to a more widespread type collapse. Crushing under high temperatures also leads to additional compaction at the cell level caused by the softening of the material. This is attributed to both the decrease of the base alloy's Young's modulus with the temperature that softens the contact between ligaments, as well as the reduction of its post-yielding hardening that creates increased local bending of the foam ligaments. The collective effect of these deformation mechanisms alters the characteristics of the stress plateau. First, the slope of the plateau decreases and at high-temperatures $T \geq 250\,^{\circ}\mathrm{C}$ softening produces a concave-up shape. Moreover, the distributed crushing and increased local compaction at the cell level extend the plateau to larger deformations and increased associated densification strains.

These observations were consistent in a series of crushing tests in a temperature

range $20\,^{\circ}\mathrm{C} \leq T \leq 300\,^{\circ}\mathrm{C}$. From these tests, the effect of temperature on all mechanical properties was quantified. The results indicate a linear trend for all important variables: the limit and plateau stresses that increase and the densification strain that decreases. The combined effect of the stress plateau and the densification strain produces a drop in the strain energy absorbed during crushing. It is interesting to note that the linear dependence of the foam mechanical properties with temperature resembles the corresponding linear trend that has been observed with respect to the foam relative density. The difference is that the effect is opposite, i.e. an increase in density leads to increase in the stresses and decrease of the densification strain, and also that the response is more sensitive to density variations.

5.3 Future Research Directions

This thesis focused on the strength of brittle foams and its connection to the underlying microstructure. Additive manufacturing is shown to be an important tool in the study of cellular solids with controlled morphological characteristics. It would be interesting to combine stereolithography and pyrolysis as a means to synthesize carbon cellular materials, both random and regular, that can attain or surpass the mechanical properties of carbon foams but with minimal scatter. Furthermore, one could also explore the resulting thermal insulation capacity of additively-manufactured carbon cellular solids and especially the design of microstructures that provide superior combinations of strength and thermal conductivity. Physics-based modeling would be an important component of such studies due to the large number of processing and morphological parameters involved. Finally, one could examine the behavior of the resulting designed materials under both extreme temperatures and high velocity impacts.

References

1. Gibson, L. J., Ashby, M. F. & Harley, B. A. *Cellular materials in nature and medicine* (Cambridge University Press, 2010).
2. Cunningham, A. & Hilyard, N. in *Low density cellular plastics* 1–21 (Springer, 1994).
3. Ashby, M. F. *et al. Metal foams: a design guide* (Elsevier, 2000).
4. Gibson, L. J. & Ashby, M. F. *Cellular solids: structure and properties* (Cambridge university press, 1999).
5. Klintworth, J. & Stronge, W. Elasto-plastic yield limits and deformation laws for transversely crushed honeycombs. *International Journal of Mechanical Sciences* **30,** 273–292 (1988).
6. Papka, S. D. & Kyriakides, S. In-plane compressive response and crushing of honeycomb. *Journal of the Mechanics and Physics of Solids* **42,** 1499–1532 (1994).
7. Papka, S. D. & Kyriakides, S. Experiments and full-scale numerical simulations of in-plane crushing of a honeycomb. *Acta materialia* **46,** 2765–2776 (1998).
8. Papka, S. D. & Kyriakides, S. In-plane crushing of a polycarbonate honeycomb. *International Journal of Solids and Structures* **35,** 239–267 (1998).
9. Triantafyllidis, N. & Schraad, M. Onset of failure in aluminum honeycombs under general in-plane loading. *Journal of the Mechanics and Physics of Solids* **46,** 1089–1124 (1998).
10. Zhou, J., Mercer, C. & Soboyejo, W. An investigation of the microstructure and strength of open-cell 6101 aluminum foams. *Metallurgical and Materials Transactions A* **33,** 1413–1427 (2002).
11. Zhou, J., Shrotriya, P. & Soboyejo, W. Mechanisms and mechanics of compressive deformation in open-cell Al foams. *Mechanics of Materials* **36,** 781–797 (2004).
12. Zhou, J., Allameh, S. & Soboyejo, W. Microscale testing of the strut in open cell aluminum foams. *Journal of materials science* **40,** 429–439 (2005).
13. Gong, L., Kyriakides, S. & Jang, W.-Y. Compressive response of open-cell foams. Part I: Morphology and elastic properties. *International Journal of Solids and Structures* **42,** 1355–1379 (2005).
14. Gong, L. & Kyriakides, S. Compressive response of open cell foams Part II: Initiation and evolution of crushing. *International Journal of Solids and Structures* **42,** 1381–1399 (2005).
15. Jang, W.-Y. & Kyriakides, S. On the crushing of aluminum open-cell foams: Part I. Experiments. *International Journal of Solids and Structures* **46,** 617–634 (2009).

16. Jang, W.-Y. & Kyriakides, S. On the crushing of aluminum open-cell foams: Part II analysis. *International Journal of Solids and Structures* **46,** 635–650 (2009).

17. Gaitanaros, S., Kyriakides, S. & Kraynik, A. M. On the crushing response of random open-cell foams. *International Journal of Solids and Structures* **49,** 2733–2743 (2012).

18. Sugimura, Y. *et al.* On the mechanical performance of closed cell Al alloy foams. *Acta materialia* **45,** 5245–5259 (1997).

19. Gioux, G., McCormack, T. & Gibson, L. Failure of aluminum foams under multiaxial loads. *International Journal of Mechanical Sciences* **42,** 1097–1117 (2000).

20. Congdon, E., Mehoke, D., Buchta, M., Nagle, D. & Zhang, D. *Development of High-Temperature Optical Coating for Thermal Management on Solar Probe Plus* in *10th AIAA/ASME Joint Thermophysics and Heat Transfer Conference* (2010), 4661.

21. Bauer, J., Schroer, A., Schwaiger, R. & Kraft, O. Approaching theoretical strength in glassy carbon nanolattices. *Nature materials* **15,** 438–443 (2016).

22. Hager, J. W. Widealized Strut Geometries for Open-Celled Foams. *MRS Online Proceedings Library Archive* **270** (1992).

23. Gibson, I. & Ashby, M. F. The mechanics of three-dimensional cellular materials. *Proceedings of the Royal Society of London. A. Mathematical and Physical Sciences* **382,** 43–59 (1982).

24. Ashby, M. F. & Medalist, R. M. The mechanical properties of cellular solids. *Metallurgical Transactions A* **14,** 1755–1769 (1983).

25. Maiti, S., Ashby, M. & Gibson, L. Fracture toughness of brittle cellular solids. *Scripta Metallurgica* **18,** 213–217 (1984).

26. Huang, J. & Gibson, L. Fracture toughness of brittle honeycombs. *Acta metallurgica et materialia* **39,** 1617–1626 (1991).

27. Brezny, R. & Green, D. J. Fracture Behavior of Open-Cell Ceramics. *Journal of the American Ceramic Society* **72,** 1145–1152 (1989).

28. Choi, S. & Sankar, B. Fracture toughness of carbon foam. *Journal of Composite Materials* **37,** 2101–2116 (2003).

29. Quintana-Alonso, I. & Fleck, N. A. in *Major accomplishments in composite materials and sandwich structures* 799–816 (Springer, 2009).

30. Alonso, I. Q. & Fleck, N. Damage tolerance of an elastic-brittle diamond-celled honeycomb. *Scripta Materialia* **56,** 693–696 (2007).

31. Fleck, N. A. & Qiu, X. The damage tolerance of elastic–brittle, two-dimensional isotropic lattices. *Journal of the Mechanics and Physics of Solids* **55,** 562–588 (2007).

32. Combaz, E. & Mortensen, A. Fracture toughness of Al replicated foam. *Acta materialia* **58,** 4590–4603 (2010).

33. O'Masta, M. R., Dong, L., St-Pierre, L., Wadley, H. & Deshpande, V. S. The fracture toughness of octet-truss lattices. *Journal of the Mechanics and Physics of Solids* **98,** 271–289 (2017).

34. Kucherov, L. & Ryvkin, M. Fracture toughness of open-cell Kelvin foam. *International Journal of Solids and Structures* **51,** 440–448 (2014).

35. Mora, R. J. & Waas, A. M. Strength scaling of brittle graphitic foam. *Proceedings of the Royal Society of London. Series A: Mathematical, Physical and Engineering Sciences* **458,** 1695–1718 (2002).

36. Letellier, M., Delgado-Sanchez, C., Khelifa, M., Fierro, V. & Celzard, A. Mechanical properties of model vitreous carbon foams. *Carbon* **116,** 562–571 (2017).

37. Voigt, C. *et al.* The influence of the measurement parameters on the crushing strength of reticulated ceramic foams. *Journal of Materials Research* **28,** 2288–2299 (2013).

38. Song, H.-W., He, Q.-J., Xie, J.-J. & Tobota, A. Fracture mechanisms and size effects of brittle metallic foams: In situ compression tests inside SEM. *Composites Science and Technology* **68,** 2441–2450 (2008).

39. Nakanishi, K. *et al.* Compressive behavior and failure mechanisms of freestanding and composite 3D graphitic foams. *Acta Materialia* **159,** 187–196 (2018).

40. Wang, J. Reticulated vitreous carbon—a new versatile electrode material. *Electrochimica Acta* **26,** 1721–1726 (1981).

41. Wickham, M. G., Cleveland, P. H., Binder, P. S. & Akers, P. H. Growth of cultured corneal endothelial cells onto a vitreous carbon matrix. *Ophthalmic research* **15,** 116–120 (1983).

42. Łukaszewski, M., Żurowski, A. & Czerwiński, A. Hydrogen in thin Pd-based layers deposited on reticulated vitreous carbon—A new system for electrochemical capacitors. *Journal of Power Sources* **185,** 1598–1604 (2008).

43. Czerwiński, A. *et al.* RVC as new carbon material for batteries. *Journal of applied electrochemistry* **39,** 559–567 (2009).

44. Mastragostino, M. & Valcher, S. Polymeric salt as bromine complexing agent in a Zn-Br2 model battery. *Electrochimica Acta* **28,** 501–505 (1983).

45. Moss, W. C. *et al.* Computed optical emissions from a sonoluminescing bubble. *Physical Review E* **59,** 2986 (1999).

46. Chakhovskoi, A. G., Hunt, C. E., Forsberg, G., Nilsson, T. & Persson, P. Reticulated vitreous carbon field emission cathodes for light source applications. *Journal of Vacuum Science & Technology B: Microelectronics and Nanometer Structures Processing, Measurement, and Phenomena* **21,** 571–575 (2003).

47. Czarnecki, J. S., Blackmore, M., Jolivet, S., Lafdi, K. & Tsonis, P. A. Bone growth on reticulated vitreous carbon foam scaffolds and implementation of cellular automata modeling as a predictive tool. *Carbon* **79,** 135–148 (2014).

48. Heui-Seol, H.-S. Characterization of the acoustic properties of random porous media: reticulated vitreous carbon and aluminum foam. *Journal of Korean Physical Society* **53,** 607 (2008).

49. Friedrich, J., Ponce-de-León, C., Reade, G. & Walsh, F. Reticulated vitreous carbon as an electrode material. *Journal of Electroanalytical Chemistry* **561,** 203–217 (2004).

50. Knippenberg, W. & Lersmacher, B. Carbon foam. *Philips Technical Review* **36,** 93–103 (1976).

51. Walsh, F. *et al.* The continued development of reticulated vitreous carbon as a versatile electrode material: Structure, properties and applications. *Electrochimica Acta* **215,** 566–591 (2016).

52. Scheffler, M. & Colombo, P. *Cellular ceramics: structure, manufacturing, properties and applications* (John Wiley & Sons, 2006).

53. Vinton, C. S. & Franklin, C. H. *Method for the preparation of vitreous carbon foams* US Patent 4,022,875. May 1977.

54. Stankiewicz, E. P. *Method for producing controlled aspect ratio reticulated carbon foam and the resultant foam* US Patent 6,103,149. Aug. 2000.

55. Jang, W.-Y., Kraynik, A. M. & Kyriakides, S. On the microstructure of open-cell foams and its effect on elastic properties. *International Journal of Solids and Structures* **45,** 1845–1875 (2008).

56. Hernández-Nava, E. *et al.* The effect of density and feature size on mechanical properties of isostructural metallic foams produced by additive manufacturing. *Acta Materialia* **85,** 387–395 (2015).

57. Yang, L. *et al.* Mechanical response of a triply periodic minimal surface cellular structures manufactured by selective laser melting. *International Journal of Mechanical Sciences* **148,** 149–157 (2018).

58. Seiler, P. E., Tankasala, H. & Fleck, N. The role of defects in dictating the strength of brittle honeycombs made by rapid prototyping. *Acta Materialia* **171,** 190–200 (2019).

59. Xu, Y., Zhang, H., Šavija, B., Figueiredo, S. C. & Schlangen, E. Deformation and fracture of 3D printed disordered lattice materials: Experiments and modeling. *Materials & Design* **162,** 143–153 (2019).

60. Latture, R. M., Rodriguez, R. X., Holmes Jr, L. R. & Zok, F. W. Effects of nodal fillets and external boundaries on compressive response of an octet truss. *Acta Materialia* **149,** 78–87 (2018).

61. Ling, C., Cernicchi, A., Gilchrist, M. D. & Cardiff, P. Mechanical behaviour of additively-manufactured polymeric octet-truss lattice structures under quasi-static and dynamic compressive loading. *Materials & Design* **162,** 106–118 (2019).

62. Tancogne-Dejean, T., Spierings, A. B. & Mohr, D. Additively-manufactured metallic micro-lattice materials for high specific energy absorption under static and dynamic loading. *Acta Materialia* **116,** 14–28 (2016).

63. Amani, Y., Dancette, S., Delroisse, P., Simar, A. & Maire, E. Compression behavior of lattice structures produced by selective laser melting: X-ray tomography based experimental and finite element approaches. *Acta Materialia* **159,** 395–407 (2018).

64. Wang, S., Zheng, Z., Zhu, C., Ding, Y. & Yu, J. Crushing and densification of rapid prototyping polylactide foam: Meso-structural effect and a statistical constitutive model. *Mechanics of Materials* **127,** 65–76 (2018).

65. Bi, S., Chen, E. & Gaitanaros, S. Additive manufacturing and characterization of brittle foams. *Mechanics of Materials* **145,** 103368 (2020).

66. Kraynik, A. M., Reinelt, D. A. & van Swol, F. Structure of random monodisperse foam. *Physical Review E* **67,** 031403 (2003).

67. Kraynik, A. M., Reinelt, D. A. & van Swol, F. Structure of random foam. *Physical Review Letters* **93,** 208301 (2004).

68. Brakke, K. A. The surface evolver. *Experimental mathematics* **1,** 141–165 (1992).

69. Plateau, J. *Statique expérimentale et théorique des liquides soumis aux seules forces moléculaires* (Gauthier-Villars, 1873).

70. Matzke, E. B. The three-dimensional shape of bubbles in foam-an analysis of the role of surface forces in three-dimensional cell shape determination. *American Journal of Botany,* 58–80 (1946).

71. Gaitanaros, S. & Kyriakides, S. Dynamic crushing of aluminum foams: Part II–Analysis. *International Journal of Solids and Structures* **51,** 1646–1661 (2014).

72. Bayat, A. & Gaitanaros, S. Elastic wave propagation in open-cell foams. *Journal of Applied Mechanics* **86** (2019).

73. Yang, C. & Kyriakides, S. Multiaxial crushing of open-cell foams. *International Journal of Solids and Structures* **159,** 239–256 (2019).

74. Gaitanaros, S. & Kyriakides, S. On the effect of relative density on the crushing and energy absorption of open-cell foams under impact. *International Journal of Impact Engineering* **82,** 3–13 (2015).

75. Gaitanaros, S., Kyriakides, S. & Kraynik, A. M. On the crushing of polydisperse foams. *European Journal of Mechanics-A/Solids* **67,** 243–253 (2018).

76. Jung, A. & Diebels, S. Micromechanical Characterization of Metal Foams. *Advanced Engineering Materials* **21,** 1900237 (2019).

77. Amani, Y., Dancette, S., Luksch, J., Jung, A. & Maire, E. Micro-tensile behavior of struts extracted from an aluminum foam. *Materials Characterization,* 110456 (2020).

78. Huang, Y.-M. & Lan, H.-Y. Compensation of distortion in the bottom exposure of stereolithography process. *The International Journal of Advanced Manufacturing Technology* **27,** 1101–1112 (2006).

79. Bruker. SkyScan material testing stage for the 1174, 1172 and 1173 micro-CT systems, user manual (2010).

80. Cady, C. M., Gray Iii, G., Liu, C., Lovato, M. L. & Mukai, T. Compressive properties of a closed-cell aluminum foam as a function of strain rate and temperature. *Materials Science and Engineering: A* **525,** 1–6 (2009).

81. Wang, P. *et al.* Temperature effects on the mechanical behavior of aluminum foam under dynamic loading. *Materials Science and Engineering: A* **599,** 174–179 (2014).

82. Movahedi, N., Linul, E. & Marsavina, L. The temperature effect on the compressive behavior of closed-cell aluminum-alloy foams. *Journal of Materials Engineering and Performance* **27,** 99–108 (2018).

83. Linul, E., Movahedi, N. & Marsavina, L. The temperature and anisotropy effect on compressive behavior of cylindrical closed-cell aluminum-alloy foams. *Journal of Alloys and Compounds* **740,** 1172–1179 (2018).

84. Mondal, D., Jha, N., Badkul, A., Das, S. & Khedle, R. High temperature compressive deformation behaviour of aluminum syntactic foam. *Materials Science and Engineering: A* **534,** 521–529 (2012).

85. Taherishargh, M., Linul, E., Broxtermann, S. & Fiedler, T. The mechanical properties of expanded perlite-aluminium syntactic foam at elevated temperatures. *Journal of Alloys and Compounds* **737,** 590–596 (2018).

86. Linul, E., Lell, D., Movahedi, N., Codrean, C. & Fiedler, T. Compressive properties of zinc syntactic foams at elevated temperatures. *Composites Part B: Engineering* **167,** 122–134 (2019).

87. Aakash, B., Bi, S., Shields, M. D. & Gaitanaros, S. On the high-temperature crushing of metal foams. *International Journal of Solids and Structures* **174,** 18–27 (2019).

88. Jang, W.-Y. & Kyriakides, S. On the crushing of aluminum open-cell foams: Part I. Experiments. *International Journal of Solids and Structures* **46,** 617–634 (2009).

89. Bastawros, A., Bart-Smith, H. & Evans, A. Experimental analysis of deformation mechanisms in a closed-cell aluminum alloy foam. *Journal of the Mechanics and Physics of Solids* **48,** 301–322 (2000).

90. Lee, S., Barthelat, F., Moldovan, N., Espinosa, H. D. & Wadley, H. N. Deformation rate effects on failure modes of open-cell Al foams and textile cellular materials. *International Journal of Solids and Structures* **43,** 53–73 (2006).

91. Sutton, M. A., Orteu, J. J. & Schreier, H. *Image correlation for shape, motion and deformation measurements: basic concepts, theory and applications* (Springer Science & Business Media, 2009).

92. Kaufman, J. G. *Properties of aluminum alloys: fatigue data and the effects of temperature, product form, and processing* (ASM International, 2008).

93. Barnes, A., Ravi-Chandar, K., Kyriakides, S. & Gaitanaros, S. Dynamic crushing of aluminum foams: Part I–Experiments. *International Journal of Solids and Structures* **51,** 1631–1645 (2014).

Biographical sketch

Sirui Bi was born in Jinan, Shandong, China. She received the degree of Bachelor of Science in Mathematics and Applied Mathematics in July 2011. In August 2012, she entered Dalian University of Technology and received a Master of Science in Engineering Mechanics in July 2015. In August 2015, she enrolled in the Civil and Systems Engineering department at the Johns Hopkins University pursuing a Ph.D. degree in the area of Mechanics of Materials.